COLLAGEN FIBRILS FROM PHYSIOLOGICALLY DISTINCT TENDONS FOLLOW UNIQUE PATHS TO FAILURE

by

Andrew S Quigley

Submitted in partial fulfillment of the requirements
for the degree of Master of Science

at

Dalhousie University
Halifax, Nova Scotia
November 2016

This thesis is dedicated to my mother and father for teaching me the value of balance, and to my sister for leading by example.

Table of Contents

List of Tables

List of Figures

Abstract

The collagen fibril is a fundamental unit in the mammalian class, providing strength and structure to various tissues. Here, I investigated the mechanical, morphological, and molecular properties of isolated collagen fibrils from two bovine forelimb tendons, which compose an energy storing - positional tendon pair. For each isolated fibril, two strips of glue were used to isolate a segment, which was pulled to rupture with an atomic force microscope. The stress-strain behavior of single fibrils was highly dependent on tendon type. Post-rupture AFM imaging showed that flexor fibrils were robust against plastic damage, while extensor fibrils were susceptible to plastic deformation. Second harmonic generation microscopy was used to investigate molecular organization pre- and post-rupture, and the molecular state was not altered by rupture in flexor fibrils, but was disrupted in extensor fibrils. The work shows that fibrils from distinct tendons follow unique mechanistic paths to failure.

List of Abbreviations Used

AFM	atomic force microscopy
AGE	advanced glycation end-product
BTT	bovine tail tendon
CDET	common digital extensor tendon
CHP	collagen hybridizing peptide
EDTA	ethylenediaminetetraacetic acid
GAG	glycosaminoglycan
HP	hydroxylysyl pyridinoline
HPT	human patellar tendon
MD	molecular dynamics
MEMS	microelectromechanical
pen-strep	penicillin-streptomycin
PG	proteoglycan
PMSF	phenylmethylsulfonyl fluoride
RPT	rat patellar tendon
RTT	rat tail tendon
SDFT	superficial digital flexor tendon
SEM	scanning electron microscopy
SHG	second harmonic generation

XRD   x-ray diffraction

Acknowledgements

Chapter 1

Introduction

1.1 Tendon

Tendons are soft collagenous tissues which are found across the mammalian class. Serving a primarily mechanical function, the role of tendon is to bear the force generated by muscle contraction and transmit it to a bone. The mechanical requirements of tendon are achieved through a hierarchy of collagenous structures, which is generally conserved across different tendons.

1.1.1 Energy-storing and positional tendon classification

Two functionally distinct classes of tendon have been shown to exist: energy-storing and positional. This dichotomy exists because particular tendons used in mammalian locomotion are thought to provide work via release of stored strain energy [1, 2]. Energy-storing tendons in the forelimbs of large quadripeds such as the horse and cow are estimated to receive much higher stresses than anatomically proximate positional tendons (69-75 MPa vs. 8-36 MPa) [3]. The human Achilles tendon is the primary energy-storing tendon in humans, and is estimated to receive a similar maximum stress of 67 MPa [3]. While the physiological roles of anatomically separate tendons are distinct, many features including general composition and hierarchical organization, are conserved.

1.1.2 Tendon composition and structural hierarchy

Tendons are largely made up of water and collagen: water contributes 50-65% of the tendon wet mass [4, 5, 6], and collagen contributes 70-85% of tendon dry mass [7, 4, 5, 6]. The collagen in tendon is principally type I, with small amounts of collagen III and V [8]. In addition to water and collagen, other components are present in much smaller quantities. Proteoglycans (PGs), which are brush-like units composed of long negatively charged glycosaminoglycans (GAGs) attached to a core protein, are present at the surface of fibrils, bind large amounts of water [9], and are thought

to organize the tissue [10]. Small, leucine rich PGs including decorin, biglycan, and fibromodulin are the most common PGs found in tendon [11, 9], contributing 0.5-3% of tendon dry mass [12, 13]. Elastin is also present in small amounts (<2%) [14]. There is a relatively small population of tenocytes, which maintain the tissue [15].

Tendons are hierarchically ordered over seven orders of magnitude: tendons ($\sim$ 1-10 mm in diameter) are composed of multiple fascicles ($\sim$ 100 μm) which are composed of fibers ($\sim$ 1 μm), fibrils ($\sim$ 100 nm), and single collagen molecules ($\sim$ 1 nm) [16, 17] (Figure 1.1, adapted from [18]).
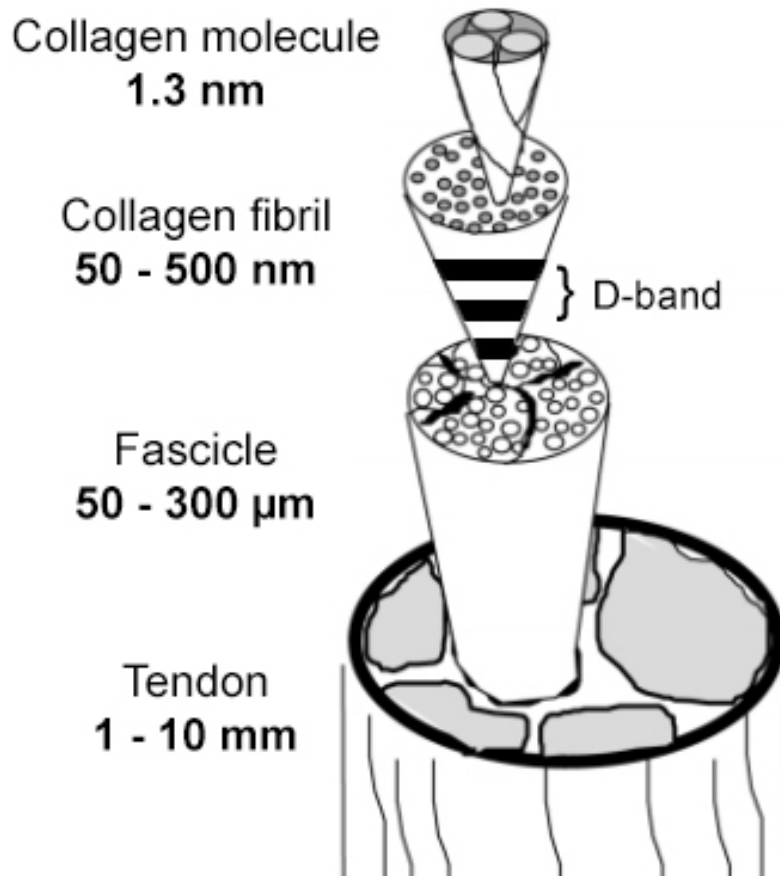
Figure 1.1: Structural hierarchy in tendon. Figure adapted from [18].

1.1.3 Collagen synthesis and fibrillogenesis

One of the defining features of collagen protein is the triple helical molecule [19, 20, 21]. Three individual left-handed α-chains, each composed of a Gly-X-Y repeating tripeptide sequence in a polyproline II conformation [22, 23], are coiled around each

other and form a right-handed triple helix. Having a glycine for every third amino acid is essential for proper triple helical conformation, because only glycine (with its single hydrogen atom side chain) is small enough to exist in the core of the helix [21]. The X and Y amino acids are non-glycine amino acids, and are often proline and its post-translational modification hydroxyproline [24, 25].

The synthesis of individual collagen molecules starts within the cell [26, 27], where individual procollagen α-chains ~ 1000 amino acids in length are first formed. Each α-chain has a C and N terminal. Three α-chains come together to form the procollagen molecule, and the C-terminus controls which α-chains come together [28]: aggregation is initiated by the formation of di-sulfide bonds in the C-terminus [29]. In the case of collagen type I, which is the most prevalent type in tendon, two $\alpha 1$ and one $\alpha 2$-chains form the procollagen molecule, which has a central triple helical region, as well as nonhelical propeptide regions at both C and N terminals. The triple helical conformation is stabilized by hydrogen bonding between its constituent α-chains [30], and post-translation modification of prolines and lysines are important for thermal stability [31] and cross-linking [32, 33], respectively.

After formation of the triple helix, procollagenases cleave the N and C propeptide regions [34], leaving a triple helical collagen molecule ~ 300 nm in length with short, nonhelical regions remaining at both C and N terminals (Figure 1.2, adapted from [27]). The remaining nonhelical telopeptide regions are important for cross-linking between molecules.

Once the propeptide regions have been cleaved, collagen molecules aggregate into fibrils that are 50-500 nm in diameter and millimeters in length [35]. Lateral aggregation is driven by non-covalent interactions: periodic hydrophilic regions [36] on each molecule enable energetically favorable lateral aggregation, where molecules are offset longitudinally in relation to their neighboring molecules. As multiple neighboring collagen molecules adopt this conformation, a 67 nm repeating structure of alternating molecular density is formed [37]. This periodic structure is known as the D-band, which consists of a gap (4/5 molecular density) and an overlap (5/5 molecular density) region [38]. Collagen molecules first organize into units of five molecules in cross-section, which are termed microfibrils [39, 40, 41, 42]. Upon further aggregation, D-periodic subfibrillar structures termed fibril segments (lengths $\sim 10~\mu$m)

3

are formed [43], which then fuse together in end-to-end and lateral fashions to form a mature fibril [44, 45]. After the fibril is fully formed, there is still evidence of distinct subfibrils [46, 47].
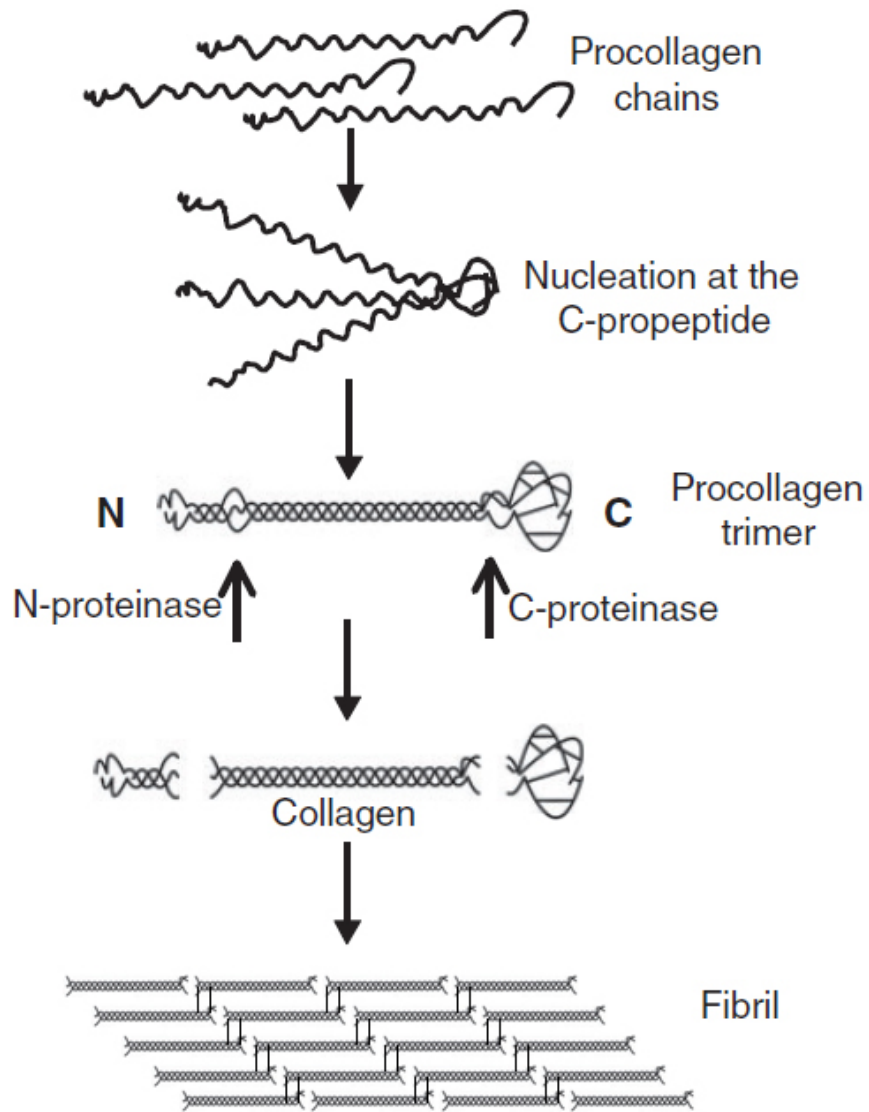
Figure 1.2: Synthesis of the triple helical collagen molecule and subsequent fibrillogenesis. Figure adapted from [27].

1.1.4 Cross-links

The tensile strength of collagen fibrils is mediated by covalent intermolecular cross-links [48], represented by black lines connecting molecules in Figure 1.2. In fibril-forming collagens, the enzyme lysyl oxidase reacts with the side-chain of lysine or hydroxylysine [49], replacing an amino group with an aldehyde that can then react with a specific amino group from a neighboring molecule. When initially formed, cross-links are thought to be divalent in nature, and are termed immature. Over time, divalent cross-links can react with a third collagen molecule, and become trivalent, mature cross-links [50, 51]. Inhibition of lysyl oxidase activity, which occurs with dietary intake of β-aminopropionitrile [52], decreases the ultimate strength of whole rat tail tendons [53] and causes a plateau in stress-strain behavior, indicative of unhindered sliding [54]. In contrast, inducing additional cross-links via glutaraldehyde treatment [55] has the opposite effect, and stiffens fascicles and fibrils [56]. Interestingly, cross-linking fibrils with glutaraldehyde has a different effect than cross-linking with a carbodiimide. This is thought to be associated with the length of the cross-link: carbodiide-induced cross-links are "zero length", while glutaraldehyde cross-links have a non-zero length [42]. With more length, the glutaraldehyde induced cross-links have a greater capacity for intermolecular connections.

In addition to enzymatically derived cross-links, there are non-enzymatic cross-links called advanced glycation end-products (AGEs). AGEs are formed in the presence of a reducing sugar, and accumulate with age [57].

1.2 SDFT-CDET model

The best characterized energy storing - positional tendon model is the forelimb superficial digital flexor tendon (SDFT) and common digital extensor tendon (CDET) pair, which has been studied in the bovine and equine model [4, 58, 59, 60]. The SDFT is located posterior to the CDET [61] (Figure 1.3, adapted from [58]). Assuming a maximum muscle stress of 0.3 MPa, and measuring the cross-sectional areas of muscles and tendons, Ker *et al.* [3] estimated the maximum *in vivo* stresses that tendons would receive. The bovine SDFT is estimated to be have a 7x higher maximum *in vivo* stress than the CDET [3]. The difference in maximum stress between the bovine

SDFT and CDET pair is mirrored in the equine model [3], which is sensible given that they are both large quadripeds. The bovine SDFT has significantly less hysteresis than the CDET [62], showing that it is the better energy storing device. Similarly, fascicles from the equine SDFT have significantly less hysteresis than CDET fascicles [60].
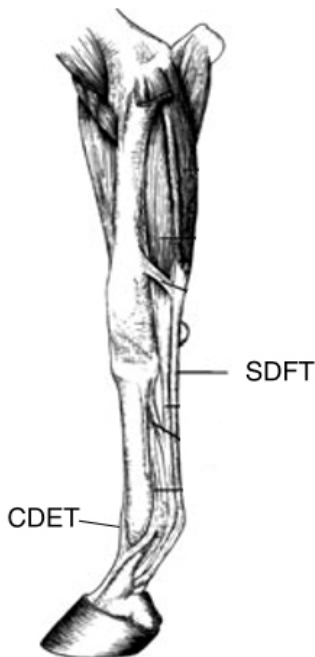
Figure 1.3: Anatomical diagram of the forelimb, showing positions of the SDFT and CDET. Figure adapted from [58].

1.2.1 Inherent structural differences

Two thermal techniques have revealed distinct molecular packing and cross-linking in the bovine SDFT and CDET. First, differential scanning calorimetry (DSC) is a technique capable of measuring the energy absorbed by a material during heating. Heating collagen through its helix to coil transition produces a denaturation endotherm, which provides useful information on collagen folding and packing within fibrils. The SDFT endotherm had a higher peak temperture and a smaller full-width-at-half-maximum than the CDET endotherm, indicating that the SDFT has more tightly packed molecules on average, and a narrower distribution of intermolecular

spacing, respectively (Figure 1.4A, adapted from [62]). Second, hydrothermal isometric tension (HIT) anaylsis is a technique used to probe collagen molecular packing and thermomechanical properties of cross-links. By restraining a tendon at a constant length between two sample grips in a water bath, and measuring the tensile force generated between the grips as the bath is heated up to 90 °C, the stability of molecules and cross-links are probed (Figure 1.4B, adapted from [62]). For a given molecular packing density, there is a denaturation temperature at which the triple helical conformation of the collagen molecules is no longer thermodynamically stable. Isolated collagen molecules denature near 37 °C [63], but are thermally stabilized in the fibril due to the polymer-in-a-box mechanism, in which neighboring molecules form the box [64]. The denaturation temperature is significantly larger in the SDFT than in the CDET, indicating that the molecular packing is more dense in the SDFT [62]. Above the denaturation temperature, the three α-chains dissociate from one another, and are entropically driven to adopt a random coil conformation instead of a triple helix. The entropically driven contraction is inhibited by the presence of cross-links between neighboring α-chains, and tension is generated in the tendon. The tension increases linearly with temperature, in accordance with rubber elastic theory [65], until the cross-links themselves become thermally disrupted. At this point, the tension stops increasing linearly, as mechanical continuity is thermally disrupted. In the SDFT, the tension continually increased during heating to 90 °C, showing a high content of thermally stable cross-links. In contrast, tension in the CDET during the HIT temperature ramp reached a maximum and declined afterwards, showing a high content of thermally labile cross-links (Figure 1.4B). Both trivalent cross-links and divalent keto-amine cross-links are thermally stable [66]; quantification of chemical cross-linking has indicated that the mature cross-link hydroxylysyl pyridinoline (HP) is prevalent in the SDFT [67], and exists in significantly greater quantities in the SDFT than the CDET [58].

SEM has been used to show that the bovine SDFT fibrils are significantly smaller in diameter than CDET fibrils (80 vs. 134 nm), and have a significantly shorter crimp wavelength (57 vs. 124 μm) [62]. When the noncollagenous matrix components were quantified in the equine model, the SDFT showed a large glycosaminoglycan (GAG) and water content [4], which is sensible since GAGs are thought to be tissue organizers

and hold water [10]. When viewed under SEM, there was a thick meshwork composed of thin filaments that lacked D-banding and connected fibrils laterally in the bovine SDFT, which was absent in the CDET [62]. There is a greater DNA content in the equine SDFT than CDET, which is indicative of greater cellularity, while fluorescence measurements suggest that the tissue turnover rate is slower in the equine SDFT than CDET [58].
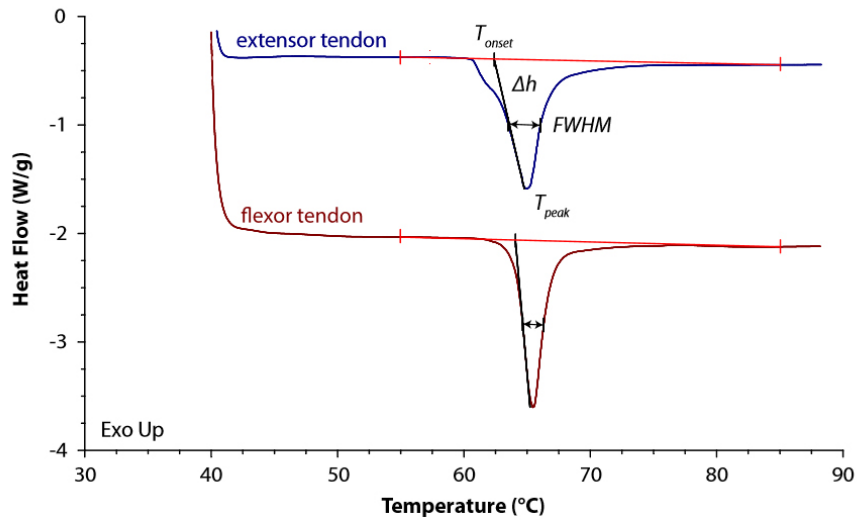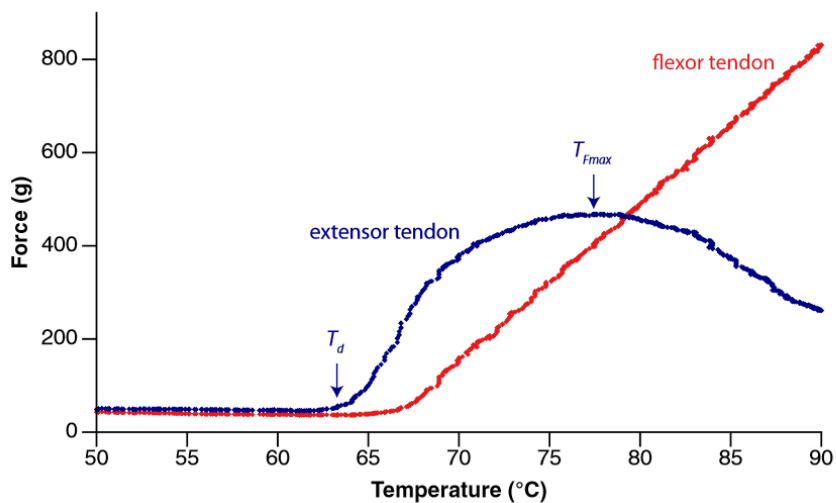
Figure 1.4: Thermoanalytical techniques at the tendon level: A) Endotherms of denaturation, and B) hydrothermal isometric tension curves, measured on the bovine SDFT and CDET. Figure adapted from [62].

1.2.2 Distinct fibrillar response to tensile testing at the tendon level

The SDFT and CDET have distinct structural responses to tensile testing. In response to a single pull to rupture at a strain rate of 10%/s, scanning electron microscopy (SEM) revealed that the constituent fibrils of the CDET were typically damaged, having undergone plastic deformation (Figure 1.5A, C, adapted from [62]). In contrast, SDFT were largely intact, demonstrating proper D-banding and no plastic deformation (Figure 1.5B, D, adapted from [62]).

This distinct structural response was similarly observed when the fibrils in the SDFT and CDET were investigated in response to 1000 loading cycles at 30% of their ultimate tensile strength. SDFT fibrils were robust against plastic damage after 1000 loading cycles, demonstrating significantly better fatigue resistance than CDET fibrils, which were heavily disrupted by cyclic loading [62]. The damage incurred on CDET fibrils in response to tendon rupture and cyclic tensile testing is morphologically similar to discrete plasticity damage observed in bovine tail tendon (BTT) fibrils [68, 69]. The bovine CDET and BTT share post-rupture damage morphologies, and have similar cross-linking as indicated by HIT [70, 62]. In contrast, the bovine SDFT is robust against damage and has a different HIT curve than the CDET and BTT [62], suggesting that cross-linking may control mechanisms of plastic damage.
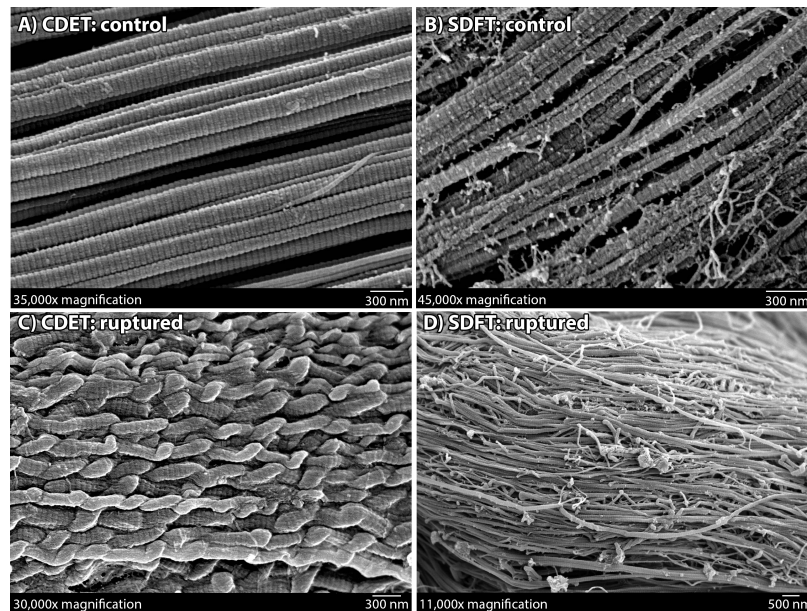
Figure 1.5: Tendon level morphological response of the bovine SDFT (A, C) and CDET (B, D). Figure adapted from [62].

1.2.3 Mechanical differences at the tendon level

One of the simplest tests to determine mechanical properties is a single pull to rupture. When loaded, the SDFT and CDET both demonstrate the characteristic progression of toe, heel, linear, and plastic regimes. The toe regime occupies the initial few percent, and corresponds to straightening of the crimp. The heel regime corresponds to straightening of microscopic bends in molecules, and the linear regime is due to loading of the aligned and straight molecules [54]. Above the linear regime there is the plastic regime, where the modulus decreases as the tendon is plastically deformed. The SDFT and CDET show distinct rupture properties: the SDFT has a significantly lower strength (23 vs. 38 MPa) and toughness (7 vs. 14 MJ/M^3) than the CDET (Figure 1.6A, adapted from [62]). In the equine model, the SDFT has a greater failure strain (23 vs. 19 %), lower failure stress (115 vs. 157 MPa), and lower modulus (614 vs 1012 MPa) than than the CDET [59].

Another mechanical distinction between the bovine SDFT and CDET that is not captured by the single pull to rupture, is observed for cyclic loading. The SDFT has significantly less hysteresis than the CDET, up to 1000 loading cycles (Figure 1.6B, adapted from [62]), which is the most direct evidence that the SDFT is a more efficient energy-storing tendon than the CDET.
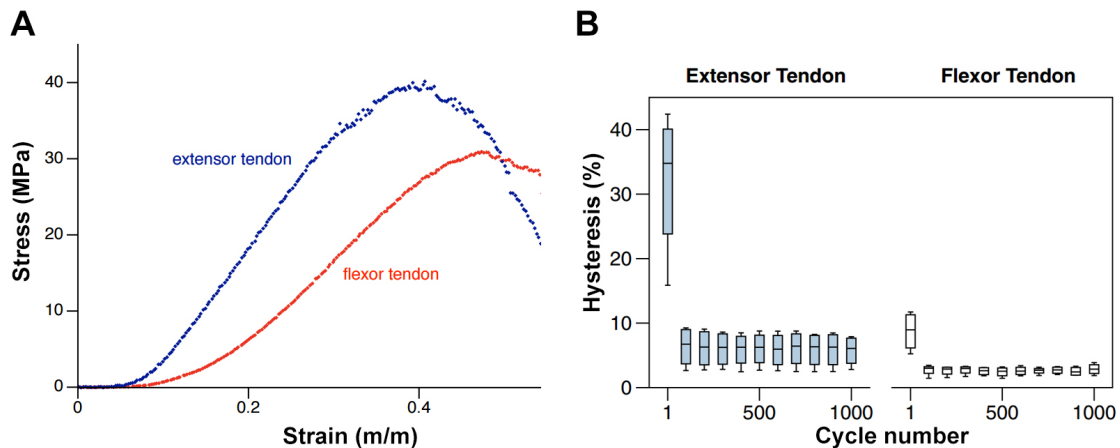
Figure 1.6: Tendon level mechanics of the bovine SDFT and CDET. A) pull-to-rupture stress-strain curves, and B) hysteresis measurements from cyclic testing. Figure adapted from [62].

1.3 Atomic force microscopy: basic operation

An atomic force microscope (AFM) enables interaction with matter below the nanoscale [71, 72], and was used for fibril imaging and manipulation in the current work. An AFM probe consists of a horizontally oriented cantilever arm and a vertically oriented tip, which is the point of interaction with a sample (Figure 1.7). The interaction is mediated through a feedback loop based on the output of the photodiode: deflection in the AFM cantilever changes the position of the reflected laser, altering the output of the photodiode. In the AFM that I used, the (x, y) position of the stage and the (z) position of the AFM probe are controlled by piezoelectric elements, enabling accurate control of the tip-sample interaction.

An AFM can operate in contact or tapping mode, which enable different types of measurements. In both modes of operation, the interaction of the AFM tip and sample is monitored and controlled by reflecting a laser off the back of the AFM cantilever onto a four quadrant photodiode (Figure 1.7). Contact mode enables lateral manipulation [73], which was used in the current work to measure mechanical properties of fibrils pulled to rupture. As the name suggests, the AFM tip is in contact with the sample throughout the whole process when operating in contact mode, and the scanner is moved in the (z) direction at each (x,y) position to maintain a constant degree of cantilever deflection. Maintaining a constant normal deflection while allowing the lateral deflection to vary as the AFM tip moves enables lateral force measurements.

Tapping mode enables nanoindentation imaging, which was used in the current work to determine structural features of fibrils. Here, the scanning AFM tip is not in contact with the surface at all times, but oscillates in and out of contact with the sample [74]. The scanner is moved in the (z) direction at each (x,y) position to maintain a constant oscillation amplitude, across sample features of varying heights.
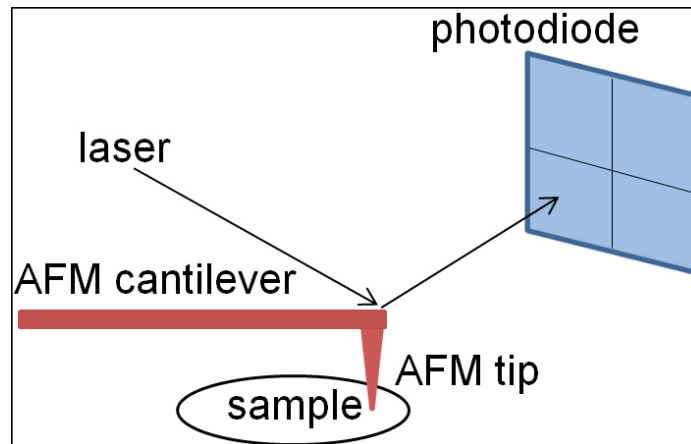
Figure 1.7: Schematic diagram of the AFM tip interacting with a sample, using the laser position on a four quadrant photodiode as the feedback parameter.

1.4 Testing of single fibrils

1.4.1 Available techniques

There are a number of single fibril studies that have been performed over the last decade, and I will address the capabilities and contributions of each of technique.

AFM nanoindentation imaging

The first type of single fibril investigation enabled by atomic force microscopy was through nanoindentation imaging. Sharp bends were observed in 10 μm AFM images of fibrils, evidence of a tubelike fibrillar structure in which a less dense core is surrounded by a more dense shell [75]. Analysis of individual nanoindentation force-curves revealed that the radial modulus of fibrils is highly dependent on hydration level, changing by three orders of magnitude between dehydrated and hydrated conditions [76], and is sensitive to the ionic content in solution [77]. Absorption of water preferentially occurs in the gap regions rather than the overlap, such that there is little difference in height between the gap and overlap in the hydrated state [78]. Despite the swelling heterogeneity, radial modulus measurements (extracted from high speed nanoindentations) are proportional to molecular density in the hydrated state, demonstrating a 4/5 gap/overlap ratio [38].

AFM bending

The second type of single fibril investigation achieved via atomic force microscopy was micro-mechanical bending. Single fibrils suspended across a micro-channel were loaded with a tipless cantilever, in a vertically oriented 3-point bending experiment [79, 80]. Bending experiments of this nature showed that the the bending modulus of a hydrated fibril exceeds the shear modulus by a factor of two orders of magnitude [80].

AFM vertical force spectroscopy

The third type of AFM investigation is vertically oriented force spectroscopy, which has been used to study tensile properties of single fibrils. By gluing both ends of an isolated fibril down, followed by attaching one glue spot to the AFM tip and peeling the fibril from the surface, a tensile test can be performed on the fibril (Figure 1.8, [42]). The force is calibrated by measuring the normal spring constant of the cantilever. This method has been used to investigate low strain behavior [81, 82, 83], and can also achieve fibril rupture [84].
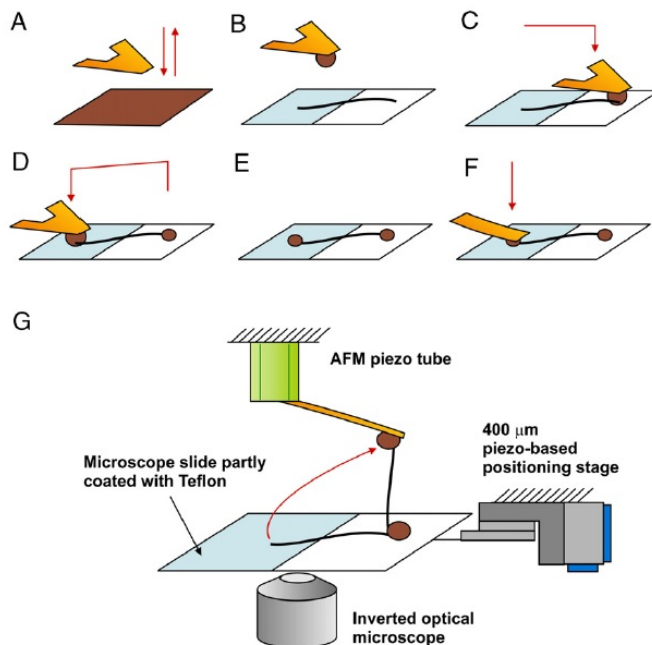
Figure 1.8: Schematic of tensile testing experiment, achieved by AFM on a single fibril through vertical force spectroscopy. Figure adapted from [42].

Microelectromechanical systems

Microelectromechanical (MEMS) devices have been used to investigate the tensile properties of single fibrils. By suspending a single fibril across a channel (Figure 1.9, adapted from [85]) in which one attachment point can be moved by an electrostatic comb-drive actuator, uniaxial tensile testing is possible [86, 87, 88, 89, 85]. The force produced by the actuator is calibrated by measuring the voltage-displacement response of the device without a fibril in place relative to the stiffness of tether beams, which was calculated using large deformation finite element analysis [86].
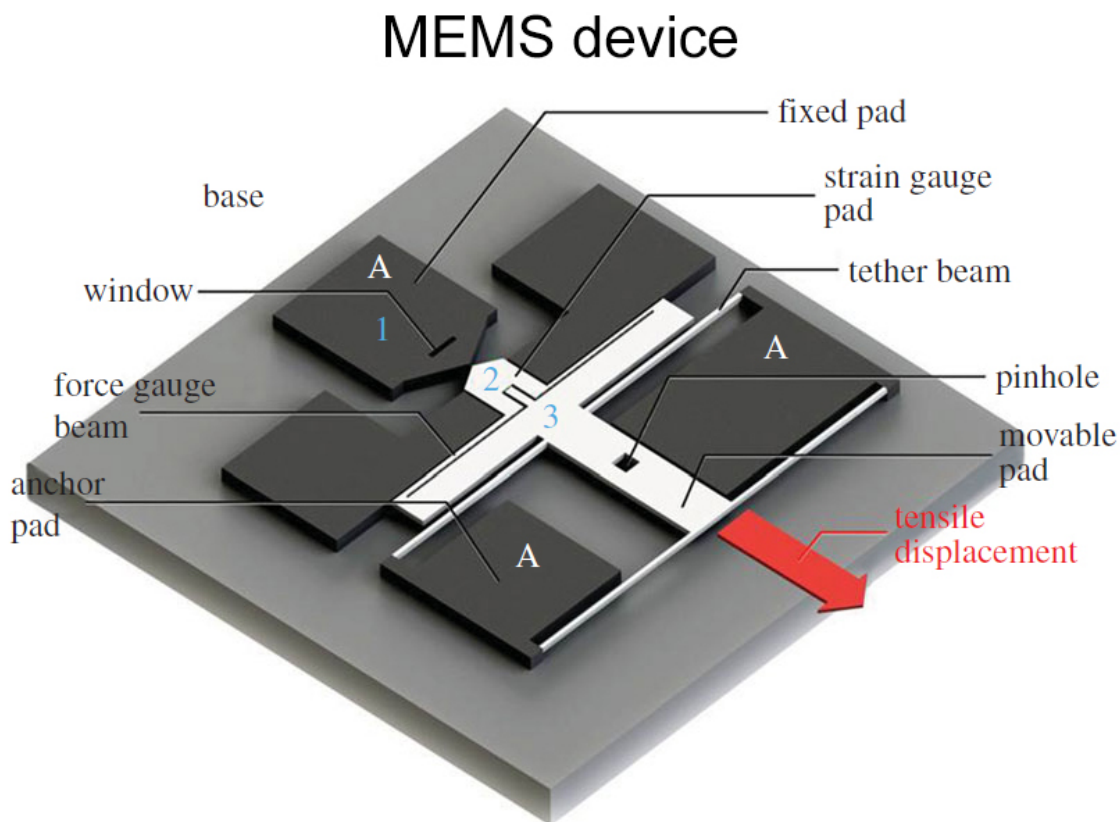
Figure 1.9: Schematic of tensile testing experiment via MEMS based device on a single fibril. Figure adapted from [85].

1.4.2 Previous fibril rupture studies

Fibril rupture: AFM vertical force spectroscopy and dehydrated AFM imaging

Using AFM force spectroscopy, the rupture mechanics of human patellar tendon (HPT) and rat tail tendon (RTT) fibrils were investigated [84]. HPT fibrils had a signficantly higher rupture stress (540 vs. 250 MPa) and modulus prior to rupture (4.3 vs. 1.6 GPa) than RTT fibrils, and they had similar rupture strains 17-20 % (Figure 1.10A, adapted from [84]). The difference in stress-strain behavior between HPT and RTT fibrils was thought to be due the signficantly greater levels of mature cross-linking in the HPT than RTT [84]. The mechanical properties elucidated in the current work on bovine SDFT and CDET fibrils are compared to measurements of Svensson *et al.* [84].

In the same study, post-rupture dehydrated AFM imaging revealed two characteristic fibril states: fibrils were either intact, demonstrating undisrupted D-banding along their length, or were heavily disrupted. Disrupted fibrils appear to have separated a disordered shell from a zig-zagging fibril core (Figure 1.10B, adapted from [84]).
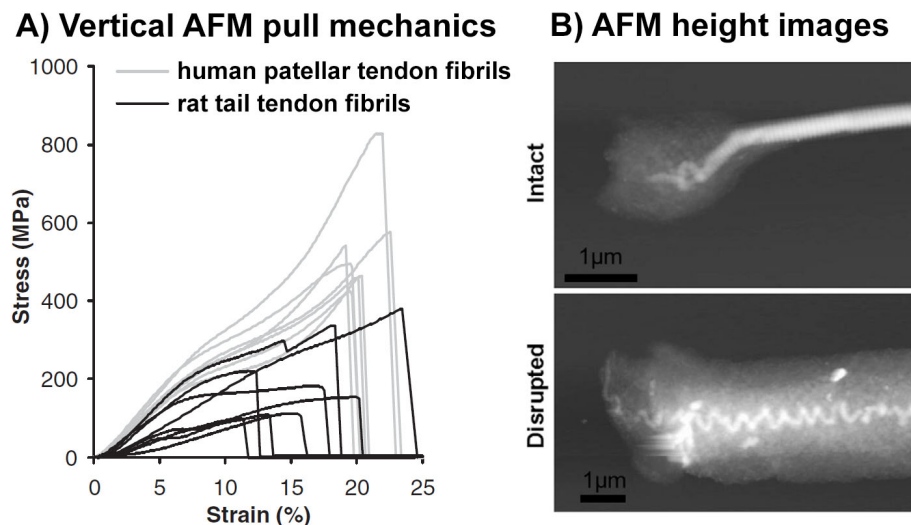
Figure 1.10: A) Stress-strain curves of single fibrils from different tendon types measured by vertical AFM force spectroscopy. B) Post-rupture dehydrated AFM images. Figure adapted from [84].

15

Fibril rupture: MEMS and SEM

Recently, a MEMS based rupture study was performed on rat patellar tendon (RPT) fibrils [85]. RPT fibrils demonstrated a graceful failure, fracturing at strains >60% with an ultimate stress ~70 MPa (Figure 1.11A, adapted from [85]). The mechanical properties elucidated in the current work on bovine SDFT and CDET fibrils are compared to measurements of Liu *et al.* [85].

After failure, SEM revealed that most of the fibril was intact, exhibiting a single fracture plane where damaged was highly localized (Figure 1.11B, adapted from [85]).
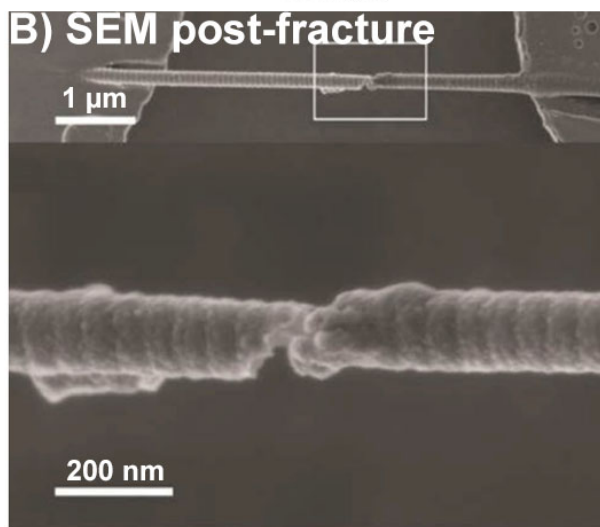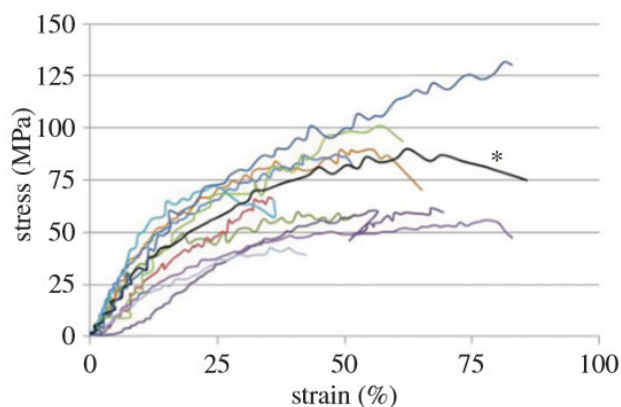
Figure 1.11: A) Stress-strain curves of single rat patellar tendon fibrils measured by MEMS based devices. B) Post-fracture SEM images of fibril damage. Figure adapted from [85].

1.5 Second harmonic generation

1.5.1 Underlying physics

Second harmonic generation (SHG) is a nonlinear optical scattering process, which arises when a material has a nonzero second order electric susceptibility, or hyperpolarizability [90, 91]. Noncentrosymmetric crystalline (or quasi-crystalline) materials lack inversion symmetry, and demonstrate hyperpolarizability. When two photons of a single wavelength are incident on such a material, a single photon with twice the incident energy is emitted (Figure 1.12).

Second harmonic generation

virtual state

incident photon ω

virtual state

outgoing photon 2ω

incident photon ω

electron ground state
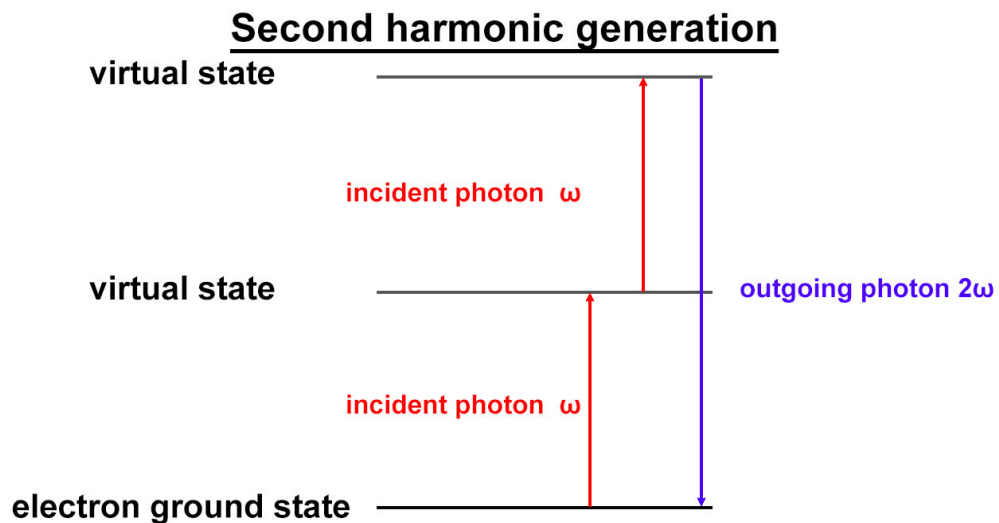
Figure 1.12: Electron energy level diagram for second harmonic generation. Two incident photons with frequency ω are combined into a single photon with frequency 2ω.

1.5.2 Collagen SHG

Collagen fibrils are known to demonstrate SHG [92, 93, 94, 95], due to the noncentrosymmetric geometry of the triple-helix, and electrons in the peptide bonds in the α-chains are the SHG harmonophores [96, 97, 98, 99, 100]. SHG in collagen is highly polarization dependent, and the highest intensity is achieved when the incident incident laser polarization is parallel with the fibril axis (Figure 1.13, adapted from [95]). Polarization-corrected SHG measurements are possible if multiple images are taken of a given sample as the incident polarization is incrementally rotated through 90 °C.

A) Tendon SHG

B) Polarization dependent intensity
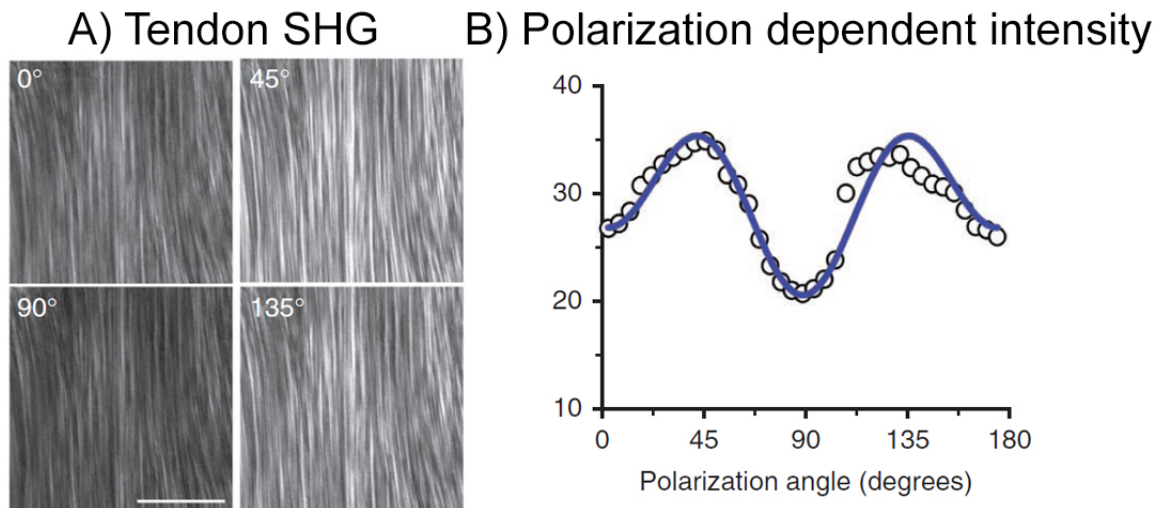
Figure 1.13: A) Second harmonic generation images from mouse tendon with rotated incident polarization, and B) plot of polarization dependent SHG intensity. Figure adapted from [95].

SHG is sensitive to the molecular state of collagen, and has been used to investigate the thermal denaturation of collagen molecules in a number of tissues [101, 102, 103, 104]. More recently, single fibril resolution has been achieved via SHG, and has been used to quantitatively investigate single fibrils [105]. With the sensitivity of SHG to triple helical molecular conformation and single fibril resolution both established, we sought to utilize SHG to investigate rupture-induced structural response in single SDFT and CDET fibrils.

Chapter 2

Research questions and hypotheses

The overarching goal of this project was to investigate the mechanical behavior and structural response to rupture of single fibrils extracted from different tendons. With the growing body of literature on the SDFT and CDET tendon pair in which mechanical and structural differences have been observed, I sought to determine if mechanical and structural differences also exist between the individual collagen fibrils making up these two tendons. For my investigation, there were four main research questions and associated hypotheses:

Q1) Do single fibrils from the bovine SDFT and CDET exhibit distinct stress-strain curves when pulled to rupture? Hypothesis: Previous testing of whole tendons to rupture has shown that the CDET is significantly stronger and tougher than the SDFT. Therefore, it is predicted that collagen fibrils from the CDET will be significantly stronger and tougher than fibrils extracted from the SDFT.

Q2) Do single fibrils from the bovine SDFT and CDET exhibit distinct post-rupture structures? Hypothesis: When whole tendons are pulled to rupture, previous research has shown that collagen fibrils from CDET undergo discrete plasticity, while those from SDFT do not sustain plastic damage. Therefore, it is predicted that when ruptured as single fibrils, fibrils from CDET will undergo plastic damage, but those from SDFT will not.

Q3) Is rupture-induced formation of plastic damage on fibrils associated with increased toughness or extensibility? Hypothesis: It has been proposed that discrete plasticity is strain induced, and could be a toughening mechanism for fibrils by which energy is absorbed by selective molecular failure [68]. Therefore, it is predicted that rupture strain and toughness will be correlated with the amount of plastic damage post-rupture.

Q4) Is the post-rupture molecular order in single fibrils from the bovine SDFT and CDET distinct? Since CDET fibrils undergo discrete plasticity while SDFT fibrils do not, and discrete plasticity damage is asociated with molecular disruption, it is predicted that molecular order will be better preserved post-rupture in single SDFT

fibrils than CDET fibrils.

Chapter 3

Materials and Methods

3.1 Overview

The mechanical behavior and structural response of 38 individually ruptured collagen fibrils were characterized. An overview of the experimental process is shown in Figure 3.1. I performed all tissue dissections, mechanical testing, and atomic force microsopy imaging. Second harmonic generation imaging was then performed on the ruptured fibrils by Stéphane Bancelin at the Institut National de la Recherche Scientifique in Varennes, Québec.

Experimental flow

SDFT

CDET

Extract SDFT and CDET tendons
from one forelimb of one 24-36 month old steer and decellularize
Store at 4 °C in sterile 1x PBS with antibiotic-antifungal

Dissect tendon in 1x PBS
Pipette 1 mL of PBS/fibril mixture onto sample dish
Leave dish on shaker table for 30 minutes

Triple rinse dish using deionized water
Dehydrate dish in desiccator for minimum 24 hours

total time
to complete
10 fibrils:
2 weeks

total time
to complete
two tendons:
4 weeks

total time
to complete
two steers:
8 weeks

Apply glue to fibrils
Measure dehydrated cross sectional area
Hydrate in 1x PBS for minimum 1 hour

Pull fibrils to rupture using AFM

Dehydrate in desiccator for minimum 24 hours
Dehydrated AFM imaging
Store in desiccator

Repeat process for CDET

Repeat entire process on second steer, test CDET before SDFT

Second harmonic generation imaging on ruptured fibrils at the Institut National de la Recherche Scientifique

Figure 3.1: Experimental flow diagram.

3.2 Tendon acquistion and decellularization

Tendons from two animals were used in this study: the SDFT and CDET tendon pair was extracted from one forelimb per animal of two 24-36 month old steers, collected fresh from a slaughterhouse (Oulton's farm, NS, Canada). Forelimbs were transferred on ice to the laboratory for dissection. The tendons used were never frozen. A scalpel was the primary tool used for cutting through the forelimb hide, removing nontendinous material, and acquiring a piece of the desired tendons. Both the SDFT and CDET were removed from each of the two dissected forelimbs (Figure 3.2). A 3 cm long piece was taken from each tendon, away from the bone and muscle insertions. The 3 cm length was selected to keep the pieces manageable with tweezers for fibril extraction. After removal from the forelimb, each tendon was placed in a 50 mL Falcon tube filled with 1x phosphate buffered saline (PBS) solution plus 1 % amphotericin B (0.25 μg/mL) and 1% penicillin-streptomycin (pen-strep) (100 units/mL pen, 0.1 mg/mL strep), labelled with animal, tendon, and solution contents.
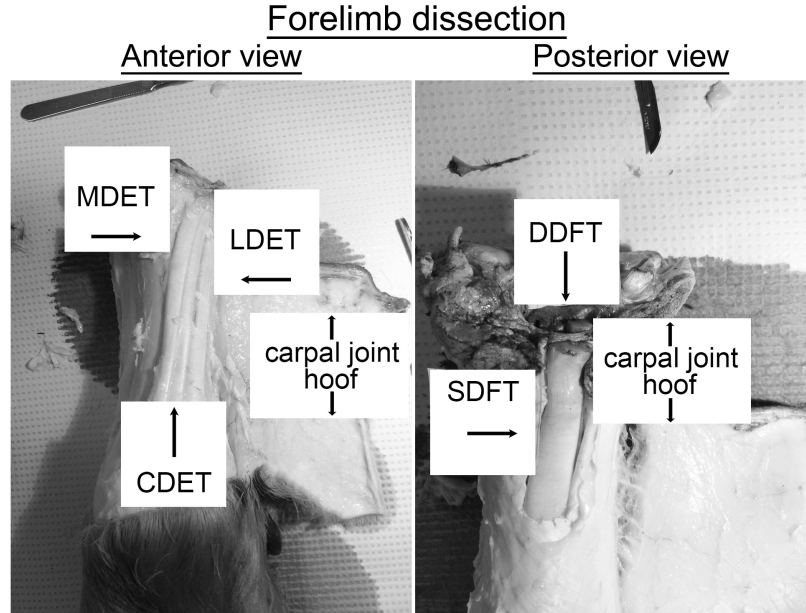
Figure 3.2: Photographs taken during the dissection of a bovine forelimb, showing the anatomical position of the SDFT and CDET forelimb tendons. The CDET, located between the MDET (medial digital extensor tendon) and LDET (lateral digital extensor tendon) was extracted from the anterior side. The SDFT, located closer to the surface than the DDFT (deep digital flexor tendon), was removed from the posterior side.

Each tendon went through a decellularization process based on the work of Ariganello *et al.* [106], which was required to enable the removal of SDFT fibrils. The seven day process consisted of washing the tendons in specific solutions, with each wash conducted on a shaker table. For steps performed in the flowhood, solutions were kept in autoclaved glassware for sterility. Decellularization was a seven day process:

Day 1:

After removing the SDFT and CDET from the forelimb, each tendon underwent three 30 minutes washes at room temperature in a labelled 50 mL Falcon tube of 1x PBS solution plus 1 % amphotericin B and 1% pen-strep.

Solution A, intended to lyse cells while inhibiting enzymatic digestion of collagen, was prepared (2 L total volume):

- in 1900 mL sterile water, dissolved:

- 2.41 g Tris Base (10 mM)

- 2.92 g ethylenediaminetetraacetic acid (EDTA) (5 mM), then:

- adjusted to pH 8.0 using 0.1 NaOH/HCl stocks

- added 10 mL pen-strep

- added 700 μL phenylmethylsulfonyl fluoride (PMSF)

- topped up to 2 L with sterile water

- stored in fridge.

The tendons underwent three 12 hour washes at 4 °C in Solution A.

Day 2:

Solution B, intended to cleanse the tissue by removing cells and other noncollagenous material, was prepared (2 L total volume):

- in 1900 mL sterile water, dissolved:

- 12.12 g Tris Base (50 mM)

- 223.66 g KCl (1.5 M)

- 2.92 g EDTA

- 20 mL Triton-X-100 then:

- adjusted to pH 8.0 using 0.1 M NaOH/HCl stocks

- added 10 mL pen-strep

- added 700 μL PMSF

- topped up to 2 L with sterile water

- stored in fridge until use.

Day 3:

Solution A was exchanged for equal amounts of Solution B (50 mL). The tendons underwent two 12 hour washes at 4 °C in Solution B (50 mL).

Day 4:

Hanks' Solution, used as a buffer in enzymatic cocktails, was prepared (2 L total volume):

- in 1900 mL sterile water, dissolved:

- 16.00 g NaCl

- 0.80 g KCl

- 0.074 g Na_2HPO_4 (anhydrous, dibasic)

- 0.12 g KH_2PO_4

- 0.70 g $NaHCO_3$

- 5.20 g HEPES

- 2.44 g $CaCl_2$ (dihydrate)

- 0.10 g $MgSO_4$ (heptahydrate)

- 0.10 g $MgCl_2$ (hexahydrate), then:

- adjusted to pH 7.35 using 0.1 M NaOH/HCl stock

- topped up to 2 L with sterile water

- stored in fridge until use.

Solution C, intended to cleanse the tissue after enzyme cocktails, was prepared (2 L total volume):

- in 1900 mL sterile water, dissolved:

- 12.12 g Tris Base

- 20 mL Triton-X-100, then:

- adjusted to pH 9.0 using 0.1 M NaOH/HCl stocks

- topped up to 2 L with sterile water

- stored in fridge until use.

Aliquotes of DNase and RNase solutions were thawed at room temperature. These were intended to remove DNA and RNA released from the lysed cells. All tendons were washed in 50 mL of sterile water for 30 minutes at room temperature. Each of the following transfers was performed in a flowhood. The tendons were transferred to new 50 mL Falcon tubes containing Hanks' Solution, and washed for 30 minutes at room temperature. DNase and RNase solutions were added to a Hanks' Solution (0.1 mg/mL each). Tendons were transferred to Falcon tubes containing the enzyme cocktail, and then the sealed tubes were placed in a 37 °C water bath and shaken for one hour. The tendons were transferred to Falcon tubes containing Hanks' Solution (50 mL), and were washed for 30 minutes. The tendons were transferred to Falcon tubes containing Solution C (50 mL), and underwent two 12 hour washes at room temperature.

Day 5:

In flowhood, tendons were transferred to Falcon tubes containing sterile 1x PBS (50 mL) with 1% amphotericin B and 1% pen-strep, and underwent two 30 minute washes at room temperature, followed by a 46 hour wash at room temperature.

Day 6:

Nothing was required on this day.

Day 7:

Each tendon was transferred to a 50 mL Falcon tube containing sterile PBS with 1% amphotericin B and 1% pen-strep. This was the end of the decellularization procedure, and tendons were stored at 4 °C for a maximum of 2 weeks prior to fibril extraction.

3.3 Collagen fibril extraction

To extract single collagen fibrils, a 3-cm-long piece of decellularized tendon was placed in 20 mL of 1x PBS in a plastic dish with a radius $\sim$ 5 cm. The fibril extraction procedure took place at room temperature. Using a razorblade, a central rectangular plug was cut from each tendon, which was free of epitenon (Figure 3.3). Single fibrils were separated from this tendon plug and released into the surrounding PBS solution via the following technique, which was found to be best for extracting a large number of fibrils of the desired length ($\geq$ 100 μm). First, the rectangular plug was sliced longitudinally using the razorblade, and the tendon was splayed open along the cut using metal tweezers to reveal the inner substance of the plug. Then, the exposed inside of the plug was scraped with the razorblade for 10 minutes, which released fibrils into the surrounding fluid. The resulting collagen fibril/PBS mixture was distributed in 1 mL aliquots via plastic pipette among 10 glass sample dishes, each with radius 3 cm. (The splayed tendon structure maintained approximately 10 of the 20 mL of PBS used, so 10 dishes were made per tendon using the 10 mL of fibril/PBS mixture not bound by the splayed tendon.) The fibril/PBS mixture was left on the glass dishes for 30 minutes on a linearly shaking table (1 Hz), to facilitate parallel alignment between fibrils which adhered to the glass substrate. After 30 minutes, each dish was successively rinsed under agitation three times with 3 mL of distilled, deionized water to remove any salt, dried under compressed nitrogen, and stored in a desiccating chamber. The sole motivation for dehydrating at this stage was to glue fibrils to the glass substrate, which could not be achieved in a hydrated environment.

Collagen fibril extraction

Decellularized tendon sample   isolated central portion   extracted collagen fibrils
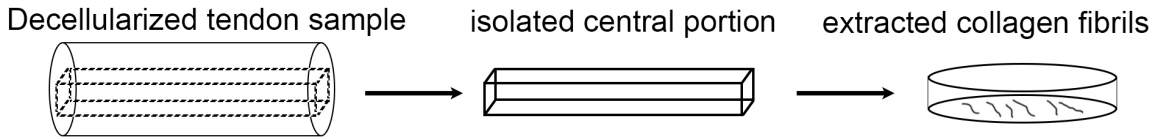
Figure 3.3: Fibrils extracted from tendon.

3.4 Pulling fine tipped glass rods

Fine tipped glass rods were used to apply two strips of glue to each fibril, to create a mechanically isolated fibril segment. Borosilicate glass capillaries with outer diameter of 1 mm and inner diameter of 0.58 mm (World Precision Instruments, USA) were heated and pulled using a vertical Kopf Pipette Puller (David Kopf Instruments, USA) to diameters smaller than 10 μm (the size of glue strips). The glass capillaries and the vertical Kopf Pipette Puller were generously supplied by Dr. Alan Fine (Department of Physiology and Biophysics, Dalhousie University).

3.5 Isolating collagen fibril segments

After being dessicated for 24 hours, straight single fibrils of at least 100 μm in length were identified (Figure 3.4A) using darkfield microscopy and a 10X, 0.3 NA objective (Olympus, Japan) and a WHK 10X/20L microscope eyepiece (Olympus, Japan). A fine tipped glass rod, controlled by a 3D hydraulic micromanipulator (Siskiyou Corp, USA), was placed in view above the glass dish, which was explored to find regions of parallel fibrils. Once a fibril was selected (Figure 3.4A), a large drop of 5 minute epoxy mix (LePage, USA) was placed at the edge of the sample dish. The glass rod was then dipped into the glue. Upon removal, the glass rod was pressed onto the glass substrate once to remove excess glue before attempting to apply glue strips to a fibril. Two parallel strips of glue, 50 μm apart and $\sim$ 10 μm wide each, were deposited perpendicularly across the selected fibril (Figure 3.4B-F). This procedure yielded a mechanically isolated fibril segment between the glue strips, and a segment outside of the glue for an unloaded control. After selecting and preparing multiple parallel

27

fibrils (5-10) on a glass dish in this manner, the sample was placed in the dessicator for a minimum of 24 hours prior to hydration.
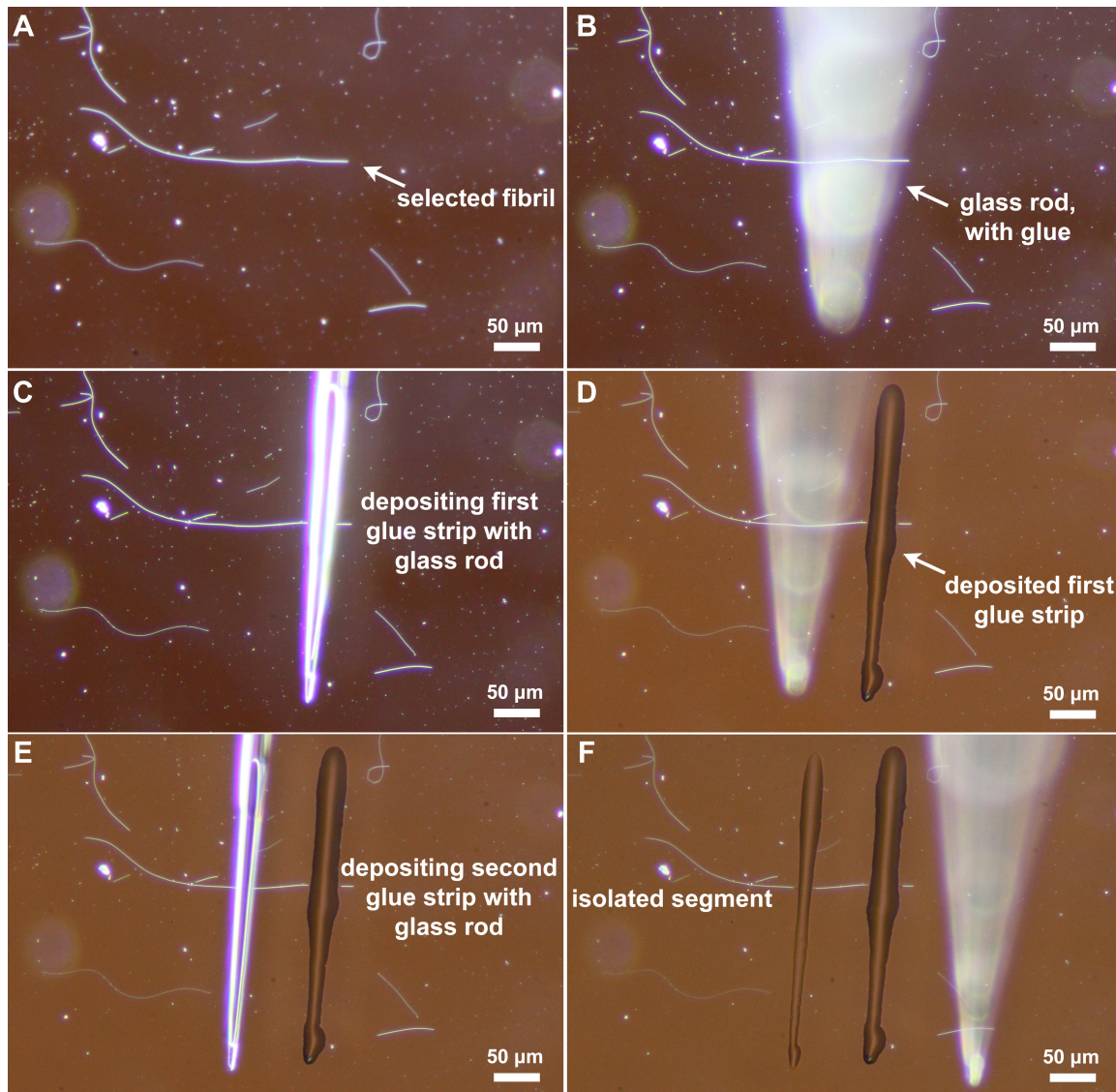
Figure 3.4: Step-by-step isolation of a fibril segment using a glass rod to deposit two strips of glue. Some brightfield illumination was used in addition to darkfield illumination in Panels D-F because the glue strips were better visualized that way.

3.6 Pre-loading dehydrated AFM imaging

A Catalyst AFM (Bruker, USA) was used in the current work. Working with a Bruker ScanAsyst fluid+ AFM probe (nominal spring constant 0.7 N/m), 500 nm long

images were taken using Bruker's PeakForce Quantitative Nanomechanical Mapping (QNM) mode to measure a cross-sectional profile of each unruptured fibril (Figure 3.5). Dehydrated imaging prior to rupture was performed with ~ 8 nm resolution, a tip indentation speed of 1200 μm/s, a 0.5 Hz raster scan frequency, and a peak force setpoint of 10 nN. The Step Tool included in Bruker Nanoscope 8.15 software was used to average 50 parallel cross sections together, yielding one average cross sectional profile. The thick white dotted box in Figure 3.5A shows the length and breadth of the area averaged over, and the thin dotted line shows the direction of the cross sectioning. Corresponding average cross sections are shown in 3.5B. The peak height and area under the curve were measured for each cross-sectional profile. The peak height was measured because it was the most directly comparable parameter between pre- and post-rupture states. Poisson's ratio is not well-defined for collagen, so the measured dehydrated cross-sectional area was used to convert tensile force into engineering stress.
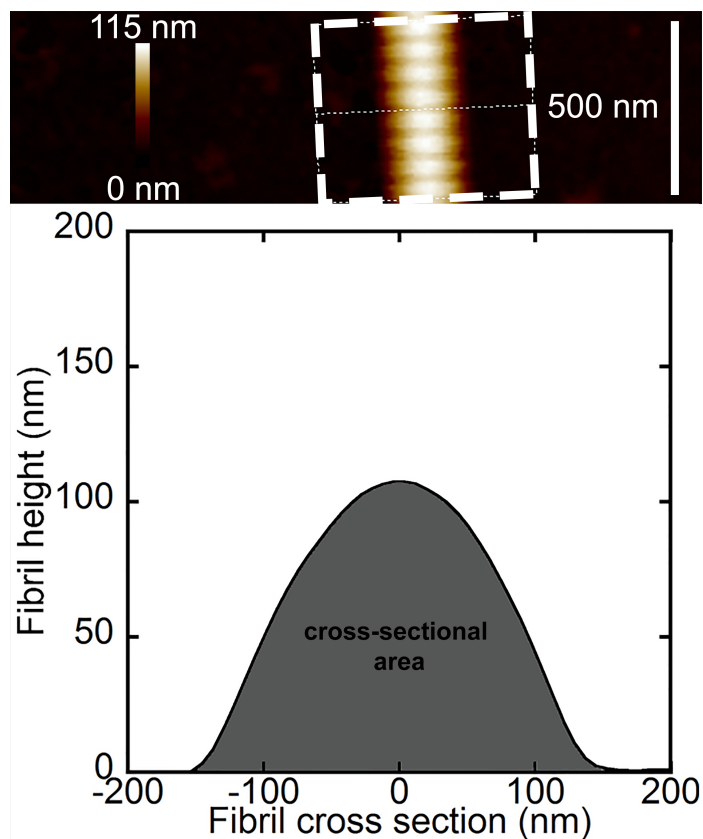
Figure 3.5: A) Pre-loading dehydrated AFM image of single fibrils and B) corresponding cross-sectional profile.

3.7 Bruker Tap525A AFM probe calibration

To calibrate the lateral force constant of the Bruker Tap525A probes used for fibril manipulations, the dimensions of cantilever length L, cantilever thickness T, and tip height H were measured using a Phenom G2 Pro scanning electron microscope (Phenom-World, Netherlands) (Figure 3.6). All probe dimensions were within the nominal range; $115 < L < 135$ μm, $6.0 < T < 7.5$ μm, and $15 < H < 20$ μm.
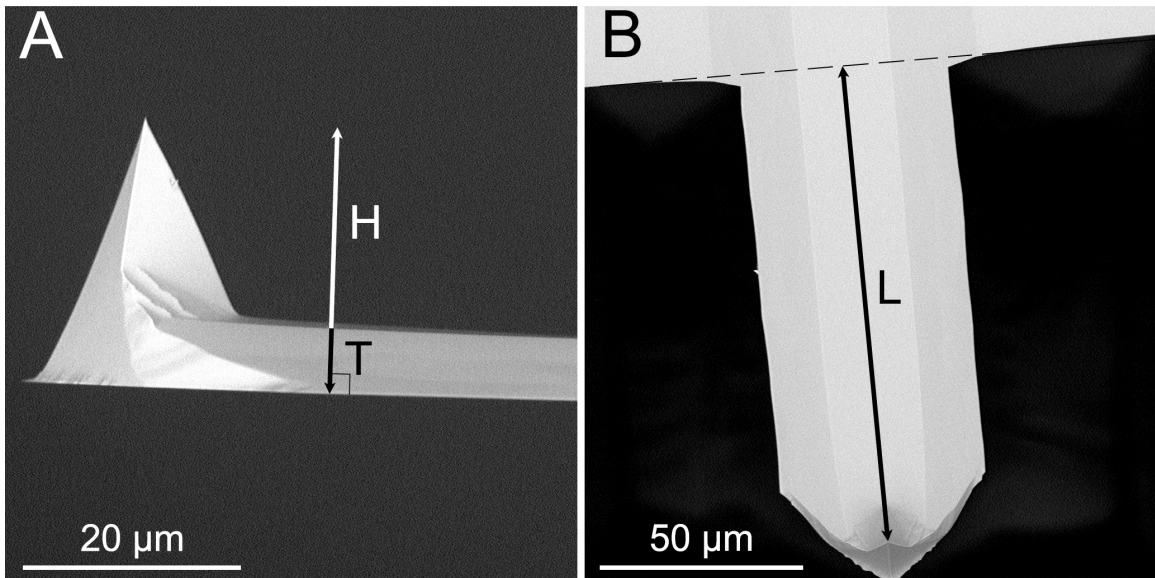
Figure 3.6: SEM images taken of a Bruker Tap525A AFM probe to measure its dimensions. A) the cantilever from a side view, used to measure cantilever thickness and tip height. B) the cantilever from a bottom view, used to measure the length of the cantilever arm to the tip.

Following these geometrical measurements, the probe was loaded into the AFM in a fluid probe holder. To calibrate the normal cantilever sensitivity, a force-displacement measurement was performed on a sapphire sample (hardness 9, Bruker PeakForce QNM Sample Kit) in which the vertical deflection [V] of the laser on the four quadrant photodiode was measured as a function of the probe height sensor [nm]. By fitting the contact regime (between vertical markers shown) the normal deflection sensitivity of the cantilever, S_z [nm/V], was measured (Figure 3.7). With this value, (characteristically 20 nm/V), the normal spring constant, K_z [N/m], was then calculated by the Nanoscope 8.15 software using the thermal method of Sader *et al.* [107] (characteristically 150 N/m). To achieve this, the cantilever was left to

oscillate under thermal motion far from the sample surface, the power spectrum of the cantilever's oscillation was measured, and the fundamental frequency peak was fit with a Lorentzian (Figure 3.8) [107].
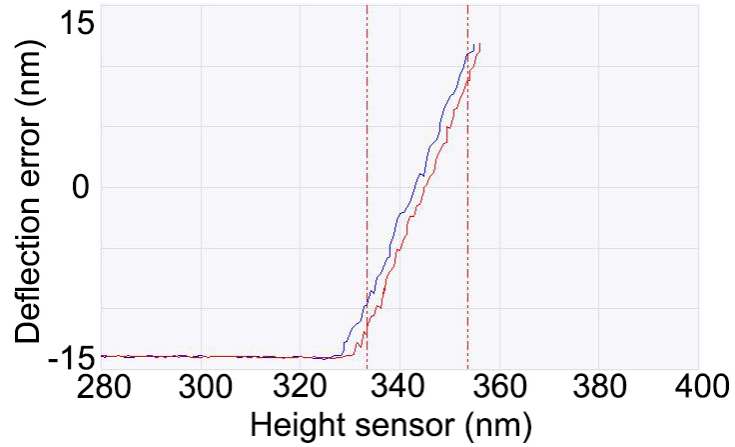
Figure 3.7: Approach (blue) and retract (red) curves for a Bruker Tap525A AFM probe on sapphire, used to measure the deflection sensitivity. It is worth clarifying that the Y-axis, while presented as deflection error in [nm], is equivalently a readout of the vertical deflection of the laser on the four quadrant photodiode [V] that has been converted to [nm] using an arbitrary sensitivity value stored in the software [nm/V].
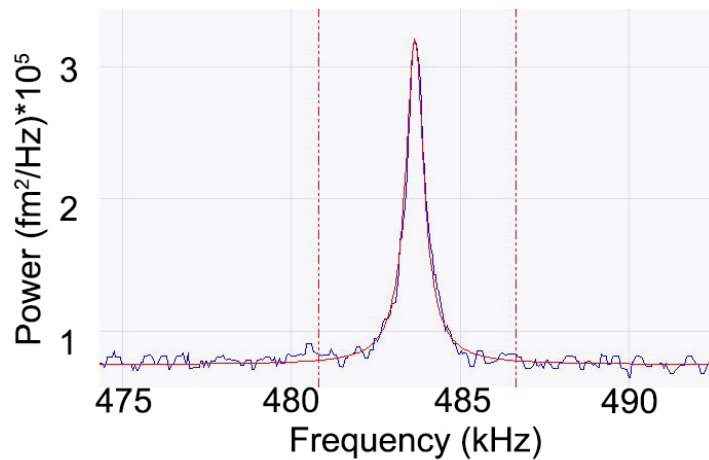
Figure 3.8: Resonance frequency peak in the power spectrum of a Tap525A AFM probe oscillating under the random driving forces of brownian motion of air particles, fit with a Lorentzian to determine the normal spring constant, K_z [N/m].

3.8 Tensile loading via AFM

38 fibrils were pulled to rupture in this work in a bowstring pulling geometry. Between 24 and 72 hours after gluing, a sample dish was removed from the dessicator, hydrated with 3 mL of 1x PBS for one hour, and placed on the stage of a Catalyst AFM (Bruker, USA) mounted on an IX71 inverted microscope (Olympus, USA). The orientation of the sample dish was selected such that the longitudinal fibril axis would be parallel to the axis of the AFM cantilever, which was fixed (Figure 3.9, adapted from [108]). Tensile loading was particularly sensitive to three contact mode parameters: the vertical deflection setpoint, the integral gain, and the proportional gain. The deflection setpoint controlled the normal force acting on the AFM tip by the glass substrate, the integral gain controlled the amount of integrated error signal used in the feedback loop, and the proportional gain controlled the amount of proportional error signal used in the feedback loop. I found that a deflection setpoint of 5 V (normal force at the tip of 15 μN), an integral gain of 1.4, and a proportional gain of 5.0 prevented the AFM tip from hopping over the fibril prior to rupture during extension.
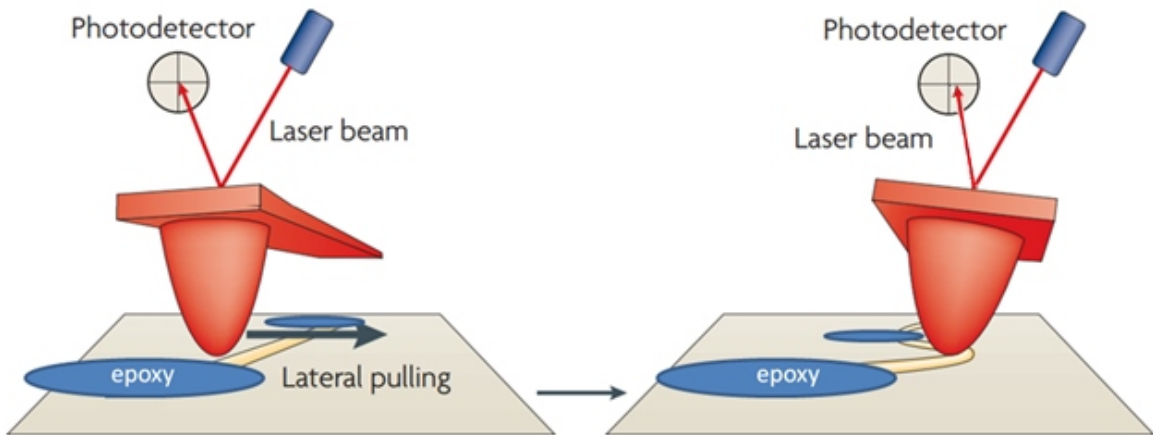
Figure 3.9: Schematic representation of the bowstring pulling geometry. The AFM cantilever axis was parallel to the fibril longitudinal axis, and the AFM tip was stationary in real space while the stage was moved under it. The force applied at the AFM tip, $F_{lateral}$, caused a horizontal laser deflection, $V_{lateral}$. Figure adapted from [108].

During the one hour sample hydration period, a calibrated Bruker Tap525A probe

was loaded onto the AFM and placed above an isolated fibril segment. The spatial relationship of AFM tip and fibril was resolved with brightfield microscopy, and images were recorded using a Grasshopper camera (Point Grey, Canada) operated at 20 frames per second. With the AFM cantilever axis parallel to the fibril axis (Figure 3.9), the tensile force acting on the AFM tip caused a lateral deflection, $V_{lateral}$, of the laser on the four quadrant photodetector. When a lateral force, $F_{lateral}$, acted on the AFM tip, the force caused a torque about the cantilever axis such that:

$$F_{lateral} = S_{lateral}K_{lateral}V_{lateral} \tag{3.1}$$

where $S_{lateral}$ [nm/V] was the lateral sensitivity, $K_{lateral}$ [N/m] was the lateral spring constant, and $V_{lateral}$ [V] was the lateral voltage deflection. I recast this relationship to give a direct relationship between $F_{lateral}$ and the measured values of S_z, K_z, and geometrical tip dimensions. First, $S_{lateral}$ was related to the normal sensitivity S_z [109]:

$$S_{lateral} = \frac{3(H + T/2)S_z}{2L} \tag{3.2}$$

where L, H, and T were the measured cantilever length, tip height, and cantilever thickness, respectively. Using this formula for $S_{lateral}$ and a maximum measured value of 1 V for $V_{lateral}$, the maximum lateral deflection was ~ 5 nm. $K_{lateral}$ was related to K_z as [109, 110]:

$$K_{lateral} = \frac{2L^2 K_z}{3(H + T/2)^2(1 + \nu)} \tag{3.3}$$

where ν is Poisson's ratio for silicon (0.27 for silicon <111> [111]). Equation 3.2 and Equation 3.3 were plugged into Equation 3.1, whiched yielded:

$$F_{lateral} = \frac{S_z K_z}{(1 + \nu)}\left(\frac{L}{H + T/2}\right)V_{lateral} \tag{3.4}$$

Each force-displacement curve derived in this manner was correlated with video frames (Figure 3.10).
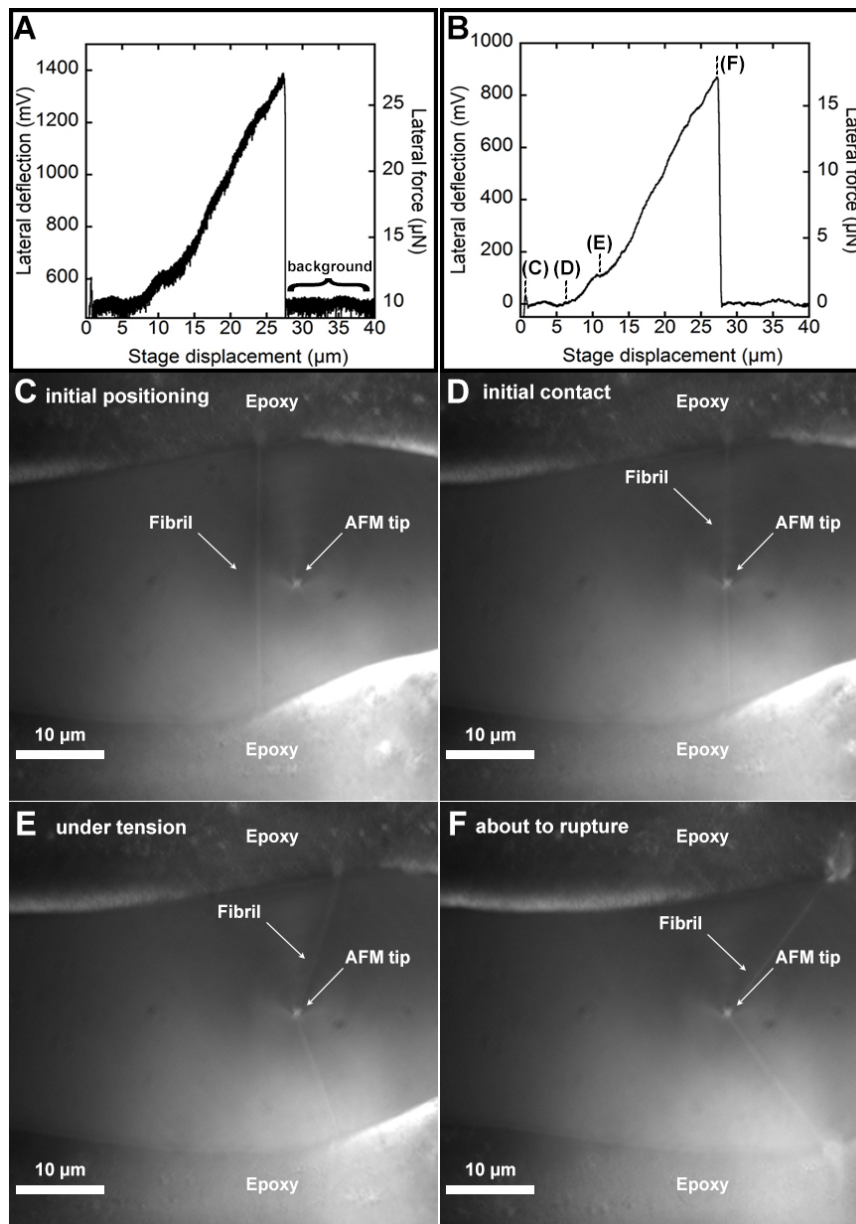
Figure 3.10: Representative CDET fibril force displacement curve correlated with brightfield images captured at 20 frame per second. A) Force displacement curve collected at 500 kHz. In the regime following fibril rupture, the average force value (labelled "background") was subtracted, removing the force background. B) Force displacement curve after adjacent averaging over 11 points to smooth the curve, and background subtraction. Four points along the force curve (C, D, E, F) were selected and verified with the brightfield video, captured at 20 frames per second. The four points correspond to initial positioning (C), initial contact with the fibril (D), moment at which fibril first fully detached from substrate (E), and the moment immediately prior to rupture (F).

34

During all tensile manipulations, the AFM stage was moved at a constant velocity, v, of 1 μm/s. The constant stage velocity induced a time dependent fibril strain, strain rate, and ratio of force at the AFM tip to fibril tension (Figure 3.11A, B). The time dependent strain and dependent strain rate were plotted (assuming isolated segment length of 55.9 $\pm$ 8.2 μm (measured average $\pm$ standard deviation)), showed as a solid black line and grey shading, respectively. (Figure 3.11C, D). With constant AFM stage speed, the fibril strain rate was variable within $\pm$ 0.5 %/s due to the variability in isolated segment length.
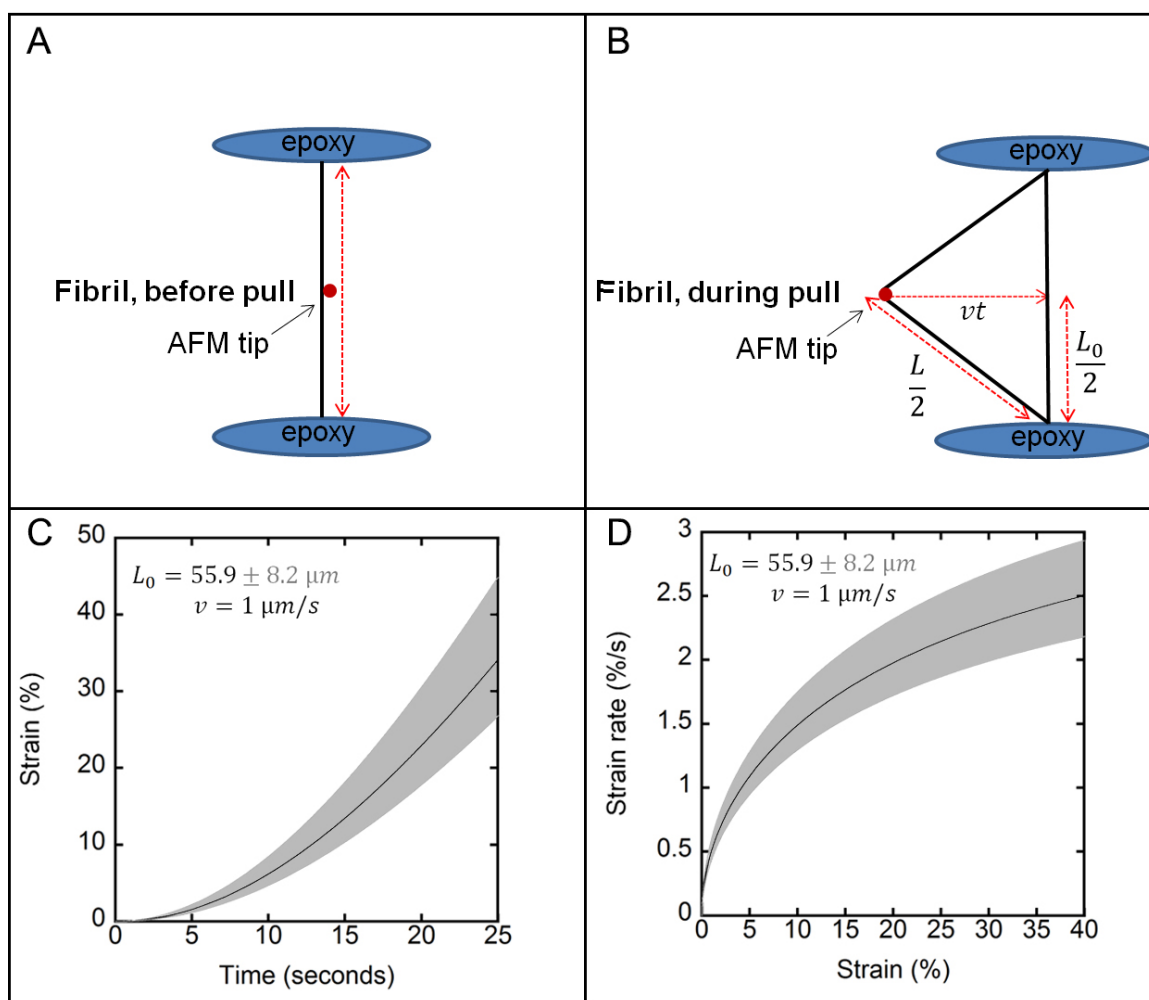
Figure 3.11: A) and B) Schematic relationship outlining the bowstring geometry used for tensile manipulations. C) Pythagoras' theorem was used to convert stage displacement into fibril strain according to Equation 3.5. D) Strain dependent strain rate, plotted according to Equation 3.6.

The time dependent fibril geometry was modelled as follows: the fibril length L was derived using the fibril's initial length L_o, and the stage displacement vt. Using Pythagoras' theorem, the time dependent strain of the fibril was given by:

$$\varepsilon = \frac{L - L_o}{L_o} = \sqrt{1 + 4(\frac{vt}{L_o})^2} - 1 \tag{3.5}$$

Taking a derivative of strain with respect to time, the strain rate during loading was given by:

$$\frac{d\varepsilon}{dt} = 4(\frac{v}{L_o})^2 t/(1 + \varepsilon) \tag{3.6}$$

The relationship between $F_{lateral}$ (which pointed in the direction of vt in Figure 3.11) and the fibril tension was given by:

$$Tension = F_{lateral}\frac{\sqrt{L_o^2 + 4(vt)^2}}{4vt} \tag{3.7}$$

which was converted to an engineering stress by dividing by the unloaded, de-hydrated cross-sectional area of each segment measured before manipulation (Figure 3.5):

$$\sigma = \frac{Tension}{CSA} \tag{3.8}$$

Each force-displacement curve was converted into a stress-strain curve according to Equations 3.5, 3.7, and 3.8 (Figure 3.12). The geometric approximation used in Equation 3.7 was not appropriate at very low pull times, because the fibril was not yet under tension, and because the factor of t in the denominator caused the tension to diverge for t close to 0. To approximate the stress-strain behavior this region of the curve, a (dashed) straight line starting from the origin was extended to the point at which the fibril was first fully detached from the substrate as seen in the captured video, which correlated with a knee in the force-displacement curve (Figure 3.12).

Four mechanical parameters were measured to describe each stress-strain curve: rupture strain, rupture stress, toughness, and high strain modulus. Rupture strain and rupture stress were measured from the last data point prior to the stress abruptly falling to zero. Toughness was the integral of the stress-strain curve, evaluated from 0% strain to the rupture strain value. The strain domain used to measure the high

strain modulus was the 5% of strain immediately prior to rupture, based on the location of the upturn in stress observed in SDFT fibrils.
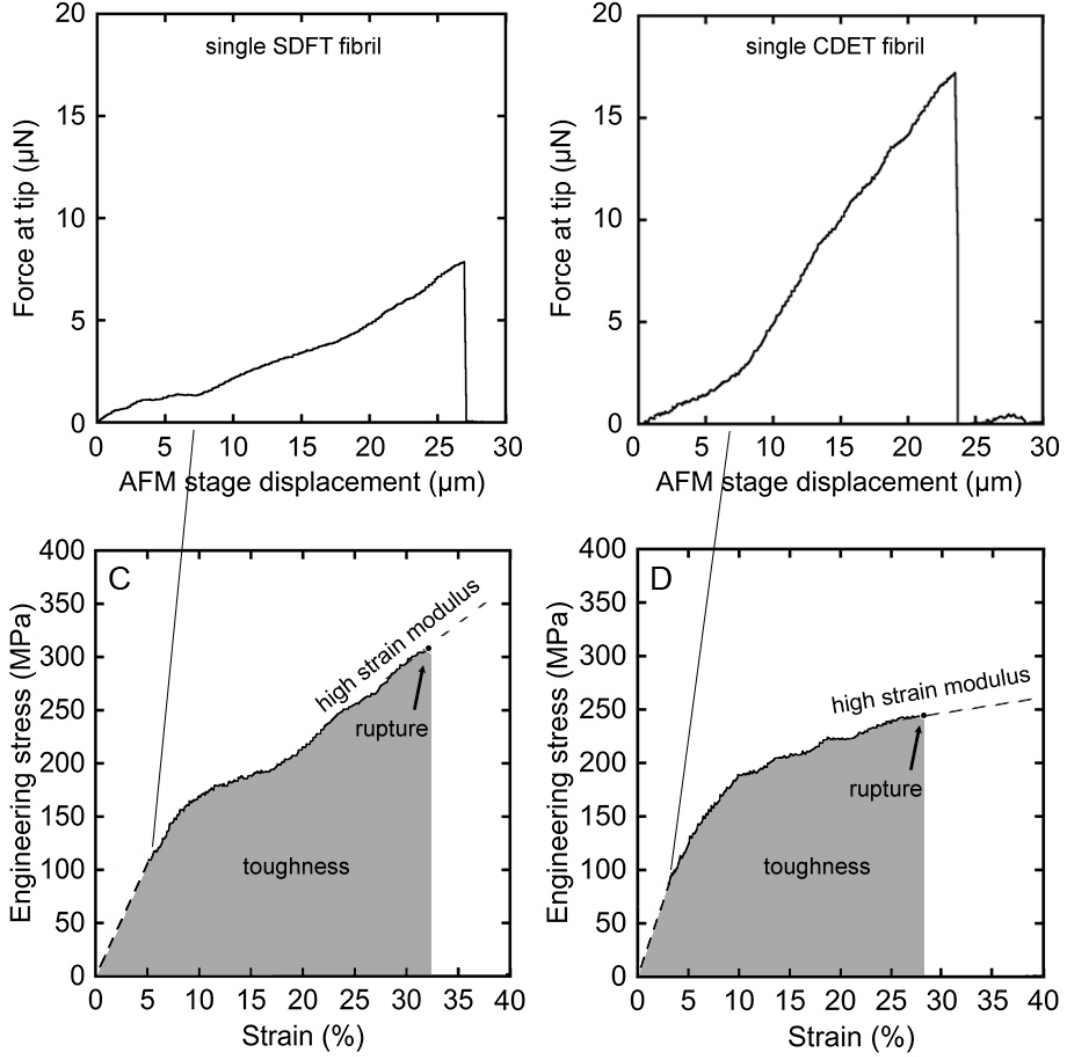
Figure 3.12: Representative conversion of a force-displacement curve (A, B) into a stress-strain curve (C, D) for one SDFT and one CDET fibril, respectively.

The geometry of the manipulation subjected the fibril to bending as well as tension, so the bending contribution to the measured force $F_{lateral}$ was estimated. According to Yang et $al.$ [80], who performed bending experiments on fibrils suspended across channels, the bending modulus of a single collagen fibril was 0.07-0.17 GPa. The bending modulus, E_{bend}, satified the relation [80]:

$$E_{bend} = \frac{l^3}{48\pi R^4} \frac{dF}{dz} \qquad (3.9)$$

The bending force dF required to displace a fibril (assuming $E_{bend} = 0.17$ GPa, radius $= 100$ nm and length $50 = \mu$m) by $dz = 5$ μm was calculated to be 0.1 nN. The magnitude of the bending contribution was therefore negligible compared to the μN force we measured at the AFM tip (Figure 3.12A and B).

3.9   Post-rupture dehydrated AFM imaging

After rupturing all fibrils on a given dish, it was removed from the AFM stage, rinsed three times using distilled, deionized water to remove any salt, dried under compressed nitrogen, and stored in a desiccating chamber. Brightfield images were used to determine the rupture location for each fibril: ruptures occurred at the AFM tip or glue attachment, and each fibril was sorted into one of these two categories. Dehydrated imaging was performed along each fibril following rupture, to characterize morphological changes. These images were typically between 30-40 μm wide, taken with a 0.125 Hz raster scan frequency. Other imaging parameters were kept the same before and after rupture.

The number of discrete sites of longitudinal damage was quantified for each fibril using dehydrated AFM images. For SDFT fibrils, these sites were sparse and were generally stand-alone events. For CDET fibrils, the longitudinal damage was more regular, which motivated the calculation of a linear plastic damage density, ρ [number of discrete damage sites/300 nm of fibril length], which was determined for each fibril by counting the discrete sites of damage, divided by the measured the length they spanned on the dehydrated AFM height image (Figure 3.13). The uncertainty on each length measurement of 0.1 μm was used to calculate the uncertainty on ρ via standard error propagation. If a CDET fibril had an undamaged piece in its midsubstance, like the one shown in Figure 3.13, then two separate ρ values were calculated, one on each side of the undamaged portion. An overall damage density was calculated for the whole ruptured segment by averaging these ρ values, weighted by the length over which they spanned.
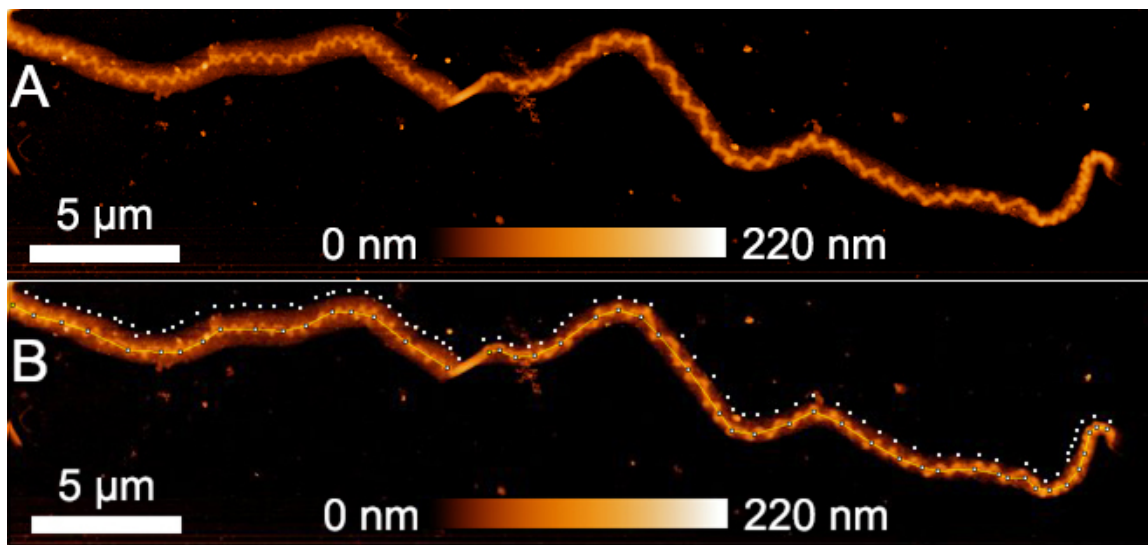
Figure 3.13: A) Dehydrated AFM height image of a ruptured CDET fibril. B) White dots mark every second damage site, and a yellow line along the fibril axis marks the measurement of fibril length. Two separate ρ values were calculated, one on each side of the undamaged micron of fibril in the middle. The weighted average ρ for the entire segment was 1.2 sites/300 nm.

To quantify the degree of structural disruption in the radial direction, the change in fibril height induced by rupture was calculated by subtracting the post-rupture fibril core height from the fibril height measured before rupture. One representative cross section, along with the peak heights of eight other cross sections taken across a single ruptured CDET fibril is shown (Figure 3.14). The standard deviation on the nine height measurements was 2 nm. Since the fibril core height had such little variability, one representative cross section was used per fibril in further analysis and the standard deviation of 2 nm was used as the uncertainty on the height measurements.
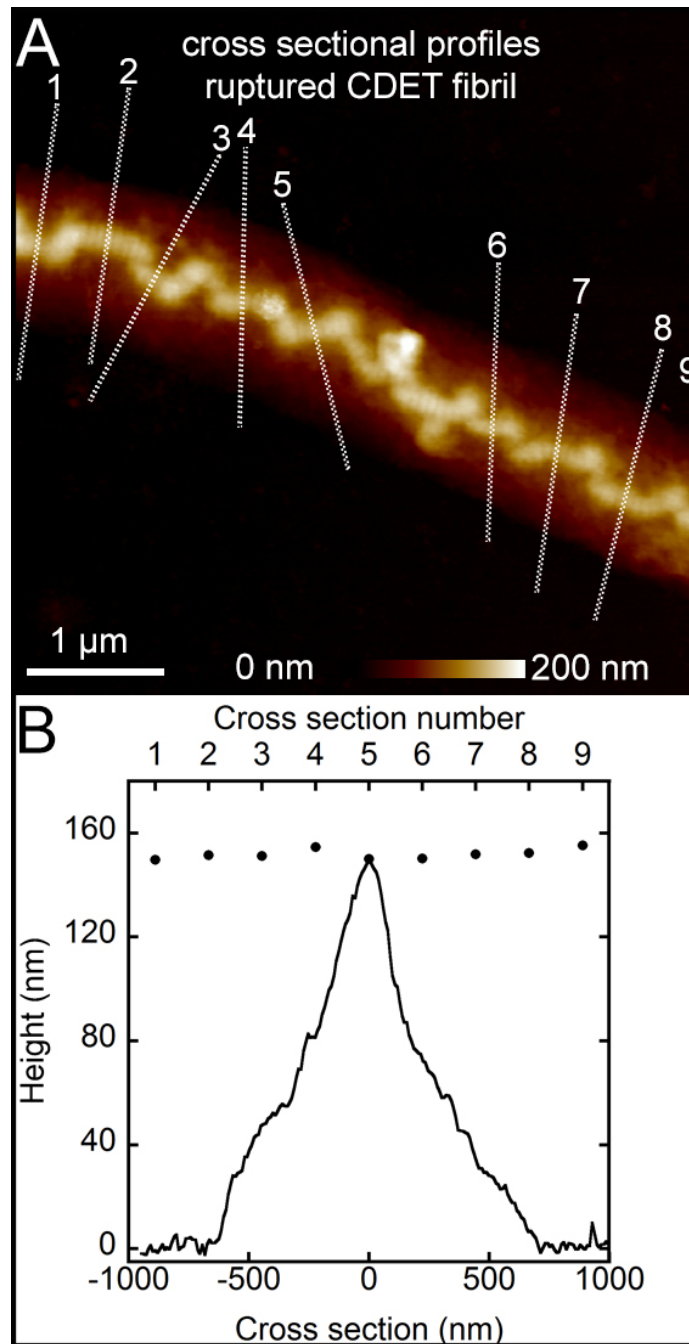
Figure 3.14: A) Post-rupture AFM height image for a representative single CDET fibril with nine cross sectional profiles. B) One select profile shown in full, along with the peak heights from each of the other eight profiles.

3.10 Post-rupture second harmonic generation imaging

The rupture-induced structure of 14 SDFT fibrils and 16 CDET fibrils were further explored through second harmonic generation imaging (SHG), performed by Stéphane Bancelin at the Institut National de la Recherche Scientifique in Varennes, Québec. Samples were probed with $\sim$ 150 fs linearly polarized laser pulses at 810 nm wavelength, generated with a titanium:sapphire oscillator [112]. The scattered SHG light at 405 nm wavelength was collected in the forward and backward directions with respect to the excitation, and was isolated using two FF01-720/SP-25 lowpass filters (Semrock, USA) which rejected the excitation light, and one FF01-405/10-25 bandpass filter (Semrock, USA), which selected the SHG wavelength and rejected the room light. Images were acquired point by point by scanning the focused excitation spot across the sample with a galvanic mirror (as described in [112]). A 40xW3/340 objective (Olympus, Japan) was used, yielding 400 nm spatial resolution. The pixel size was selected to be 200 nm, in order to oversample the sample structure and satisfy the Nyquist criteria [113]. For each ruptured fibril, the linear polarization of the excitation laser was rotated through (0°-180°] in 10° increments, yielding a pol-stack of 18 images. The maximum intensity value at each pixel, selected from amongst the 18 images in the pol-stack, was used to generated a single polarization-corrected maximum intensity map for each fibril. The field of view of the pol-stacks included both the ruptured segment and the unloaded comparison segment for each fibril, and an average value was measured for the ruptured and unruptured segment of each fibril. A ratio of ruptured/unruptured SHG signal was calculated for each fibril using these measurements. This analysis was performed for both forward and backward scattering.

3.11 Statistical analysis

Stress and strain distributions, sorted by factors Animal and Tendon Type, were analyzed for outliers. In each of the animals tested, one SDFT fibril demonstrated a rupture stress that was more than 1.5 interquarter ranges below the lower quarter mark, and were removed from any further analysis. Following removal of outliers, the distributions were analyzed for Normality with a Shapiro-Wilk test. If the distribution

was normal when grouped by Animal and Tendon Type, then a 2-way ANOVA with factors Animal and Tendon Type was performed on the data set. If the distribution was non-normal when grouped by Animal or Tendon Type, then a 2-way ANOVA was performed on a rank transformed data set with factors Animal and Tendon Type. This statistical treatment was applied to each of the following measurements:

Measurement	Values used in ANOVA
initial CSA	rank transformed
initial length	measured values
high strain modulus	measured values
rupture strain	rank transformed
rupture stress	rank transformed
toughness	measured values
total kinks	rank transformed
ruptured/unruptured height	rank transformed
ruptured/unruptured SHG (forward maximum)	rank transformed
ruptured/unruptured SHG (backward maximum)	rank transformed

Table 3.1: Values used for the 2-way ANOVA performed on each measurement. Non-normally distributed measurements were rank transformed prior to application of the 2-way ANOVA.

For measurements that were not significantly different by either Tendon Type or Animal, an average $\pm$ standard deviation by tendon type was presented. For measurements that had a significant difference by Tendon Type and did not have an interaction term, an average $\pm$ standard deviation by tendon type was presented, and the significant result from the 2-way ANOVA was used with no further post hoc testing. For measurements that had a significant interaction term in addition to having a significant difference by Tendon Type, an average $\pm$ standard deviation for each tendon type within each Animal was presented, and post hoc tests were performed. A Students t-test was used when comparing between normal distributions, and a Wilcoxon nonparametric test was used to compare between non-normal distributions. Statistical significance was denoted on each bar graph using the following notation: * p <0.05, ** p<0.01, *** p <0.001.

Chapter 4

Results

4.1 Overview

A total of 38 fibrils were ruptured and analyzed. 6 SDFT fibrils and 11 CDET fibrils were analyzed from Animal 1; 11 SDFT fibrils and 10 CDET fibrils were analyzed from Animal 2. All fibrils were extended by moving the AFM stage with a constant speed 1 μm/s. The results of the 2-way ANOVA performed on pre-manipulation measurements of initial cross-sectional area and initial segment length, with factors Animals and Tendon Type, are presented in Table 4.1:

Measurement	Tendon type P value	Animal P value	Interaction P value
Initial CSA	<0.0001	0.82	0.97
Initial segment length	0.88	0.98	0.41

Table 4.1: 2-way ANOVA results for pre-manipulation measurements. P values <0.05 were considered significant, and were highlighted.

SDFT fibrils were significantly smaller in cross-section than CDET fibrils, and there was not a significant difference in initial isolated segment lengths (Figure 4.1).
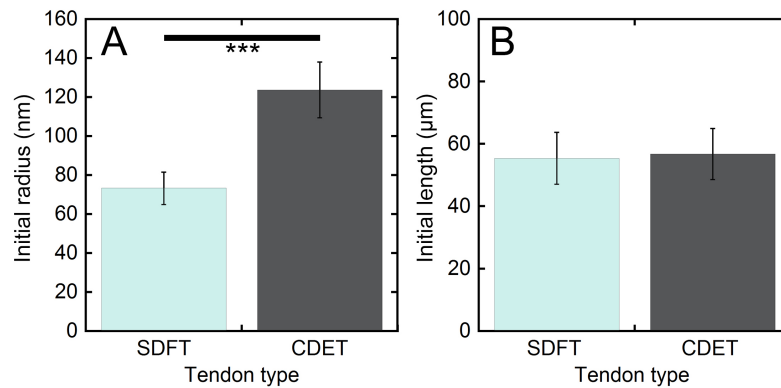
Figure 4.1: A) Initial (dehydrated) radius of fibrils, calculated using the cross-sectional area measurement and assuming a cylindrical fibril shape. B) Initial segments lengths were similar between tendon types.

Overall, fibrils tended to break near the AFM tip location or at the glue attachment (Table 4.2). SDFT fibrils most frequently broke close to the AFM tip location, while CDET fibrils most frequently broke at a glue attachment. This suggests that ruptures in both fibril types may have been induced prematurely by stress concentration, and that the parameters measured provide an underestimate of the changes that would occur in an ideal tensile testing geometry.

	Animal 1		Animal 2	
Rupture location	SDFT	CDET	SDFT	CDET
Glue attachment	0	10	3	7
Near AFM tip	6	0	8	2

Table 4.2: Fibril rupture location, by Animal and Tendon Type.

4.2 Rupture mechanics of single fibrils via AFM

The stress-strain curves, calculated using dehydrated cross-sectional area for each fibril, are shown organized by animal and tendon type in Figure 4.2. On the one hand, SDFT fibrils generally had a three-phase behavior. The initial increase in stress from 0-5% strain is an approximation because the fibril was being detached from the glass surface during this part of the stress-strain curve, and was not under pure tension. In the second phase, the modulus decreased between 5-10% strain, which lasted until ~15% strain. Above this strain, the stress increased more steeply, which continued until failure (Figure 4.2A, C). On the other hand, CDET fibrils generally only had a two-stage behavior. The first and second phases observed for SDFT fibrils were similarly observed on CDET fibrils; the important distinction was that CDET fibrils did not demonstrate the third phase of high strain stiffening, but rather appeared to undergo a graceful failure (Figure 4.2B, D).
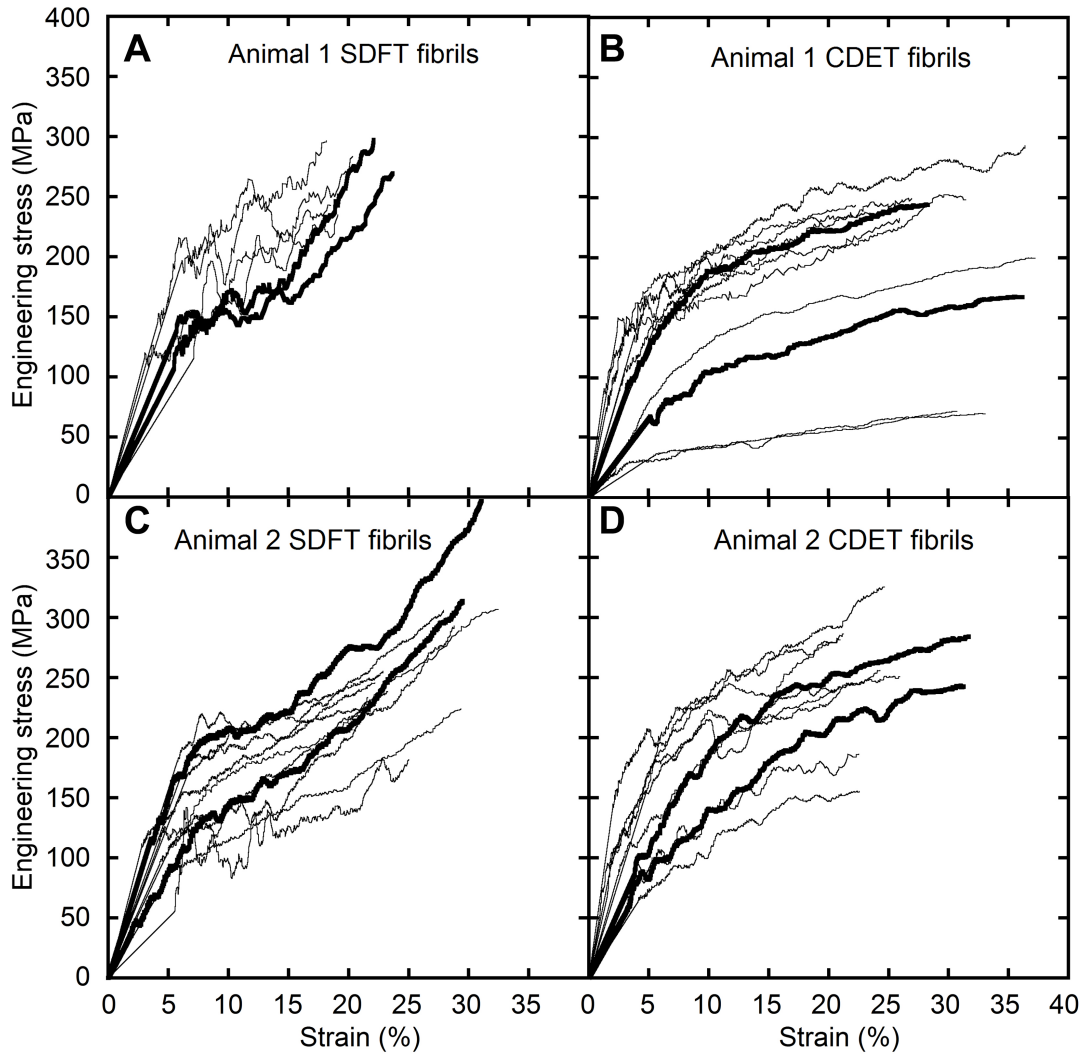
Figure 4.2: A, C) SDFT fibril stress-strain curves from Animal 1 and 2, respectively. B, D) CDET fibril stress-strain curves from Animal 1 and 2, respectively. Two stress-strain curves were bolded for each tendon type in each animal, which demonstrated the general trends most clearly.

The phases were difficult to separate quantitatively, and were left as a qualitative observation. For quantitative analysis on each stress-strain curve, the well-defined measurements of high strain modulus, rupture strain, rupture stress, and toughness were used. It should be noted that this methodology was not designed for low strain measurements, and as such a Young's modulus measurement would be less accurate than meaurements of high strain modulus, rupture strain, rupture stress, and toughness. The results of the 2-way ANOVA performed on these four mechanical measurements, with factors Animal and Tendon Type, are presented in Table 4.3:

Measurement	Tendon type P value	Animal P value	Interaction P value
High strain modulus	<0.0001	0.68	0.39
Rupture strain	0.002	0.32	0.0001
Rupture stress	0.07	0.40	0.22
Toughness	0.26	0.24	0.18

Table 4.3: 2-way ANOVA results for mechanical measurements. P values <0.05 were considered significant, and were highlighted.

The 2-way ANOVA showed that the high strain modulus was highly dependent on tendon type: The SDFT fibrils demonstrated a significantly larger high strain modulus than CDET fibrils (Figure 4.3A). The 2-way ANOVA showed that rupture strain was dependent on tendon type with a significant interaction, and so post hoc comparisons were performed within Animal and also within Tendon Type. Within Animal 1, the SDFT fibrils had a significantly lower rupture strain than the CDET fibrils, but this was not observed in Animal 2 (Figure 4.3B). Furthermore, Animal 1 SDFT fibrils had a significantly lower rupture strain than Animal 2 SDFT fibrils, while Animal 1 CDET fibrils had a significantly higher rupture strain than Animal 2 CDET fibrils (Figure 4.3B). While SDFT fibrils had a marginally higher average rupture stress and lower toughness than CDET fibrils (Figure 4.3C, D), neither of these differences were statistically significant (Table 4.3).
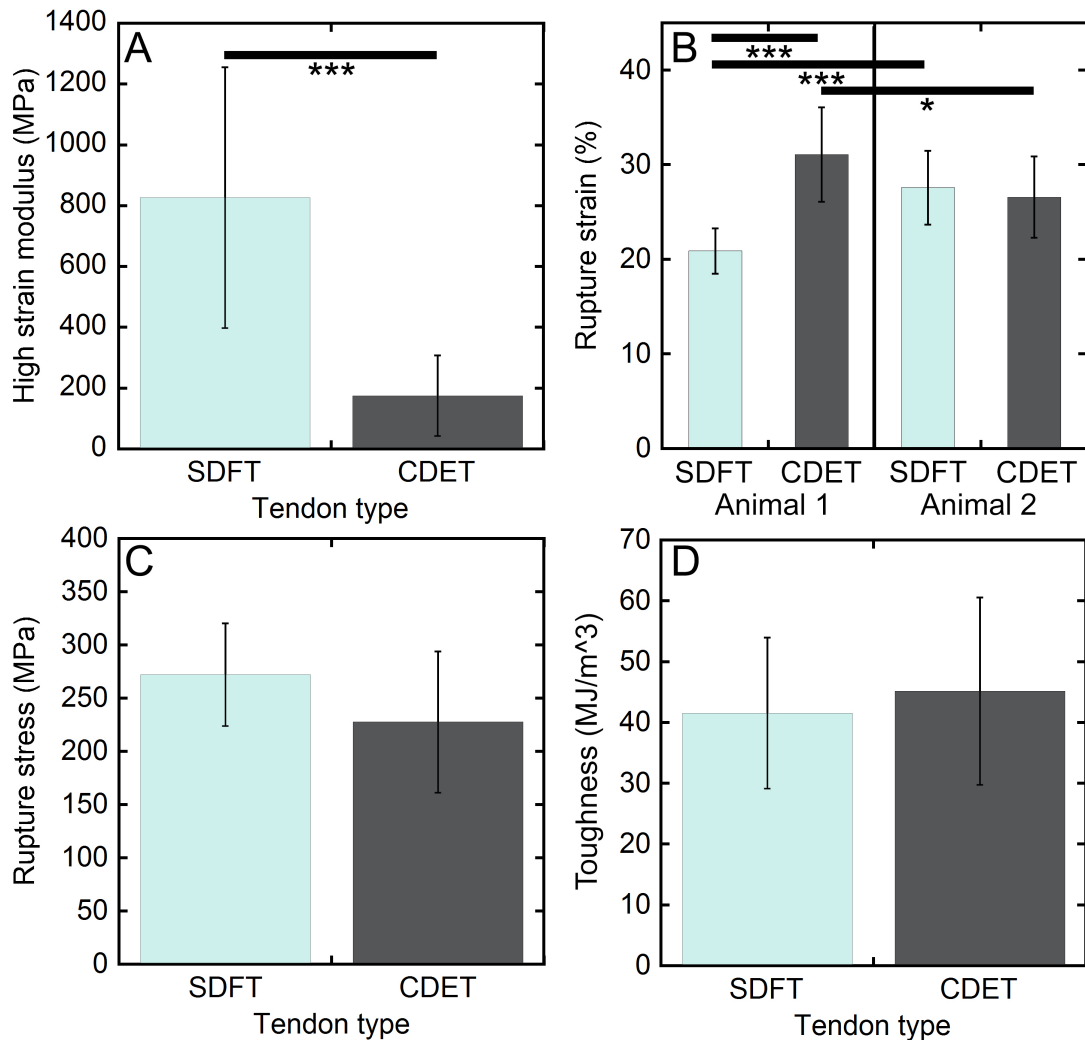
Figure 4.3: Summary of mechanical properties (mean ± SD) and statistical significance. A Student's t-test was used to compare the normally distributed rupture strains by tendon types within Animal 1, and a nonparametric Wilcoxon test was used otherwise.

4.3   Post-rupture single fibril morphology via AFM

After rupture, each fibril segment was dehydrated and imaged via AFM along its length, which was used to characterize longitudinal and radial damage. AFM height images of the damage incurred in the longitudinal midsubstance of CDET fibrils revealed a number of consistent damage motifs (Figure 4.4).

Figure 4.4: Ruptured CDET fibrils: dehydrated AFM images of midsubstance damage. A-F) Fibrils from Animal 1. G-L) Fibrils from Animal 2. White arrows denote slippage planes.

The least severe forms of damage presented as oblique lines of disrupted D-banding, which appeared in a repeating fashion spaced by regions of properly maintained D-banding (Figure 4.4C, G, H). This form of damage is referred to as "slippage plane", and was characteristic of 5 of the 21 CDET fibrils. The longitudinal fibril axis was relatively undisrupted by the presence of slippage planes ((Figure 4.4G, H), although they were sometimes accompanied by a small lateral shift ((Figure 4.4C). In the cases of more severely damaged CDET fibrils, the longitudinal axis of the fibril core took on a zig-zag morphology, and demonstrated disrupted D-banding at each change in axis direction ((Figure 4.4A, B, D-F, I-L). The term describing a singular damage structure of this form was a "kink" [68, 114], and was characteristic of 14 of the 21 CDET fibrils. The D-band was generally observable between successive axis changes (Figure 4.4A, B, D-F, I, J-L). In the radial direction, these fibrils appeared to separate into a distinct core and shell (Figure 4.4A, B, D-F, I, J-L), while shell delamination was absent on fibrils that only demonstrated slippage planes longitudinally.

Imaging each CDET fibril revealed three deviations in morphology from the motifs of longitudinal kinks and radially separated core/shell. Firstly, there were highly localized, $\sim 1\mu$m long regions of undisrupted fibril, termed "nodes", which occured on 11 CDET fibrils (Figure 4.5). In many cases, a node separated two regions of equally damaged fibril (Figure 4.5C, D, I). In other cases, the node separates regions that were not equally damaged, but is more severe on one side (Figure 4.5A, B, E, G). This could be due to some inherent structural differences or stress localization. Nodes occured in the middle of the ruptured segment only twice (Figure 4.5B, C), occured only 2.5 μm away from the ruptured end in one case (Figure 4.5F), and occured twice on one segment 4.5 μm away from each other (Figure 4.5E). Secondly, there were two instances of longitudinal splitting, in which the fibrils displayed subfibrillar elements (Figure 4.5A, H). The severity of splitting was more severe in Figure 4.5H, in which a 3 μm piece had been separated, than in Figure 4.5A, where the split was only 500 nm. Thirdly, among all fibrils tested, one demonstrated necking (Figure 4.5F).
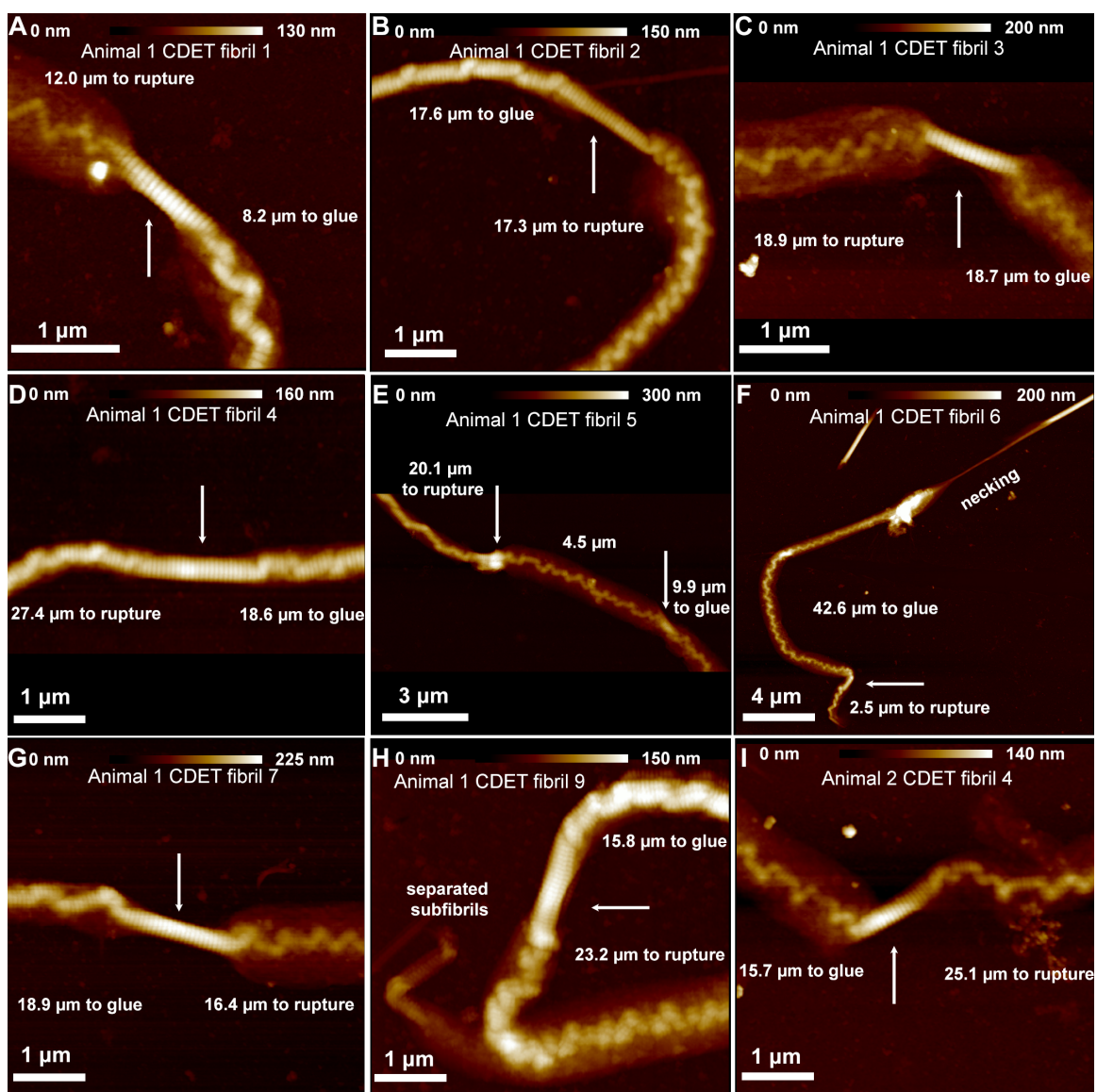
Figure 4.5: Ruptured CDET fibrils: dehydrated AFM images of isolated midsubstance features. A-H) Fibrils from Animal 1 I) Fibril from Animal 2. White arrows denote nodes.

AFM height images of the ruptured ends of CDET fibrils also revealed consistent damage motifs (Figure 4.6). The formation of kinks generally propagated all the way from glue to ruptured end (Figure 4.6A-I), and occured with separation of core/shell. In a few of these cases, the shell had been removed from a notably thinned core, which was nevertheless heavily kinked (Figure 4.6G, I). Several fibrils demonstrated an apparent increase in height towards the ruptured end (Figure 4.6B, D, H). In these locations, the recoil of the fibril post-rupture was presumably strong enough for

the fibril to turn over itself repeatedly over a short distance, giving the appearance of greater height. The pair of ruptured ends from one fibril were included (Figure 4.6K, L) for the stark difference in morphology between them. One end appeared structurally dissociated in a characteristic extensor fibril fashion, with the addition of shell-like material extending beyond the core of the ruptured end (Figure 4.6K). The other end appeared properly D-banded, with no shell material (Figure 4.6L). Notably, this was the only ruptured end with this morphology of all CDET fibrils. The most severe radial damage observed in the study was the complete dissociation into subfibrillar elements (beyond core and shell separation,) and was observed along $5\ \mu$m of one fibril length towards a ruptured end (Figure 4.6L). While the presence of salt crystals on that particular fibril complicated the interpretation of the AFM height information, the failure process seemed to have generated kinks that further dissociated into subfibrillar elements. This notion was based on the fact that the subfibrillar elements periodically bulged as a unit, reminiscent of the regular kinks observed on other fibrils.
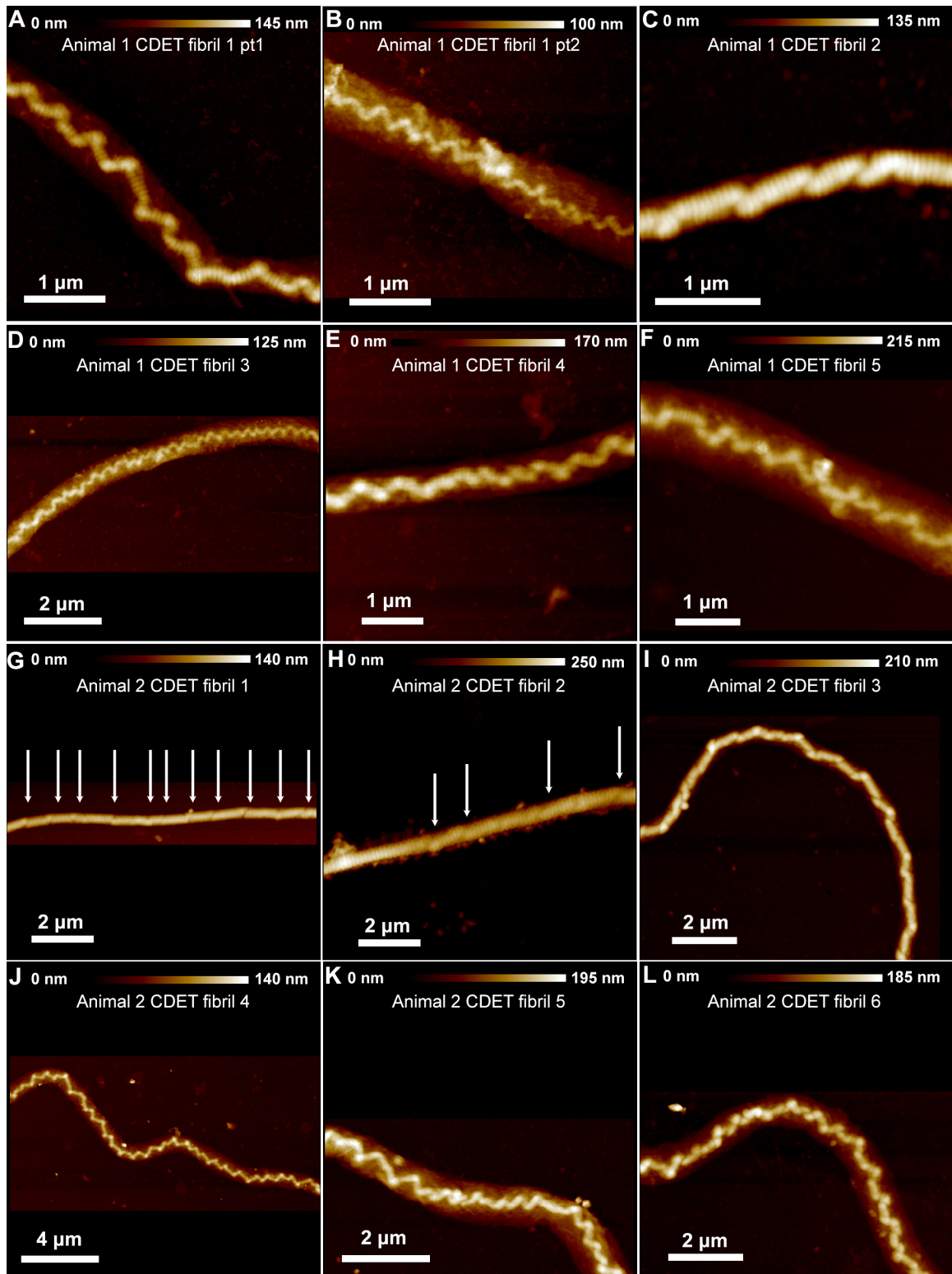
Figure 4.6: Ruptured CDET fibrils: dehydrated AFM images of ruptured ends. A-E) Fibrils from Animal 1. F-L) Fibrils from Animal 2.

AFM height images of the damage incurred in SDFT fibrils' midsubstance revealed much less structural disruption (Figure 4.7) than in the CDET fibrils. Generally, the D-band remained intact all along the length of SDFT fibrils (Figure 4.7A-L). In 9 of the 17 SDFT fibrils analyzed, no change in fibril structure was observed. The remaining 8 SDFT fibrils demonstrated damage in the form of slippage planes, which were less visibly stark than for CDET fibrils and the D-band was still largely intact. SDFT fibrils demonstrated isolated, sharp changes in fibril axis (Figure 4.7D, H, K, L). A slippage plane would be required for such a sharp geometrical configuration, so each of these features was counted as a single slippage plane. While longitudinal damage presented with modest regularly in one case (Figure 4.7I), stand alone events of damage were more commonly observed. SDFT fibrils did not separate into a distinct core and shell in the radial direction.

All SDFT fibrils ruptured cleanly, showing abrupt ruptured ends (Figure 4.8A-L). The ends flattened and widened modestly, but were otherwise indistinguishable from their midsubstance. In cases where the rupture spanned multiple D-bands, the banding pattern remained throughout the smaller end pieces (Figure 4.8D, F) which varied in length from two to seven D-bands. The peak force error image was shown in Figure 4.8F, which clearly showed the D-banding pattern of the smaller end piece. The most severe damage observed on SDFT fibrils occured in three cases, in which the 2 μm of fibril length leading to the ruptured end had regularly disrupted D-banding, and created a small shell layer at the end (Figure 4.8J-L). These cases had more pronounced damage regularity than most ruptured SDFT fibrils, but the damage notably only spanned a couple μm of fibril length in each case.
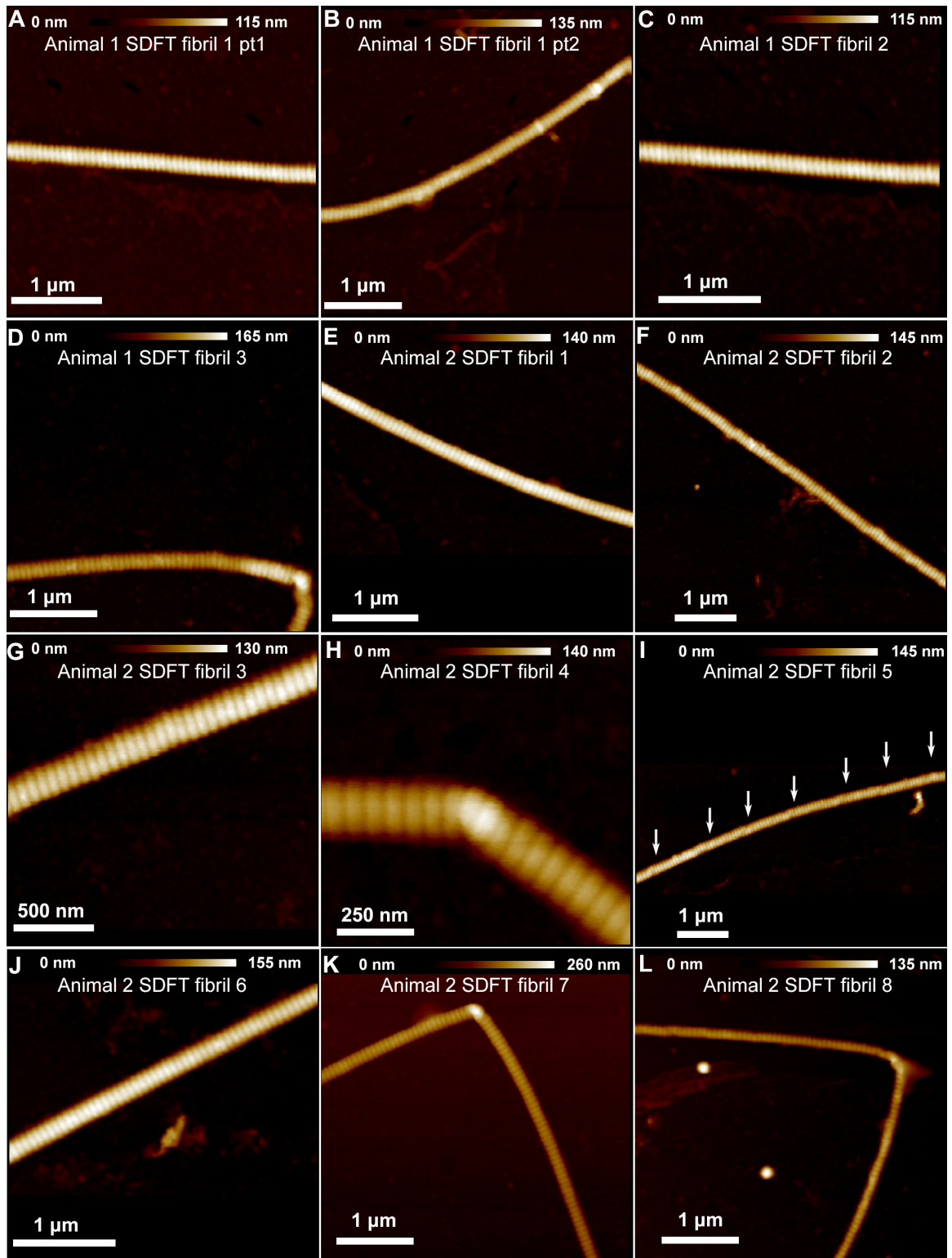
Figure 4.7: Ruptured SDFT fibrils: dehydrated AFM images of fibril midsubstance. A-D) SDFT fibrils from Animal 1. E-L) SDFT fibrils from Animal 2. White arrows denote slippage planes.
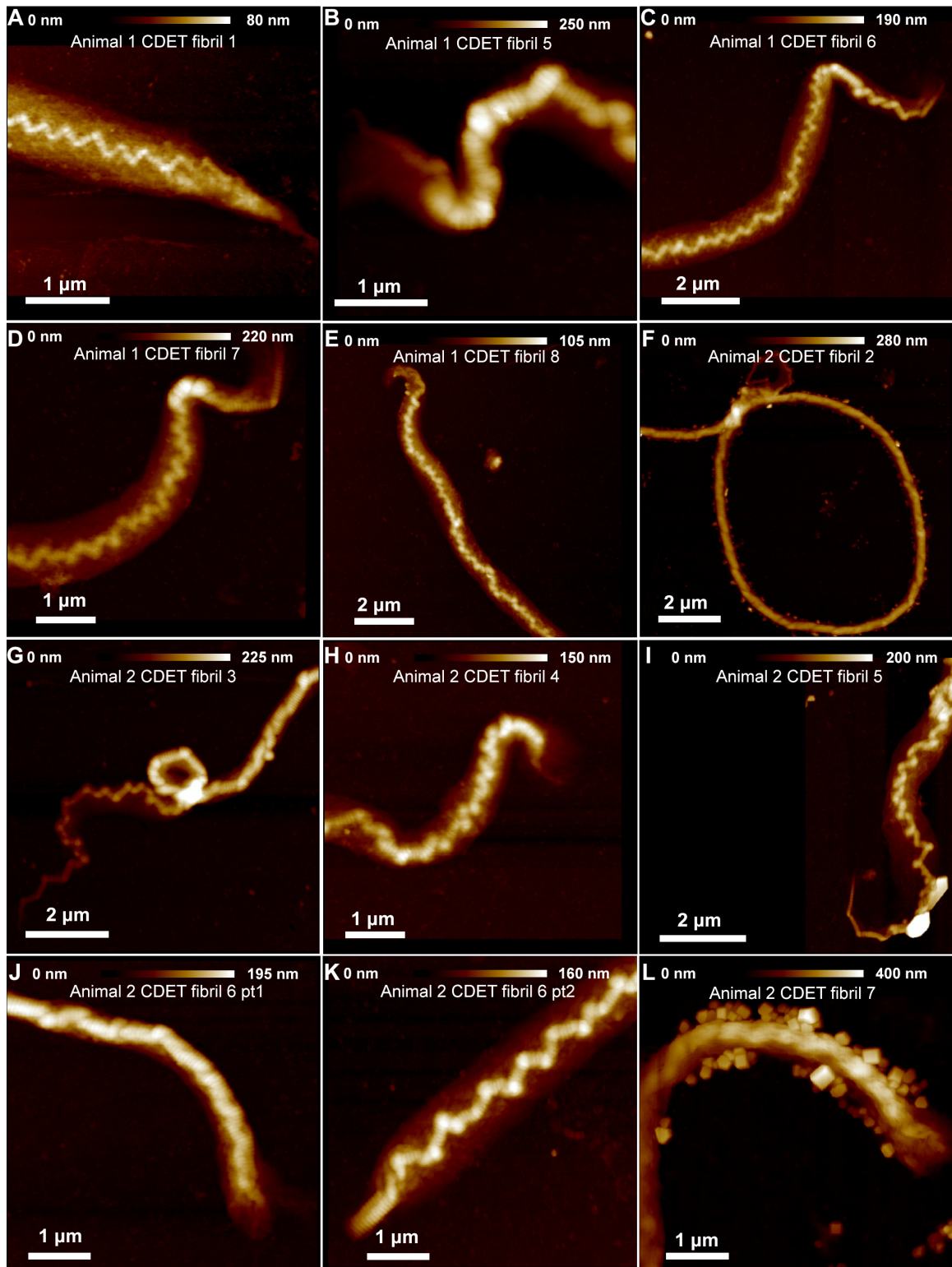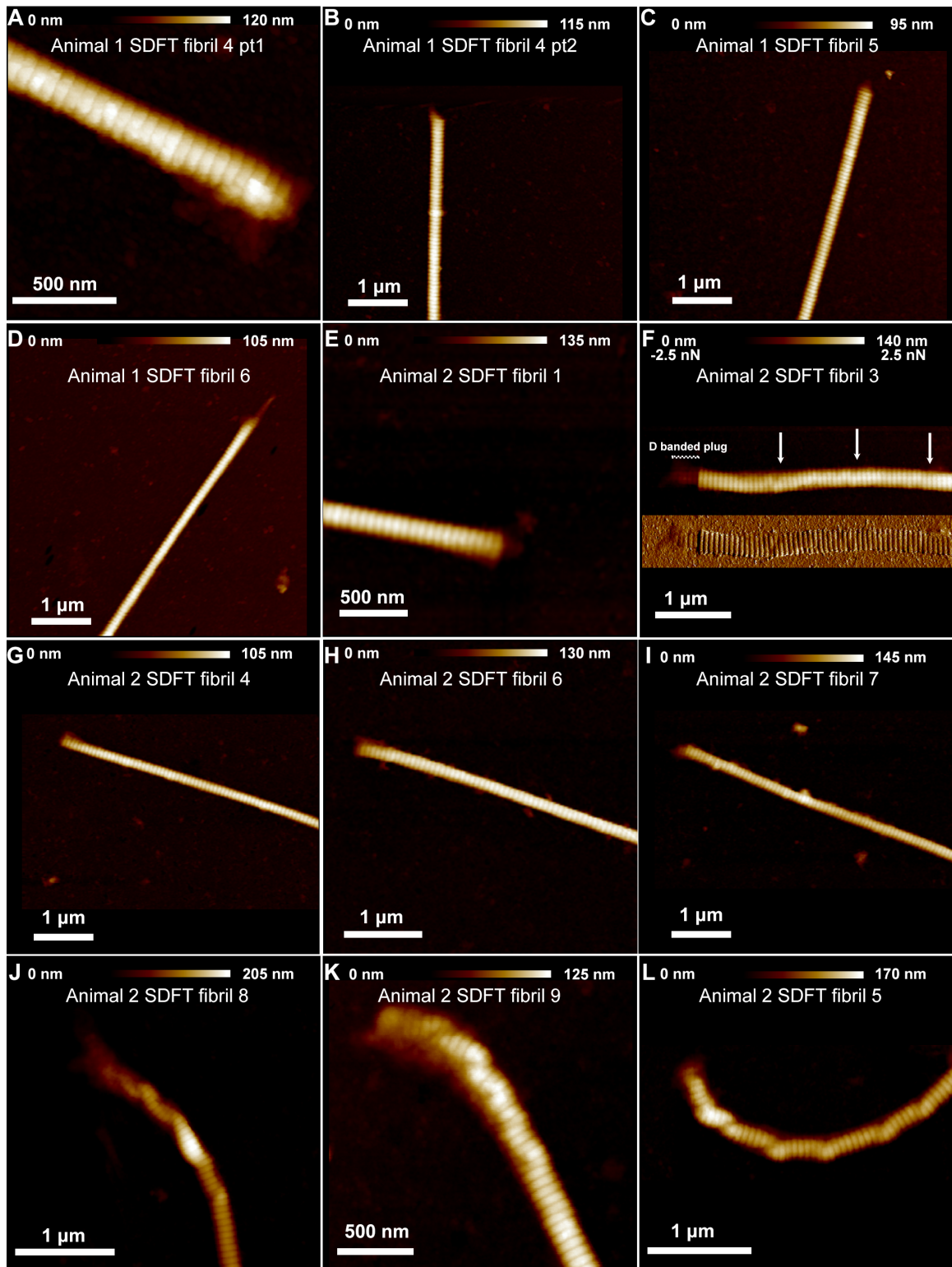
Figure 4.8: Ruptured SDFT fibrils: dehydrated AFM images of ruptured ends. A-D) SDFT fibrils from Animal 1. E-L) SDFT fibrils from Animal 2.

The visual impression given by the dehydrated AFM images of CDET and SDFT fibrils was clear: SDFT fibrils were much more resistant to permanent structural alteration than CDET fibrils, and demonstrated less longitudinal and radial damage. Longitudinally, CDET fibrils much more readily formed kinks with regular spacing, and the array of kinks spanned the length of the fibril. SDFT fibrils did not demonstrate the zig-zagging morphology characteristic of ruptured extensor fibril cores, but rather demonstrated isolated slippage planes. Radially, CDET fibrils separated into a distinct core and shell, while SDFT fibrils remained radially intact. To quantify these observations, the number of discrete plastic damage events and ratio of ruptured/unruptured fibril height were measured from dehydrated AFM height images. The results of the 2-way ANOVA performed on these two structural measurements, with factors Animal and Tendon Type, are presented in Table 4.4:

Measurement	Tendon type P value	Animal P value	Interaction P value
Ruptured/Unruptured fibril core height	<0.0001	0.0003	0.81
Number of discrete plastic damage sites	<0.0001	0.67	0.0001

Table 4.4: 2-way ANOVA results for post-rupture morphological measurements. P values <0.05 were considered significant, and were highlighted.

The 2-way ANOVA showed that SDFT fibrils had a significantly higher ruptured/unruptured fibril height ratio than CDET fibrils. Indeed, the average ratio for SDFT fibrils was not different than 1, while CDET fibrils had an average of ~ 0.7 (Figure 4.9A). This was consistent with the visual observation in AFM images that material was delaminated into a shell for CDET fibrils, but not SDFT fibrils.

The 2-way ANOVA also revealed that the number of plastic damage sites depended on Tendon Type, and that there was a significant interaction between factors. Post hoc tests revealed that the CDET fibrils had significantly more plastic damage sites than SDFT fibrils within each animal. CDET fibrils from Animal 1 had significantly more damage sites than CDET fibrils from Animal 2 (Figure 4.9B).
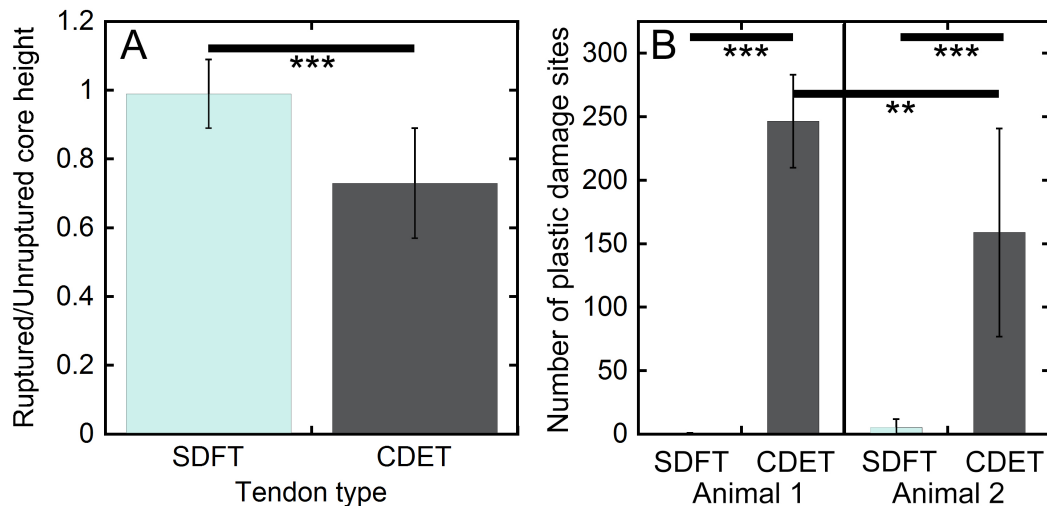
Figure 4.9: Morphological summary of radial and longitudinal damage (mean ± SD) with statistical significance by Tendon Type within Animal, and by Animal within Tendon Type. A Student's t-test was used to compare the normally distributed number of discrete damage sites by Animal within the CDET, and a nonparametric Wilcoxon test was used otherwise.

For CDET fibrils, the regularity of the longitudinal damage motivated the calculation of a plastic damage density, ρ [number of discrete damage sites/300 nm of fibril length]. Since the mechanical measurement of rupture strain and the morphological measurements of plastic damage sites and rupture/unruptured height ratio all depended on Animal for CDET fibrils, the rupture strain and ruptured/unruptured fibril height ratio were plotted as a function of the average ρ for each CDET fibril to elucidate a relationship between these mechanical and structural measurements (Figure 4.10).

The linear fit of rupture strain vs. ρ may provide meaningful coefficients (Figure 4.10A), with the caveat of potentially premature rupture due to stress concentration. The y-intercept of 21.8 ± 2.9% (estimate ± standard error, p <0.0001) matched the average rupture strain of 23.2 ± 3.9 % (mean ± SD) measured for undamaged SDFT fibrils. Therefore, this is a reasonable general value for a fibril's maximum extensibility in this pulling geometry, prior to the onset of plastic damage. The extra extensibility provided by structural alterations in CDET fibrils was quantified by the slope of rupture strain vs. ρ, which took a value of 7.1 ± 2.6%/(N/300 nm) (estimate ± standard error, p = 0.01). This value quantified how extension correlated with

densification of plastic damage. The linear fit of ruptured/unruptured fibril height vs. ρ may also yield meaningful coefficients (Figure 4.10B). The y-intercept of 1.0 $\pm$ 0.1 (estimate $\pm$ standard error, p <0.0001) predicts that a CDET fibril without longitudinal damage would also have no shell delamination. The amount of fibril material disrupted into a shell was quantified by the slope of the height ratio vs. ρ, which had a value of -0.25 $\pm$ 0.08%/(N/300 nm) (estimate $\pm$ standard error, p = 0.004).
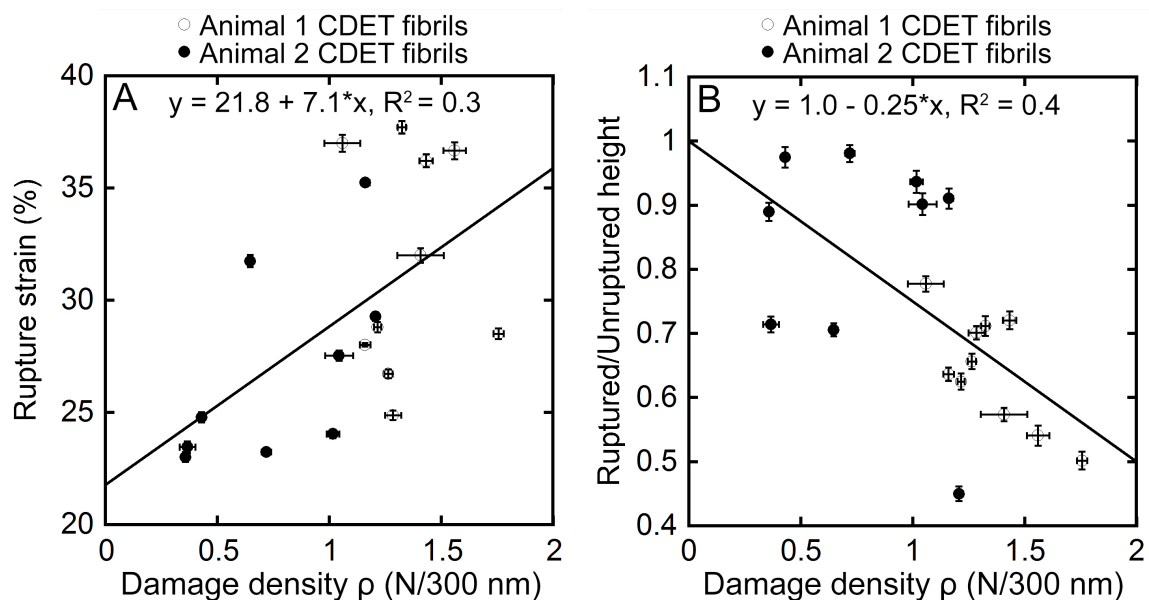
Figure 4.10: A) Rupture strain vs. ρ (N/300 nm) and B) ruptured/unruptured fibril height vs. ρ (N/300 nm) for CDET fibrils.

4.4   Post-rupture molecular order via SHG

After AFM imaging, 14 SDFT fibrils and 16 CDET fibrils were analyzed using second harmonic generation (SHG) microscopy, performed by Stéphane Bancelin at the Institut National de la Recherche Scientifique in Varennes, Québec. Forward and backward scattered SHG images were taken on a subset of ruptured fibrils, which included both the ruptured segment and an unloaded segment for comparison. On the one hand, the forward SHG signal on SDFT fibrils appeared similarly in the ruptured segment and the unloaded control segment (Figure 4.11B), and AFM images of the ruptured segment showed undisrupted D-banding pattern post-rupture (Figure

4.11C). On the other hand, the forward SHG signal on CDET fibrils appeared both less intense and less homogeneous on the ruptured segment than on the unloaded control piece (Figure 4.12B). Importantly, the CDET fibril shown had a node along its length (Figure 4.12C, zoomed view in Figure 4.5I) that distinctly appeared in the forward SHG image (Figure 4.12B). Nodes on CDET fibrils were resolved by SHG.
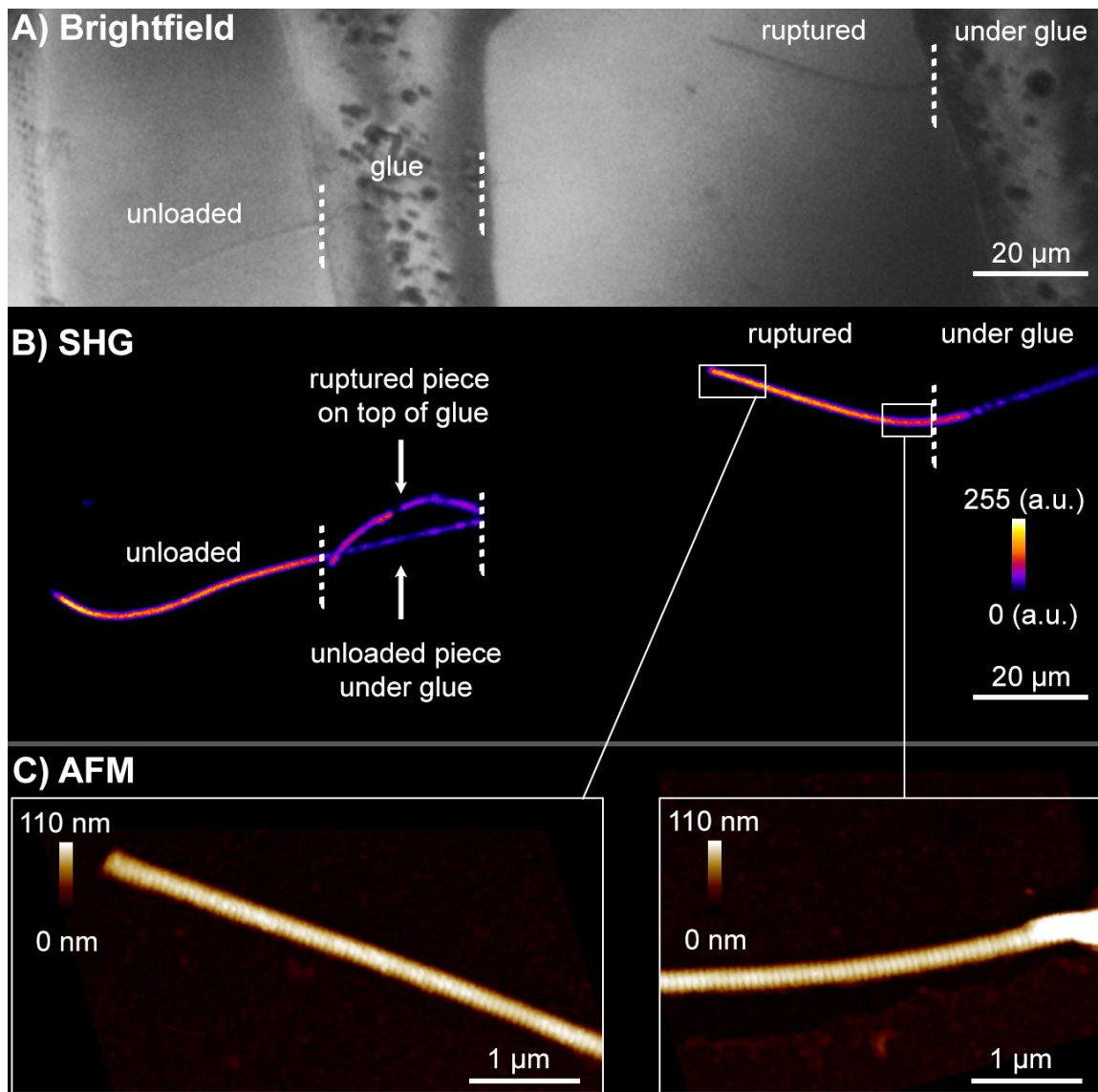
Figure 4.11: A) Brightfield image of a ruptured SDFT fibril, which shows the location of ruptured segment, glue strips, and unloaded segment. B) Polarization-corrected maximum forward SHG image of the same fibril, viewed with 256-valued false color palette. C) AFM images of the ruptured fibril segment, demonstrating undisrupted fibrillar structure.
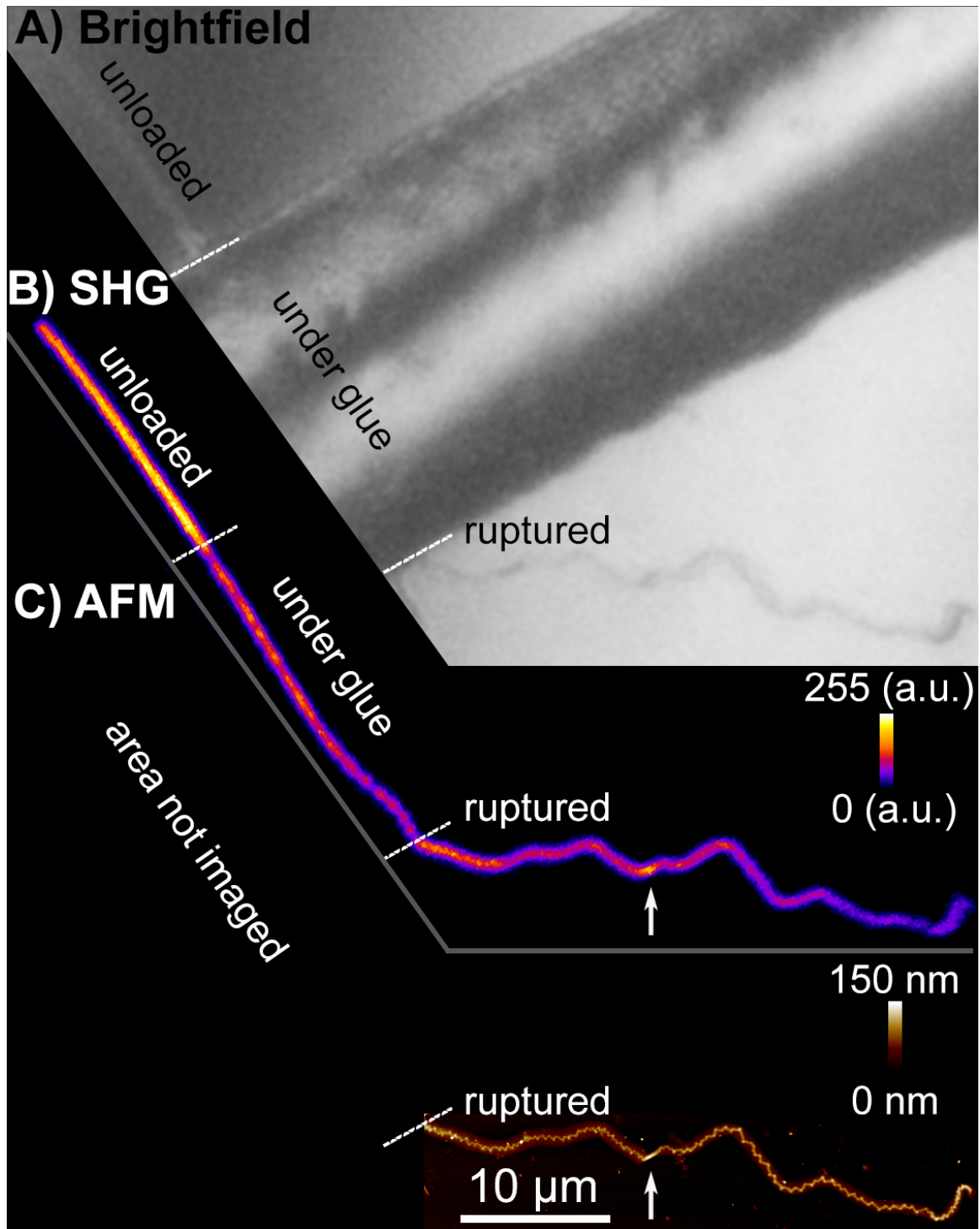
Figure 4.12: A) Brightfield image of a ruptured CDET fibril, which shows the location of ruptured segment, glue strips, and unloaded segment. B) Polarization-corrected maximum forward SHG image of the same fibril, mapped to 256-valued false color palette. C) AFM images of the ruptured fibril segment. The fibril had a single node, indicated by white arrows, which was resolved using both SHG and AFM.

Thermally-induced molecular disruption of collagen is known to cause a decrease in SHG intensity [101, 102, 103, 104]. Similarly, mechanically-induced molecular disruption can be quantified via SHG. A ratio of ruptured/unruptured SHG signal was calculated for each fibril by comparing the SHG intensity of the ruptured segment to that of the unloaded segment. The results of the 2-way ANOVA performed on these two SHG measurements, with factors Animal and Tendon Type, are presented in Table 4.5:

Measurement	Tendon type P value	Animal P value	Interaction P value
Ruptured/unruptured SHG (forward max)	<0.0001	0.20	0.87
Ruptured/unruptured SHG (backward max)	0.08	0.47	0.77

Table 4.5: 2-way ANOVA results for SHG measurements. P values <0.05 were considered significant, and were highlighted.

The 2-way ANOVA showed that the ruptured/unruptured forward SHG ratio strongly depended on Tendon Type, while the ruptured/unruptured backward SHG ratio did not depend on either factor (Table 4.5). The ruptured/unruptured forward SHG ratio was not different than 1 for SDFT fibrils, and was significantly higher than the ~0.7 ratio measured for CDET fibrils (Figure 4.13). Since forward SHG is sensitive to the whole fibril volume while backward SHG probes a volume smaller than the fibril [115, 112], the forward SHG is a more robust measurement for representing the molecular structure throughout the whole fibril.
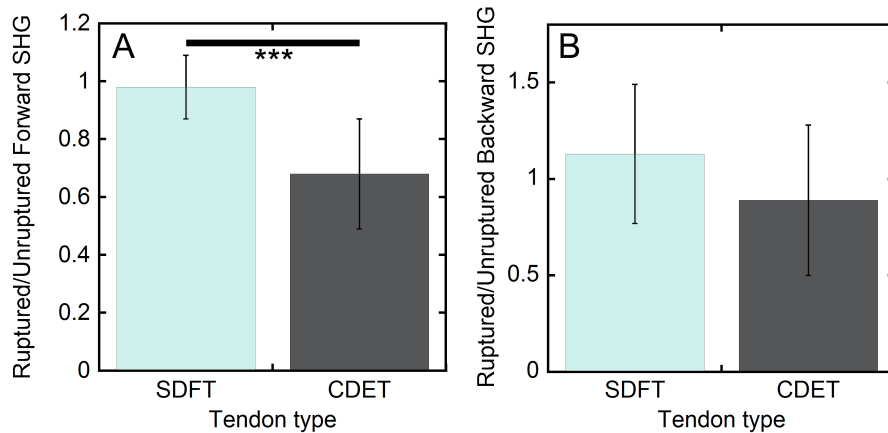
Figure 4.13: Ratio of ruptured/unruptured polarization-corrected maximum SHG in the A) forward and B) backward direction by tendon type, with statistical significance.

4.5 Results summary tables

The numerical values for each of the preceeding measurements is provided in the following tables. Table 4.6 contains values for measurements that did not have a significant interaction in the 2-way ANOVA, and Table 4.7 contains values for measurements with an interaction.

Measurement	SDFT	CDET
initial radius (nm)	73.3 ± 8.3	123.7 ± 14.3
initial length (μm)	55.4 ± 8.3	56.8 ± 8.2
high strain modulus (MPa)	826.9 ± 429.3	175.4 ± 132.6
rupture stress (MPa)	272.3 ± 48.3	227.7 ± 66.3
toughness (MJ/m^3)	41.6 ± 12.4	45.2 ± 15.4
Ruptured/Unruptured fibril core height	0.99 ± 0.1	0.73 ± 0.16
Ruptured/unruptured SHG (forward maximum)	0.98 ± 0.1	0.7 ± 0.2
Ruptured/unruptured SHG (backward maximum)	1.13 ± 0.36	0.89 ± 0.39

Table 4.6: Numerical values for each measurement that did not have a significant interaction in the 2-way ANOVA. Data is presented as mean $\pm$ standard deviation for each Tendon Type.

Measurement	Animal 1		Animal 2	
	SDFT	CDET	SDFT	CDET
rupture strain (%)	20.9 ± 2.4	31.1 ± 5.0	27.6 ± 3.9	26.6 ± 4.3
total plastic damage sites	0.3 ± 0.8	246.7 ± 36.6	5.5 ± 6.6	158.9 ± 82.0

Table 4.7: Numerical values for each measurement that did have a significant interaction in the 2-way ANOVA. Data is presented as mean $\pm$ standard deviation, organized by Animal and Tendon Type.

62

Chapter 5

Discussion

5.1 Comparison with previous single fibril investigations: tissue preparation and rupture methodology

There are two other methodologies that have been used recently to rupture single fibrils: vertically oriented AFM pulls [84] and MEMS based pulls [85]. The current work has strengths and drawbacks in comparision to these previous studies.

First, the decellularization process used in the current work is a methodological strength in comparison to previous fibril extraction methods, which include washing the tissue in trypsin [116], and risk digesting some of the tissue prior to fibril extraction. The decellularization facilitated the extraction of single fibrils from a SDFT, which were otherwise difficult to remove. I suspect that this difficulty was due to the dense interfibrillar meshwork observed in the SDFT [62] which may have been loosened and/or removed during decellularization, but this hypothesis has not been directly tested. In addition to facilitating the extraction of fibrils, the decellularization process sterilized the tissues, removing the need to ever freeze it. Following decellularization, tendons were stored in 1x PBS with antibacterial and antifungal agents at 4 °C without any sign of bacterial or fungal growth within the two weeks of storage time required to test $\sim$ 10 fibrils per tendon. Frozen tissue was used in both of the other comparable single fibril rupture studies [84, 85, 117].

A second strength is that a larger number of fibrils were ruptured in the current work (N=38) than the 25 fibrils ruptured via vertically oriented AFM pulls [84] or the 12 fibrils fractured via MEMS based pulling [85]. In vertical AFM force spectrsocopy, only one fibril can be glued and prepared at a time since the fibril is attached to the AFM probe [84]. Similarly, only one fibril can be prepared per MEMS device [85]. In the current work, we greatly increased fibril throughput, by having multiple experimental steps (gluing, hydrating, rupturing, and imaging) happen in batches of many fibrils on a single AFM dish (Figure 3.1). The experimental time per fibril was lowered, allowing a greater sample throughput than other methods.

Third, performing the tensile tests in a horizontal plane enabled visualization of the entire pulling process. Tensile tests are not visualized in vertical AFM force spectroscopy [84] or MEMS based pulling [85], which could be used to ensure the features in the measured force-distance curve are fibrillar in nature. The current work enabled recording a video of each tensile test, so features in the measured force-distance curves were checked against the video (Figure 3.10) to ensure that changes in the measured force were due to the fibril being under tension rather than other factors.

Performing the tensile tests in a bowstring geometry in the horizontal plane also had its drawbacks. The first drawback is that the calibration of the lateral force measurement in the current work is less direct than the force calibration in the AFM force spectroscopy [84] or the MEMS based method [85]. In the bowstring geometry employed here, the tensile force is calibrated by measuring the normal sensititivity S_z and spring constant K_z, and then scaling these measured quantities by geometrical considerations (Equation 3.2 and Equation 3.3). The normal and lateral properties are geometrically related when the cantilever is a rectangular prism [109, 110]. Since the Bruker Tap525A used are actually trapezoidal and not perfectly rectangular (Figure 3.6B), this detracts from the accuracy of our force measurement, but does not affect the precision. In vertical AFM force spectroscopy, only the normal sensitivity and spring constant need to be measured [84], so the calibration is more accurate than in the current method. The MEMS device is calibrated by measuring the voltage-displacement response of the device without a fibril in place relative to the stiffness of tether beams, which was calculated using large deformation finite element analysis [86].

The second drawback of the current work is that the bowstring geometry has spots of stress concentration at the AFM tip and glue attachments, as well as a non-linear strain-time relationship (Figure 3.11). While the effect of the non-linearity is likely small because it is only a change of $\sim 1\%/s$ of the whole pull, stress concentrations may have caused premature rupture in the fibrils tested (Table 4.2). The tendency of SDFT fibrils to break at the AFM tip location, while CDET fibrils failed at the glue attachment, may be due to the size difference between fibril types. Since SDFT fibrils are much smaller, it is possible they are more susceptible to slicing by the AFM tip.

64

The tendency of CDET fibrils to break at the glue attachment suggests that rupture may be premature for both SDFT and CDET fibrils. While premature rupture due to stress concentration is a drawback of the current work, geometrically induced stress concentrations also exist in vertical AFM force spectroscopy, where the fibril would be bent 90 ° at its bottom glue attachment point, and stress-concentration appears to have occured in the MEMS based uniaxial tensile testing [85]. Overall, stress concentration is a persistent challenge at the single fibril level, and appears to affect each methodology.

The third drawback of the current work is that the low strain data is unreliable, because it does not represent fibril tension but rather is due to the fibril being progressively detached from the glass substrate (Figure 3.10). Fourth, because the fibril is in close proximity to the glass throughout the whole pull, the stress values reported may be an over-estimate of the fibril stress. In contrast, both the vertical AFM pull and the MEMS method are substrate free [84, 85].

5.2 Rupture mechanics of single fibrils via AFM

5.2.1 SDFT and CDET fibrils have distinct stress-strain curves

The stress-strain behavior of SDFT and CDET fibrils pulled to rupture are markedly distinct. The most stark mechanical difference observed is that SDFT fibrils had a larger high strain modulus (826 MPa vs. 175 MPa, Figure 4.3A). This relationship is independent of animal tested, suggesting these are inherent properties of each respective fibril type. The SDFT fibrils had a higher rupture stress (272 MPa vs. 227 MPa, Figure 4.3C), though the p-value in that comparision was 0.07 and is not significant by the 0.05 standard. SDFT fibrils also generally appeared less extensible than CDET fibrils; however, the difference was only statistically significant within one of the animals tested (21 % vs. 31 % and 26% vs. 27%, Figure 4.3B). The clear cut difference in high strain modulus and modest difference in rupture stress together suggest that SDFT fibrils are more difficult to extend than CDET fibrils. The difference in rupture strain suggests that SDFT fibrils are less able to extend than CDET fibrils, though more animals would need to tested in order to solidify this statement.

5.2.2 Mechanistic paths to failure

The strong dependence of stress-strain behavior on tendon type (Figure 4.3) suggests that the mechanistic paths to failure are distinct for fibrils from the SDFT and CDET. Fibril extension mechanisms have been studied by performing X-ray diffraction (XRD) experiments on tendon under tension, which have suggested that the mechanisms of fibrillar extension are unwinding of the triple helical molecules followed by sliding between them [118, 119]. However, only $\sim 30\%$ of tendon level strain is transmitted to fibril strain [54]. High strain stiffening has been directly observed on single coiled-coil domains previously in tensile testing of individual myosin II tails [120]: after the protein was fully unfolded, the polypeptide backbone was directly engaged, and stiffening was observed as the backbone was stretched. The stiffening is entropic in nature, and comes from the sharp decrease in conformational microstates accessible to the polypeptide chain when it is almost fully extended. While high strain stiffening has not been directly observed on single collagen molecules, it is reasonable to assume that entropically driven stiffening of polypeptide chains would similarly occur in an unfolded and stretched collagen molecule. With this mechanism of high strain stiffening in mind, I propose that molecules in each fibril type were unfolded, and that the constituent polypeptide backbones were stretched in SDFT fibrils, while intermolecular sliding prevented further stretching of the polypeptide backbones in the CDET fibrils. The most likely structural explanation for the mechanistic difference is a distinction in intermolecular cross-links, which control load transmission between molecules [53, 121, 54, 51, 80, 42]. In a recent three-dimensional coarse-grained molecular dynamics (MD) study on the influence of enzymatic cross-links on fibril mechanics [122], three phases of mechanical behavior were observed. The stress-strain curves in the MD study showed: i) an initial elastic deformation corresponding to molecular stretching (uncoiling of the triple helix), ii) a region of decreased modulus corresponding to molecular sliding, and iii) high strain stiffening due to direct stretching of polypeptide backbones. The most important result of this molecular dynamics study is that only fibrils with a high density of mature cross-links showed the third phase of high strain stiffening [122]. The maturity of cross-links is important for homogeneous load sharing between molecules: mature, trivalent cross-links mechanically connect three molecules, while divalent cross-links only connect two molecules.

In addition to the maturity of cross-links, the cross-link density is important: if all cross-links were trivalent, but were sparse, then the cross-links may not be sufficient to prevent molecular slippage despite their trivalent nature. Therefore it makes sense that both cross-linking type and density tuned properties of fibrils in MD simulation.

While I did not investigate cross-linking directly, the SDFT have shown a distinct cross-linking profile in comparison to the CDET in the bovine and equine models. In the bovine model, the SDFT demonstrates both significantly more cross-links, and a significantly higher proportion of thermally stable cross-links than the bovine CDET [62], and in the equine model, the SDFT has a significantly higher content of the mature cross-link hydroxylysyl pyridinoline (HP) than the CDET [58]. I propose that the level of cross-linking in SDFT fibrils surpassed a threshold of intermolecular connectivity, enabling the applied load to be shared homogeneously across molecules within the fibril cross-section, which the CDET fibrils did not surpass. On the one hand, SDFT fibrils underwent a well mediated path to failure, in which fibrils went through the initial phases of molecular unwinding and some amount of intermolecular sliding until sliding between neighboring molecules was hindered via engagement of a high density of mature cross-links, which lead to high strain stiffening as the constituent polypeptide backbones were subsequently stretched. On the other hand, CDET fibrils underwent a poorly mediated path to failure, in which the fibrils went through the initial phases of molecular unwinding, which was followed by intermolecular sliding. When engaged, the cross-linking profile was insufficient to prevent further sliding between molecules, which continued as the predominant mechanism of extension until failure.

5.2.3 Comparison of mechanical data with previous results

Interestingly, a similar dichotomy in stress-strain behavior as the one observed between SDFT and CDET fibrils (Figure 4.2) was also observed by Svensson *et al.* [84] between 33-39 year-old human patellar tendon (HPT) fibrils and 12-16 week-old rat tail tendon (RTT) fibrils. HPT fibrils demonstrated a larger rupture stress than RTT fibrils (540 MPa vs. 250 MPa), and exhibited high strain stiffening while RTT fibrils did not (high strain modulus 4.3 GPa vs. 1.6 GPa). However, the HPT and RTT demonstrated similar rupture strains (20 % vs. 17 %) [84]. While a similar dichotomy

in high strain stiffening between fibril types was observed in our work and Svensson's, there was a quantitative distinction between the two works [84]: the high strain modulus measured was systematically lower, and the rupture strains systematically higher, in the current work than in the work of Svensson [84]. One likely explanation is the large difference in strain rate between the current work and that of Svensson *et al.* [84]. Fibrils are known to have viscoelastic properties [88, 42, 82, 81, 83], and fibrils in the current work were ruptured using a strain rate of $\sim 1\%$/s, which is two orders of magnitude lower than the $\sim 100\%$/s used by Svensson [84]. Another factor that may have contributed to the quantitative discrepancy between the current work and that of Svensson *et al.* is one of their analysis steps: each strain measurement was multiplied by a constant factor of 0.55 (and each modulus measurement divided by 0.55), which scaled their low strain modulus measurements to match measurements made on longer fibrils in their previous work [84]. Their modulus measurements were more similar to ours prior to applying this correction factor. The stress values in the current work and that of Svensson *et al.* [84] were based on dehydrated fibril cross-sectional area, and AFM investigation of fibril swelling has shown a diameter increase of 70-100 % between dehydrated and hydrated states [123, 82, 114].

While there is some quantitative discrepancy between the current work and that of Svensson *et al.* [84], the differences appear to be largely systematic in nature. Overall, the fact that a dichotomy is stress-strain behavior was observed in the current work and by Svensson is the most informative comparision. Interestingly, when Svensson *et al.* measured the cross-linking profile of the HPT and RTT fibrils, they found that the HPT fibrils had significantly higher quantities of the mature cross-links hydroxylysyl pyridinoline and lysyl pyridinoline than the RTT fibrils [84], which mirrors the difference that has been observed in the bovine SDFT and CDET [58]. If the HPT is considered an energy storing tendon (a fact that I was not able to confirm from the literature) and the RTT considered a positional tendon, then both the current work and that of Svensson independently show that energy storing tendon fibrils demonstrate high strain stiffening, while positional tendon fibrils undergo a graceful failure.

In addition to comparison with Svensson [84], the mechanical properties of the bovine SDFT and CDET fibrils should be compared to failure properties of isolated

68

rat patellar tendon (RPT) fibrils (unreported age) using MEMS based devices by Liu *et al.* [85]. A large discrepancy exists between the maximum strain measurements: while bovine SDFT and CDET fibrils demonstrated average rupture strains between 20-30% (Figure 4.2), the rat patellar tendon fibrils had an average maximum strain over 60 %. There was also a discrepancy in the maximum stress measurement: RPT fibrils had an average maximum stress of $\sim$70 MPa, much lower than the 250 MPa required to rupture bovine SDFT and CDET fibrils. It is worth noting that Liu *et al.* applied a multiplicative factor of 4.85 to their cross-sectional area measurements (performed *in vacuo* via SEM), based on the swelling factor previously observed between cross-sectional area measurements via SEM and hydrated AFM [89]; therefore the maximum stress measurements were much closer to the bovine SDFT and CDET values prior to applying this correction factor. However, another explanation is needed for the large discrepancy in maximum strain, which may be structural in nature: Liu *et al.* [85] noted that the fibrils tested did not separate totally into two pieces, and were still connected by a collagenous bridge of material. It is difficult to see the bridging material in the SEM images provided, but localized thinning and structural disruption are characteristic traits of material necking, which is evidence of localized flow. Necking may explain the large maximum strains observed by Liu *et al.* [85]. None of the RPT fibrils demonstrated mechanical evidence of high strain stiffening, but rather had a graceful failure qualitatively similar to the bovine CDET. I propose that the graceful failure behavior was controlled by the necking, which make their stress-strain curves difficult to compare to directly, and speaks to difficulties in measuring stress-strain curves at the single fibril level.

5.3 Post-rupture single fibril morphology via AFM

5.3.1 SDFT and CDET fibrils have distinct post-rupture morphologies

SDFT and CDET fibrils demonstrated remarkably different tendencies for plastic deformation in response to rupture. SDFT fibrils underwent significantly less structural disruption in both the longitudinal and radial directions: SDFT fibrils had generally intact D-banding post-rupture, demonstrating isolated events of plastic damage in the form of slippage planes, and did not delaminate material radially into a disordered

69

shell (Figure 4.7). The fact that the D-band was clearly visible after rupture and dehydration suggests that the axial registry of collagen molecules had been largely maintained as collagen helices unfolded during stretching. The ruptured ends of SDFT fibrils were much cleaner than in CDET fibrils, giving a brittle-like appearance (Figure 4.8). Since the bovine SDFT is known to have a higher density of thermally stable cross-links than the CDET [62] and the equine SDFT has more mature cross-links than the CDET [58], I propose that the cross-linking in bovine SDFT tendon fibrils controls the morphological characteristics observed post-rupture in the current work: the intermolecular connectivity was sufficient for homogeneous load-sharing across molecules within the fibril cross-section, and irrecoverable molecular sliding was hindered at high strain by the network of cross-links. It is likely that cross-links maintained the quarter stagger molecular registry during the rupture process even as molecules were unfolded and stretched, evidenced by the D-banded fibrils post-rupture (Figure 4.7). The slippage plane damage sites observed on SDFT fibrils were locations at which sufficient sliding occured to disrupt the registry, but generally occured infrequently and with less severity than in CDET fibrils (Figure 4.4). The mechanistic differences and post-rupture morphological differences between SDFT and CDET fibrils both suggest an underlying difference in intermolecular connectivity, and the hypothesis that distinct cross-linking is at the root is consistent with the known differences in chemical composition [58] and functionality of cross-linking [62] between the SDFT and CDET. While MD simulations [122] have recapitulated the experimental stress-strain behaviors of fibrils with different cross-linking to some degree, the characteristic motifs of post-rupture morphology observed experimentally have not been predicted by any simulation. This suggests further nuance in the structure-function relationship that is not yet fully understood.

5.3.2 CDET fibrils: longitudinal and radial damage

Kink density and extensibility

One question that the current work was particularly well suited to address was the interplay of kink formation and fibril extensibility: rupture strain correlated significantly with kink density (Figure 4.10), suggesting that each discrete kink site provided some extra extensibility to the fibril. This is consistent with the mechanistic

path to failure I suggested for CDET fibrils: insufficient intermolecular cross-linking was unable to prevent irreversible molecular slippage, which continued until failure. Discrete locations of irreversible molecular slippage each provided the fibril with a bit of extensibility, and resulted in a slippage plane or kink post-rupture. The direct investigation of the structure-function relationship between rupture strain and kink formation is one of the most important contributions of the current work to the body of knowledge regarding localized fibril damage. This importantly has predictive power, as the number of kinks required to provide a CDET with a given extensibility can be predicted from the linear regression of rupture strain vs. kink density (Figure 4.10).

Shell delamination

Delamination of a shell was a major structural motif of CDET fibrils post-rupture (Figure 4.9A), and the shell morphology contained clues as to how it was formed. First, the molecular quarter stagger was evidently lost, as the D-banding pattern was not present post-rupture. However, it should be noted that the shell still followed the average contour of the fibril core (Figure 4.4), which suggests the molecules are still laterally connected by cross-links, even as the quarter stagger was disrupted. In other words, the rupture process caused irrecoverable sliding, but did not destroy the cross-links, so the molecules were still laterally connected post-rupture.

While it is clear that the shell was more structurally disrupted than the core, it is not clear how distinct the core and the shell were prior to rupture. A number of investigations have suggested an inherent radial distinction: a tubelike fibrillar cross-section has been suggested by AFM imaging on fibrils, which showed sharp bends [75], and by thermal denaturation, which showed molecules in the center of fibrils are easier to denature than molecules toward the outer fibril shell, suggesting lower molecular density in the center [124].

The tubelike fibril model is also supported by equatorial XRD experiments. XRD patterns from rat tail tendon [125], chicken and turkey leg tendon, and bovine achilles tendon [126] all demonstrated a set of sharp Bragg reflections superimposed on an underlying diffuse scatter, which Hulmes *et al.* [127] recapitulated using a theoretical model in which both molecular density and packing order increase with radial position

[127]. The less ordered inner core contributed the diffuse signal, while the highly ordered outer shell contributes the sharp Bragg peaks.

With the tubelike fibril model in mind, I propose that when CDET fibrils were pulled to rupture, the radial gradient in molecular density concentrated stress to the outer shell of the fibril, and that the cross-linking was insufficient to prevent irrecoverable sliding between molecules. Thus, the stress concentration caused a strain concentration, disrupting the quarter stagger registry and causing the apparent shell. The effects of shear may also play a role in shell formation, though it is difficult to parse these effects out. For instance, it is also possible that the molecules in the more loosely packed fibril core had larger lubricating water jackets than the molecules in the outer fibril shell, and that the formation of shell was influenced by intermolecular shear. It is also possible that the shear between the fibril and the glass influenced the formation of the shell. However, a delaminated shell was also formed on RTT fibrils ruptured using vertical AFM force spectroscopy, which is substrate free during tensile testing [84], so shear between the fibril and the glass during manipulation is not a consistent explanation for shell delamination. Rather, I propose that it is an inherent process of positional tendon fibrils. In a recent study of plastic damage incurred on fibrils extracted from a bovine tail tendon overloaded *in situ* [114], two ideas were put forth to explain the formation of shell: forces acting directly on the surface of fibrils, and a pre-existing radial heterogeneity which predisposed the outer fibril radius to damage. The current *ex vivo* single fibril results suggests that shear between the fibril and the glass surface is not the dominating factor in shell formation, and that an inherent radial heterogeneity is the most likely cause.

How are longitudinal and radial damage related?

The current investigation demonstrated that fibrils with greater kink density had more shell delamination (Figure 4.10), showing that the radial and longitudinal damage are related. However, it is difficult to tie the mechanisms together and a firm conclusion cannot be drawn from the results at hand. Nevertheless, the interplay of rupture strain, kink formation, and shell delamination on CDET fibrils between animals was informative: since Animal 2 had a lower rupture strain, less kinks, and less shell delamination (Figure 4.10), it is possible that the CDET of the Animal 2 had a

different population cross-links than the CDET of Animal 1, limiting the ability of CDET fibrils from Animal 2 to form kinks in comparison to the less cross-linked CDET fibrils from Animal 1. The cross-linking profiles could feasibly be different in trivalent cross-link content, and also in divalent cross-links density. The explanation of distinct cross-linking between the CDET of Animal 1 and Animal 2 underlying the different rupture strain, kink formation, and shell delamination is left as speculation.

Nodes

The undisrupted nodes observed on CDET fibrils (Figure 4.5) had interesting features, but were difficult to explain with certainty. Some nodes occured very close to where the AFM tip contacted the fibril, suggesting protective clamping of the fibril by the AFM tip at that location. However, other nodes appeared far from point where the AFM tip contacted the fibril, and thus need another explanation. As the nodes were devoid of kinks or shell delamination, it is clear that there were highly localized regions that were robust against plastic damage. Considering the process of fibrillogenesis, the nodes may be a consequence of a fibril fusion event: discrete fibril segments 10-30 μm in length [43, 44] are deposited in the first days of fibrillogenesis, followed by lateral and end-to-end fusion between the segments during tendon development [44], leading to long fibrils in mature tendon [45]. The CDET nodes may be locations of end-to-end segment fusion. The four cases in which nodes separated regions that were not equally damaged (Figure 4.5A, B, E, G) suggest that the node may have effectively screened stress from a particular region of fibril, resulting in one side of the node being more intact than the other post-rupture. The structurally robust nature of nodes may be a result of denser cross-linking at that location, created during a fibril fusion event in fibrillogenesis.

5.3.3   Comparison of post-rupture fibril morphology with existing works

The morphological dichotomy between SDFT and CDET fibrils in the current work is similar to the structural results in the work of Svensson [84]. The post-rupture morphologies of positional CDET and RTT fibrils [84] were remarkably similar: the motifs of a radially delaminated shell from a zig-zagging core that characterized CDET fibrils (Figure 4.4) were similarly observed on most of the RTT fibrils [84]. It is

important to note that these fibrils were ruptured in a vertically oriented AFM pull, so they were not in contact with the glass substrate during extension and yet still delaminated a shell. Geometry-independent shell formation observed on positional tendon fibrils between the current work and that of Svensson [84] strongly suggests that shell delamination is a characteristic process of positional tendon fibrils, and that it does not arise from external shear forces. The fact that neither of the energy storing tendon fibrils from the SDFT (Figure 4.7) or HPT [84] delaminated a shell suggests that shell delamination is not a characteristic process of energy storing tendon fibrils. A significant relationship between tendon type and post-rupture morphology was only elucidated in the current work, and was not achieved in the work of Svensson [84], which may have simply been due to the larger sample size investigated in the current work.

There are distinct structural results in the current work and the rupture study on rat patellar tendon (RPT) fibrils by Liu [85]. The post-fracture RPT fibril morphology revealed via SEM showed that each fractured fibril had intact D-banding for most of its length, except at one weak point, where a clean separation with a well defined angle occured. The authors observed collagenous material bridging the separated fibril pieces, and referred to the events as fractures, not ruptures. The post-fracture morphology suggests that necking had occured at the fracture location. RPT fibril necking at one weak location explains why the D-band was intact on the majority of the fibril, despite being subjected to strains >60% [85], and can also explain why the RPT fibrils did not demonstrate high strain stiffening during their graceful mechanical failure. While the fact that necking occured on Liu's RPT fibrils is suggested in the SEM images, the root of the necking is not clear. The differences may be due to end effects, since the 10 μm segment length used in that study is notably smaller than the $\sim$ 55 μm segment length used in the current work and the $\sim$ 35 μm segment length used by Svensson [84]. Overall, the mechanistic path to failure observed by Liu [85] appears to be dominated by effects of stress concentration and necking. This is very different than the consistent picture elucidated in both the current work and the work of Svensson [84] that the energy storing or positional nature of tendon type controls the mechanistic path to failure.

5.4 Post-rupture molecular order via SHG

5.4.1 Expectation for damaged collagen

Collagen fibrils are known to demonstrate SHG [92, 93, 94, 95], which arises from the geometry of each triple-helical collagen molecule: the triple helix is a noncentrosymmetric structure, and delocalized electrons in the peptide bonds of the α-chains are the SHG contributors [98, 99, 100]. Since SHG is sensitive to the molecular state of collagen, it has been used to investigate the thermal denaturation of collagen molecules in a number of tissues [101, 102, 103, 104]. In each study, the SHG signal decreased with increasing temperature, as the molecules lost their helicity and stopped producing SHG. In addition to these tissue level investigations, SHG has been used to investigate single fibrils [105], so we utilized SHG to further investigate the rupture-induced changes in molecular structure on SDFT and CDET fibrils. SHG occurs in both the forward and backward directions [128], and is primarily forward propagating due to different phase matching properties in the two directions [129, 130]: backward scattered SHG has a smaller coherence length (~ 70 nm) than forward scattered SHG (~ 1 μm) [115, 112], so it probes a smaller volume. Since the coherence length of backward SHG is smaller than the dimension of the fibril, it is expected to be less sensitive to structural alteration than forward SHG, which probes the whole fibril.

5.4.2 SDFT and CDET fibrils have distinct molecular response to rupture

On the one hand, the ratio of ruptured/unruptured SHG was not different than 1 for either forward or backward scattering for SDFT fibrils (Figure 4.13). This suggests that molecular order and helicity of the collagen molecules in SDFT fibrils was not significantly altered by rupture. On the other hand, the CDET fibrils exibited a ratio of ruptured/unruptured forward SHG that was lower than 1, and was significantly different than the same ratio on SDFT fibrils (Figure 4.13). This is molecular evidence that post-rupture CDET fibrils had more disordered molecules, which were potentially denatured. It is not possible at present to separate the contribtutions of molecular denaturation from orientational disorder on decreasing the SHG signal.

Interestingly, the average CDET fibril ruptured/unruptured backward SHG was

not different than 1. This is most likely due to the smaller focal volume probed by backward SHG than forward SHG: the CDET shell had a flattened, pancake-like shape (Figure 3.14), and if the focal volume was the 70 nm above the glass substrate, it would have been sampling a larger amount of collagen in the ruptured case than the unruptured case. While the shell generally appeared disordered, it is possible that a proportion of the molecules in the shell were not denatured, and still provided an SHG signal. This may have offset the decrease in signal due to denaturation, causing the backward SHG ratio to not be different than 1. With this confounding feature of backward SHG in mind, the decrease in intensity observed with forward SHG provides the clearest picture, as forward SHG was able to sample the whole fibril volume.

The forward SHG was sensitive to the average structural disruption on post-rupture CDET fibrils, and was sensitive to the nodes as well (Figure 4.12C). Smaller structural features, like individual slippage planes or kinks, were not resolved by the SHG. This is unsurprising, since the resolution of the setup was 400 nm, which is larger than a single slippage plane or kink, but is smaller than a node.

Second harmonic generation performed on SDFT fibrils and CDET fibrils yielded results consistent with the mechanical behavior and structural response measured via AFM. SDFT fibrils were structurally robust by both measures, as they did not lose material into a shell (Figure 4.9A), nor did they decrease in SHG intensity post-rupture (Figure 4.13). The structural disruption observed via AFM on CDET fibrils, quantified using longitudinal kink density and radial shell delamination, was corroborated by the decrease in forward SHG. However, relating the decrease in SHG to the kink density or shell delamination proved difficult; the decrease in SHG was not related to the amount of shell delaminated in a straightforward way, complicating the interpretation of decreased SHG as a direct result of the delaminated shell. Since there is potentially denatured collagen in the kinked core as well as in the delaminated shell, these contributions are difficult to parse. Nevertheless, this is the first study to quantitatively show that SHG is sensitive to mechanical damage on single fibrils.

5.5 SDFT-CDET tendon model

The bovine SDFT-CDET model is an excellent model for comparative study between an energy storing and positional tendon. By testing fibrils extracted from two tendons

removed from a single forelimb, variables including animal age, regularity of exercise, and diet were paired between those two tendons.

5.5.1 Post-rupture fibril morphology is similar whether tendon or single fibrils are ruptured

Recently, the nanoscale structure of collagen fibrils and macroscale functional response of the bovine SDFT and CDET was investigated at the tendon level by Herod *et al.* [62]. This work elucidated the structural response of single fibrils to tendon rupture, and is a natural choice for comparison for the current work. Morphologically, the fibrils that were ruptured individually in the current work recapitulated the characteristic fibril features observed in response to tendon rupture. First, SDFT fibrils were structurally robust when ruptured individually (Figure 4.7) or in a tendon, and generally did not demonstrate any plastic deformation. When viewed under SEM, a dense filamentous network was observed between SDFT fibrils [62]; the current work suggests that this meshwork was not the primary factor underlying the robust morphological fibril response to tendon rupture, but rather, it suggests that the structural integrity was inherent to the SDFT fibrils themselves.

The dense arrays of longitudinal kinks and delamination of a disordered shell observed on CDET fibrils (Figure 4.4) are similar to the characteristic manifestations of discrete plasticity, demonstrated by bovine CDET fibrils in response to tendon rupture [62]. When the phenomena of discrete plasticity as a mode of fibrillar damage was first investigated on bovine tail tendon fibrils, both longitudinal and radial damage were observed [68] and a sequential, two-stage damage model was suggested. In the first stage, damage manifested as periodic longitudinal kinking, which was followed by the second stage of surface denaturation [68]. In the current work, I observed that CDET fibrils which only demonstrate slippage plane damage longitudinally did not delaminate a shell, while fibrils with a zig-zagging kinked core did delaminate a shell (Figure 4.12). This observation is consistent with Veres and Lee's [68] sequential model at the single fibril level, suggesting that what we have observed may be discrete plasticity on single fibrils. While the post-rupture morphology is clear evidence that individual fibrils are directly engaged and damaged during tendon rupture, the contribution of fibril mechanics to tendon mechanics is not as straightforward.

5.5.2 Scaling from fibrillar mechanics to tendon mechanics

When Herod *et al.* [62] pulled bovine SDFT and CDET tendons to rupture, the CDET proved to be a stronger, tougher tendon than the SDFT. How do fibril mechanics contribute to tendon rupture mechanics? This is a complicated question, since there are two levels of collagenous hierarchy ($\sim 1\ \mu$m fiber and $\sim 100\ \mu$m fascicle) in between the fibril and the tendon. Complicating this question further, the contributions of collagen fiber and fascicle appear to contribute differently to macroscopic tendon behavior. In the equine SDFT/CDET pair, the interfascicular space is larger and sliding between fascicles occurs more readily in the SDFT than in the CDET [59], while sliding of fibers within fascicles occurs less readily in the SDFT than in the CDET [60]. Rather than explicitly considering the complicated hierarchical scheme, I will use a simpler model based on XRD to directly relate tendon and average fibril strain, which has suggested that fibril strain only accounts for only ~ 30 % of tendon extension [54]. Assuming this relationship is true during the whole rupture process, then the yield strain of the CDET of 32 % would correspond to 10% fibril strain. The actual rupture strain of the CDET was above 50% strain [62], so a maximum strain closer to 20 % than 10 % may have been passed onto the fibrils prior to tendon rupture. Interestingly, this level of strain corresponds to the regime of high strain stiffening in SDFT fibrils (Figure 4.2A, C), supporting the notion that plastic damage resistance is related to mechanical stiffening.

Scaling tendon to fibril strain based on XRD has the advantage of being a simple model, but it is only an approximation. Since the 30 % fibril/tendon strain relationship was measured using tendon strain only up to 10% and using strain rates <0.1 %/s [54], this may not be representative of the fibril strain/tendon strain fraction that occured as tendon were pulled to rupture (>30%) at a strain rate of 10%/s in the work of Herod *et al.* [62]. However, the same fraction has not been quantified in the conditions used by Herod *et al.* so I use the fraction of 0.3 as an estimate.

To compare tendon and fibril stress, the volume fraction of water in each measurement must be accounted for. In the current work, the reported mechanical properties were based on dehydrated fibril cross-sectional area, while Veres [62] based their mechanical properties on hydrated tendon cross-sectional area. AFM investigation of fibril swelling have shown a diameter increase of 70-100 % between dehydrated and

hydrated states [123, 82, 114]. Assuming a swelling of 100 % in fibril height, the hydrated cross-sectional area is 4 times larger than the dehydrated cross-sectional area. Applying this factor of 4 to the average fibril stress of $\sim$ 200 MPa at 10 % strain (Figure 4.2), the hydrated fibril stress would be 50 MPa. This level of stress is comparable to the $\sim$ 30 MPa yield strength measured at the tendon level. In this simple model, the fibrils have a higher stress than the tendon, sensibly suggesting that the fibril material is stiffer than the nonfibrillar material in tendon cross-section.

5.5.3   Physiological implications

The results of the current work imply that the tissue maintenance may be very different between the SDFT and CDET. Tissue turnover is a cell mediated process, and a cellular response to mechanically denatured collagen has been observed: macrophage-like U937 cells recognized and digested damaged collagen from bovine tail tendon fibrils that had undergone strain-induced discrete plasticity, but did not remove collagen from undamaged fibrils [131]. It is reasonable to assume that a similar response would be observed on the damaged CDET fibrils. It is feasible that the cell's ability to recognize and remove damaged collagen may facilitate overall tissue turnover.

However, since single SDFT fibrils were largely intact, without notable plastic deformation or loss of SHG, this suggests that SDFT molecules are cohesively packed such that they never become mechanically denatured. Since macrophage-like U937 cells did not remove collagen from undamaged fibrils [131], it is reasonable to predict that they would not readily remove material from the structurally robust SDFT fibrils. In addition to being intact after rupture, the SDFT fibrils were highly resistant to fatigue damage, and were structurally intact after a thousand cycles [62].

Since SDFT fibrils are evidently robust against mechanical denaturation, while CDET fibrils plastically deform quite regularly, this is likely one cause of the slower turnover rate observed in the SDFT than CDET [4, 58]. Distinct tissue turnover may exist between energy storing and positional tendon generally.

Why are the SDFT fibrils so much more structurally robust than CDET fibrils? One reason, proposed by Herod *et al.* [62], is that a strength vs. fatigue resistance tradeoff exists, and each tendon type is built of fibrils that are best suited for the primary demand of that tendon. Since the SDFT experiences higher higher stress in

each locomotive stride than the CDET [3], the demand for fatigue resistance would likely be higher, so it is sensible that the SDFT fibrils are more fatigue resistant than the CDET fibrils [62]. The demand for elastic energy storage in locomotion may also be a driving factor the hysteresis of the SDFT tendon is smaller than that of the CDET tendon [60, 62]. I propose that energy storage and fatigue resistance are likely two sides on the same coin. On the mechanical side, energy can be stored and returned when it is stored in elastic deformations, but not when it is dissipated in viscous/plastic deformations. On the structural side, fatigue resistance is possible when viscous/plastic deformation is minimized, and structural alterations are reversible.

Chapter 6

Conclusion

6.1 Summary of results

The current work culminates in four main conclusions. First, the stress-strain relationship of single SDFT and CDET fibrils pulled to rupture are distinct. SDFT fibrils demonstrated high strain stiffening, which arose due to stretching of α-chains after triple helices had been unfolded. CDET fibrils demonstrated a graceful failure and higher extensibility than SDFT fibrils, which arose due to poorly restrained sliding of collagen molecules after some unfolding. Interestingly, CDET fibrils were not stronger or tougher than SDFT fibrils, which was expected because the CDET is stronger and tougher than the SDFT [62]. It is likely that the inherent difference in cross-linking profile underlies the distinct mechanistic paths to failure.

Second, single SDFT fibrils are inherently robust against plastic damage, while CDET fibrils are susceptible to damage. This is an important result which shows that the filamentous interfibrillar meshwork that exists in the SDFT was not responsible for the lack of damage induced by tendon rupture [62], but rather shows that the fibrils themselves are robust against damage. The damage on CDET fibrils was highly reminiscent of discrete plasticity observed on bovine tail tendon and bovine CDET fibrils in response to tendon rupture, suggesting discrete plasticity is a fibrillar process inherent to positional tendons.

Third, CDET fibrils which were more heavily damaged post-rupture were more extensible, but damage was not correlated with toughness. This suggests a structure-function relationship between kink formation and extra extensibility. Shell delamination was correlated with kinks formed, suggesting their may be a single structural alteration that connects the longitudinal and radial manifestations of damage.

Fourth, molecules were not disrupted in SDFT fibrils, but were more disordered post-rupture in CDET fibrils post-rupture. The drop in SHG observed post-rupture was due to a combination of molecular denaturation and orientational disorder between molecules. Since SDFT fibrils did not lose any SHG, the molecules are neither

81

denatured or disordered.

6.2 Significance

The current work has a simple overarching significance: single fibrils from different tendons follow unique paths to failure. Choice of tissue has a fundamental impact on mechanical and structural properties of fibrils, and the different features observed on the bovine SDFT and CDET appear to be indicative of a energy-storing versus positional tendons. The distinct structural response of SDFT and CDET fibrils would have an effect on cell recognition, removal and repair of damaged collagen, and may require distinct mechanisms for tissue turnover. If the features observed on the SDFT and CDET are representative of energy-storing and positional tendons in general, this could suggest distinct tissue turnover processes exist generally between functionally distinct tendons.

6.3 Next steps

The results of the current work motivate a number of further questions, some of which the AFM bowstring method is well-suited to investigate. I outline eight avenues of thought, each of which would further our understanding of fibril structure and mechanics in a unique direction:

1) Are the chemical cross-linking profiles of the bovine SDFT and CDET distinct? High performance liquid chromatography (HPLC) on bovine SDFT and CDET tissue would quantify the cross-linking contributions of hydroxylysyl pyridinoline, lysyl pyridinoline, and the AGE pentosidine [83]. The chemical cross-linking content has been quantified in the equine model [58], and directly measuring cross-linking in the bovine model would illuminate how directly the chemical composition is mirrored across species.

2) Is tendon strain transferred to fibrils differently in the bovine SDFT and CDET? Time resolved XRD on rat tail tendon showed that 30% of tendon strain is transferred to fibril strain [54], but large differences between the interfascicular interface of the equine SDFT and CDET [59] suggest that strain may be hierarchically transferred differently between the SDFT and CDET. I suggest performing time resolved XRD

on the bovine SDFT and CDET, to investigate whether different amounts of tendon strain are transferred to fibril strain by tendon type.

3) Do rupture mechanics of the bovine SDFT and CDET fibrils depend on segment length? I noted in the current work that it was difficult to isolate segments that were shorter than 50 μm, because the amount of glue on the glass tip was variable between applications and some horizontal spreading would occur. Automating the application of glue strips would enable shorter segments to be more reliably reproduced. It was also not possible to visualize segments that were longer than $\sim$ 60 μm, because that was the field of view of the 100x objective used. By using an objective with a larger field of view, longer fibril segments could be visualized while tested.

4) Does the mechanistic path to failure of single bovine SDFT and CDET fibrils depend on strain rate? Tendon level rupture of the SDFT and CDET at different speeds show that the mechanism of shell delamination in CDET is largely frozen out with increasing strain rate [132]. Rupturing single CDET fibrils at strain rates higher than the 1%/s using the AFM bowstring method could recapitulate this at the single fibril level, and would shed light on the characteristic relaxation time associated with the viscous process of shell delamination. Interestingly, the SDFT fibrils showed kinks in response to tendon rupture at a strain rate of 1%/s [132]. Rupturing single SDFT fibrils at a strain rate below the 1%/s used in the current work may elicit a morphological response involving kink formation, which could be investigated by dehydrated AFM imaging. I predict that increasing the strain rate on CDET fibrils would freeze out the shell formation mechanism, and decreasing the strain rate on SDFT fibrils would enable kink formation.

5) Are the relative contributions of elastic and viscous components to fibril tension different between the bovine SDFT and CDET? This could be investigated by a force relaxation experiment using the AFM, in which single SDFT and CDET fibrils are pulled to a given strain in the bowstring geometry, and then held there for an extended period of time afterwards. By measuring the force decay as a function of time at a given strain, the elastic and viscous contributions to fibril tension can be separated. The AFM could subsequently be used to investigate structural changes in these fibrils, though they would have to be relaxed back to their initial positions with the removal of the AFM tip from the surface. I predict that single SDFT fibrils would have a

higher relative elastic contribution than CDET fibrils.

6) Is there a difference in the hysteresis of single SDFT and CDET fibrils? Considering that the SDFT demonstrates less hysteresis than the CDET at the tendon level and the fascicle level, I predict that single SDFT fibrils would have less hysteresis than CDET fibrils, for any number of cycles measured. AFM imaging could be used to investigate the accumulation of structural alterations as a function of cycle number. When considering cyclic experiments, it should be noted that AFM bowstring method can be used to cycle a fibril to a given strain more easily than cycling it up to a given force.

7) Does cyclic subrupture loading cause a decrease in SHG intensity for single SDFT or CDET fibrils? Since the SDFT fibrils did not lose any SHG when ruptured, it is likely that cyclic subrupture loading would not have an effect either. More interestingly, the CDET fibrils may incur damage progressively during cyclic subrupture tests, and that progression could be investigated through SHG.

8) Does the collagen hybridizing peptide (CHP) demonstrate distinct binding capabilities to loaded SDFT and CDET fibrils? CHP is a collagen mimicking peptide which can be fluorescently tagged, and binds to unfolded collagen molecules without binding to intact collagen molecules [133, 134]. Since CDET fibrils have a tendency to delaminate a disordered shell, I predict that CHP binding would be greater in the CDET than SDFT fibrils. The AFM bowstring method is well-suited to this investigation, because it produces a large number of fibrils on a single dish, that would all be exposed to the CHP molecule at once. Fluorescent binding could be added after either a rupture or cyclic subrupture protocol.

Bibliography

[1] R Alexander and Alexandra Vernon. The mechanics of hopping by kangaroos (macropodidae). *Journal of Zoology*, 177(2):265–303, 1975.

[2] R McNeill Alexander. Elastic energy stores in running vertebrates. *American Zoologist*, 24(1):85–94, 1984.

[3] RF Ker, RMcN Alexander, and MB Bennett. Why are mammalian tendons so thick? *Journal of Zoology*, 216(2):309–324, 1988.

[4] EL Batson, RJ Paramour, TJ Smith, HL Birch, JC Patterson-Kane, and AE Goodship. Are the material properties and matrix composition of equine flexor and extensor tendons determined by their functions? *Equine veterinary journal*, 35(3):314–318, 2003.

[5] Thomas L Willett, Rosalind S Labow, Nicholas C Avery, and J Michael Lee. Increased proteolysis of collagen in an in vitro tensile overload tendon model. *Annals of biomedical engineering*, 35(11):1961–1972, 2007.

[6] Adam P Rumian, Andrew L Wallace, and Helen L Birch. Tendons and ligaments are anatomically distinct but overlap in molecular and morphological featuresa comparative study in an ovine model. *Journal of orthopaedic research*, 25(4):458–464, 2007.

[7] D Amiel, C Frank, F Harwood, J Fronek, and W Akeson. Tendons and ligaments: a morphological and biochemical comparison. *Journal of Orthopaedic Research*, 1(3):257–265, 1983.

[8] FH Silver, YP Kato, M Ohno, and AJ Wasserman. Analysis of mammalian connective tissue: relationship between hierarchical structures and mechanical properties. *Journal of long-term effects of medical implants*, 2(2-3):165–198, 1991.

[9] J Hae Yoon and J Halper. Tendon proteoglycans: biochemistry and function. *J Musculoskelet Neuronal Interact*, 5(1):22–34, 2005.

[10] JOHN E Scott. Extracellular matrix, supramolecular organisation and shape. *Journal of anatomy*, 187(Pt 2):259, 1995.

[11] Renato V Iozzo. Matrix proteoglycans: from molecular design to cellular function. *Annual review of biochemistry*, 67(1):609–652, 1998.

[12] Thomas J Koob and Kathryn G Vogel. Site-related variations in glycosaminoglycan content and swelling properties of bovine flexor tendon. *Journal of orthopaedic research*, 5(3):414–424, 1987.

[13] Gion Fessel and Jess G Snedeker. Evidence against proteoglycan mediated collagen fibril load transmission and dynamic viscoelasticity in tendon. *Matrix Biology*, 28(8):503–510, 2009.

[14] DT Kirkendall and WE Garrett. Function and biomechanics of tendons. *Scandinavian journal of medicine & science in sports*, 7(2):62–66, 1997.

[15] Nicholas S Kalson, Yinhui Lu, Susan H Taylor, Tobias Starborg, David F Holmes, and Karl E Kadler. A structure-based extracellular matrix expansion mechanism of fibrous tissue growth. *Elife*, 4:e05958, 2015.

[16] DH Elliott. Structure and function of mammalian tendon. *Biological Reviews*, 40(3):392–421, 1965.

[17] J Kastelic, A Galeski, and E Baer. The multicomposite structure of tendon. *Connective tissue research*, 6(1):11–23, 1978.

[18] Peter Fratzl. Cellulose and collagen: from fibres to tissues. *Current opinion in colloid & interface science*, 8(1):32–39, 2003.

[19] Pauline M Cowan, Stewart McGavin, and ACT North. The polypeptide chain configuration of collagen. *Nature*, 176:1062–1064, 1955.

[20] GN Ramachandran and Gopinath Kartha. Studies on collagen. In *Proceedings of the Indian Academy of Sciences-Section A*, volume 42, pages 215–234. Springer, 1955.

[21] Alexander Rich and Francis Crick. The structure of collagen, 1955.

[22] Darwin J Prockop and Kari I Kivirikko. Collagens: molecular biology, diseases, and potentials for therapy. *Annual review of biochemistry*, 64(1):403–434, 1995.

[23] Johanna Myllyharju and Kari I Kivirikko. Collagens, modifying enzymes and their mutations in humans, flies and worms. *TRENDS in Genetics*, 20(1):33–43, 2004.

[24] Michel Van der Rest and Robert Garrone. Collagen family of proteins. *The FASEB journal*, 5(13):2814–2823, 1991.

[25] Rachel Z Kramer, Jordi Bella, Barbara Brodsky, and Helen M Berman. The crystal and molecular structure of a collagen-like peptide with a biologically relevant sequence. *Journal of molecular biology*, 311(1):131–147, 2001.

[26] Karl E Kadler, David F Holmes, John A Trotter, and John A Chapman. Collagen fibril formation. *Biochemical Journal*, 316(1):1–11, 1996.

[27] Elizabeth G Canty and Karl E Kadler. Procollagen trafficking, processing and fibrillogenesis. *Journal of cell science*, 118(7):1341–1353, 2005.

[28] Jamshid Khoshnoodi, Jean-Philippe Cartailler, Keith Alvares, Arthur Veis, and Billy G Hudson. Molecular recognition in the assembly of collagens: terminal noncollagenous domains are key recognition modules in the formation of triple helical protomers. *Journal of Biological Chemistry*, 281(50):38117–38121, 2006.

[29] LI Fessler, RE Burgeson, NP Morris, and JH Fessler. Collagen synthesis: a disulfide-linked collagen precursor in chick bone. *Proceedings of the National Academy of Sciences*, 70(10):2993–2996, 1973.

[30] Matthew D Shoulders and Ronald T Raines. Collagen structure and stability. *Annual review of biochemistry*, 78:929, 2009.

[31] Thengiz V Burjanadze. New analysis of the phylogenetic change of collagen thermostability. *Biopolymers*, 53(6):523–528, 2000.

[32] Robert C Siegel, Sheldon R Pinnell, and George R Martin. Cross-linking of collagen and elastin. properties of lysyl oxidase. *Biochemistry*, 9(23):4486–4492, 1970.

[33] Joseph PRO Orgel, Andrew Miller, Thomas C Irving, Robert F Fischetti, Andrew P Hammersley, and Tim J Wess. The in situ supermolecular structure of type i collagen. *Structure*, 9(11):1061–1069, 2001.

[34] Karl E Kadler, Yoshio Hojima, and DJ Prockop. Assembly of collagen fibrils de novo by cleavage of the type i pc-collagen with procollagen c-proteinase. assay of critical concentration demonstrates that collagen self-assembly is a classical example of an entropy-driven process. *Journal of Biological Chemistry*, 262(32):15696–15701, 1987.

[35] Alan S Craig, Mervyn J Birtles, James F Conway, and David AD Parry. An estimate of the mean length of collagen fibrils in rat tail-tendon as a function of age. *Connective tissue research*, 19(1):51–62, 1989.

[36] S Leikin, DC Rau, and VA Parsegian. Temperature-favoured assembly of collagen is driven by hydrophilic not hydrophobic interactions. *Nature structural biology*, 2(3):205–210, 1995.

[37] JW Smith. Molecular pattern in native collagen. *Nature*, 219:157–158, 1968.

[38] Samuel J Baldwin, Andrew S Quigley, Charlotte Clegg, and Laurent Kreplak. Nanomechanical mapping of hydrated rat tail tendon collagen i fibrils. *Biophysical journal*, 107(8):1794–1801, 2014.

[39] David F Holmes and Karl E Kadler. The 10+ 4 microfibril structure of thin cartilage fibrils. *Proceedings of the National Academy of Sciences*, 103(46):17249–17254, 2006.

[40] Joseph PRO Orgel, Thomas C Irving, Andrew Miller, and Tim J Wess. Microfibrillar structure of type i collagen in situ. *Proceedings of the National Academy of Sciences*, 103(24):9001–9005, 2006.

[41] Mario Raspanti. Different architectures of collagen fibrils enforce different fibrillogenesis mechanisms. *Journal of Biomedical Science and Engineering*, 3(12):1169, 2010.

[42] L Yang, KO Van der Werf, PJ Dijkstra, J Feijen, and ML Bennink. Micromechanical analysis of native and cross-linked collagen type i fibrils supports the existence of microfibrils. *Journal of the mechanical behavior of biomedical materials*, 6:148–158, 2012.

[43] David E Birk, Emanuel I Zycband, Donald A Winkelmann, and Robert L Trelstad. Collagen fibrillogenesis in situ: fibril segments are intermediates in matrix assembly. *Proceedings of the National Academy of Sciences*, 86(12):4549–4553, 1989.

[44] David E Birk, Maria V Nurminskaya, and Emanuel I Zycband. Collagen fibrillogenesis in situ: Fibril segments undergo post-depositional modifications resulting in linear and lateral growth during matrix development. *Developmental Dynamics*, 202(3):229–243, 1995.

[45] David E Birk, Emanuel I Zycband, Samantha Woodruff, Donald A Winkelmann, and Robert L Trelstad. Collagen fibrillogenesis in situ: fibril segments become long fibrils as the developing tendon matures. *Developmental Dynamics*, 208(3):291–298, 1997.

[46] David R Baselt, Jean-Paul Revel, and John D Baldeschwieler. Subfibrillar structure of type i collagen observed by atomic force microscopy. *Biophysical journal*, 65(6):2644, 1993.

[47] Susumu Yamamoto, Hiroya Hashizume, Jiro Hitomi, Masatsugu Shigeno, Shoichi SAWAGUCHI, Haruki ABE, and Tatsuo USHIKI. The subfibrillar arrangement of corneal and scleral collagen fibrils as revealed by scanning electron and atomic force microscopy. *Archives of histology and cytology*, 63(2):127–135, 2000.

[48] Allen J Bailey, Robert Gordon Paul, and Lynda Knott. Mechanisms of maturation and ageing of collagen. *Mechanisms of ageing and development*, 106(1):1–56, 1998.

[49] David R Eyre, Mercedes A Paz, and Paul M Gallop. Cross-linking in collagen and elastin. *Annual review of biochemistry*, 53(1):717–748, 1984.

[50] AJ Bailey and MS Shimokomaki. Age related changes in the reducible cross-links of collagen. *FEBS letters*, 16(2):86–88, 1971.

[51] David R Eyre and Jiann-Jiu Wu. Collagen cross-links. In *Collagen*, pages 207–229. Springer, 2005.

[52] Sheldon R Pinnell and George R Martin. The cross-linking of collagen and elastin: enzymatic conversion of lysine in peptide linkage to alpha-aminoadipic-delta-semialdehyde (allysine) by an extract from bone. *Proceedings of the National Academy of Sciences*, 61(2):708–716, 1968.

[53] RC Haut. The effect of a lathyritic diet on the sensitivity of tendon to strain rate. *Journal of biomechanical engineering*, 107(2):166–174, 1985.

[54] R Puxkandl, I Zizak, O Paris, J Keckes, W Tesch, S Bernstorff, P Purslow, and P Fratzl. Viscoelastic properties of collagen: synchrotron radiation investigations and structural model. *Philosophical Transactions of the Royal Society of London B: Biological Sciences*, 357(1418):191–197, 2002.

[55] LHH Olde Damink, PJ Dijkstra, MJA Van Luyn, PB Van Wachem, P Nieuwenhuis, and J Feijen. Glutaraldehyde as a crosslinking agent for collagen-based biomaterials. *Journal of Materials Science: Materials in Medicine*, 6(8):460–472, 1995.

[56] Philip Hansen, Tue Hassenkam, René Brüggebusch Svensson, Per Aagaard, Todd Trappe, Bjarki Thor Haraldsson, Michael Kjaer, and Peter Magnusson. Glutaraldehyde cross-linking of tendon-mechanical effects at the level of the tendon fascicle and fibril. *Connective tissue research*, 50(4):211–222, 2009.

[57] Nicole Verzijl, Jeroen DeGroot, Suzanne R Thorpe, Ruud A Bank, J Nikki Shaw, Timothy J Lyons, Johannes WJ Bijlsma, Floris PJG Lafeber, John W Baynes, and Johan M TeKoppele. Effect of collagen turnover on the accumulation of advanced glycation end products. *Journal of Biological Chemistry*, 275(50):39027–39031, 2000.

[58] H. L. Birch. Tendon matrix composition and turnover in relation to functional requirements. *Int. J. Exp. Path.*, 88:241–248, 2007.

[59] Chavaunne T Thorpe, Chineye P Udeze, Helen L Birch, Peter D Clegg, and Hazel RC Screen. Specialization of tendon mechanical properties results from interfascicular differences. *Journal of The Royal Society Interface*, 2012.

[60] Chavaunne T Thorpe, Christian Klemt, Graham P Riley, Helen L Birch, Peter D Clegg, and Hazel RC Screen. Helical sub-structures in energy-storing tendons provide a possible mechanism for efficient energy storage and return. *Acta biomaterialia*, 9(8):7948–7956, 2013.

[61] Klaus-Dieter Budras. *Bovine anatomy: an illustrated text*. Schlütersche, 2003.

[62] Tyler W Herod, Neil C Chambers, and Samuel P Veres. Collagen fibrils in functionally distinct tendons have differing structural responses to tendon rupture and fatigue loading. *Acta Biomaterialia*, 2016.

[63] I Type. collagen is thermally unstable at body temperature leikina, e.; mertts, mv; kuznetsova, n.; leikin, s. *Proceedings of the National Academy of Sciences of the United States of America*, 99(3):1314–1318, 2002.

[64] Christopher A Miles and Michael Ghelashvili. Polymer-in-a-box mechanism for the thermal stabilization of collagen molecules in fibers. *Biophysical Journal*, 76(6):3243–3252, 1999.

[65] LRG Treloar. *Physics of Rubber Elasticity (Oxford classic texts in the physical sciences)*. Oxford University Press, 2005.

[66] NC Avery and AJ Bailey. Restraining cross-links responsible for the mechanical properties of collagen fibers: natural and artificial. In *Collagen*, pages 81–110. Springer, 2008.

[67] JC Patterson-Kane, DAD Parry, HL Birch, AE Goodship, and EC Firth. An age-related study of morphology and cross-link composition of collagen fibrils in the digital flexor tendons of young thoroughbred horses. *Connective tissue research*, 36(3):253–260, 1997.

[68] Samuel P Veres and J Michael Lee. Designed to fail: a novel mode of collagen fibril disruption and its relevance to tissue toughness. *Biophysical journal*, 102(12):2876–2884, 2012.

[69] Samuel P Veres, Julia M Harrison, and J Michael Lee. Repeated subrupture overload causes progression of nanoscaled discrete plasticity damage in tendon collagen fibrils. *Journal of Orthopaedic Research*, 31(5):731–737, 2013.

[70] Samuel P Veres, Julia M Harrison, and J Michael Lee. Cross-link stabilization does not affect the response of collagen molecules, fibrils, or tendons to tensile overload. *Journal of Orthopaedic Research*, 31(12):1907–1913, 2013.

[71] Gerd Binnig, Calvin F Quate, and Ch Gerber. Atomic force microscope. *Physical review letters*, 56(9):930, 1986.

[72] Daniel Rugar and Paul Hansma. Atomic force microscopy. *Physics today*, 43(10):23–30, 1990.

[73] Gerhard Meyer and Nabil M Amer. Simultaneous measurement of lateral and normal forces with an optical-beam-deflection atomic force microscope. *Applied physics letters*, 57(20):2089–2091, 1990.

[74] Ricardo Garcıa and Ruben Perez. Dynamic atomic force microscopy methods. *Surface science reports*, 47(6):197–301, 2002.

[75] Thomas Gutsmann, Georg E Fantner, Manuela Venturoni, Axel Ekani-Nkodo, James B Thompson, Johannes H Kindt, Daniel E Morse, Deborah Kuchnir Fygenson, and Paul K Hansma. Evidence that collagen fibrils in tendons are inhomogeneously structured in a tubelike manner. *Biophysical journal*, 84(4):2593–2598, 2003.

[76] Colin A Grant, David J Brockwell, Sheena E Radford, and Neil H Thomson. Effects of hydration on the mechanical response of individual collagen fibrils. *Applied Physics Letters*, 92(23):233902, 2008.

[77] Colin A Grant, David J Brockwell, Sheena E Radford, and Neil H Thomson. Tuning the elastic modulus of hydrated collagen fibrils. *Biophysical journal*, 97(11):2985–2992, 2009.

[78] Eike-Christian Spitzner, Stephanie Roper, Mario Zerson, Anke Bernstein, and Robert Magerle. Nanoscale swelling heterogeneities in type i collagen fibrils. *ACS nano*, 9(6):5683–5694, 2015.

[79] Lanti Yang, Kees O van der Werf, Bart FJM Koopman, Vinod Subramaniam, Martin L Bennink, Pieter J Dijkstra, and Jan Feijen. Micromechanical bending of single collagen fibrils using atomic force microscopy. *Journal of Biomedical Materials Research Part A*, 82(1):160–168, 2007.

[80] Lanti Yang, Kees O Van der Werf, Carel FC Fitié, Martin L Bennink, Pieter J Dijkstra, and Jan Feijen. Mechanical properties of native and cross-linked type i collagen fibrils. *Biophysical journal*, 94(6):2204–2211, 2008.

[81] René B Svensson, Tue Hassenkam, Philip Hansen, and S Peter Magnusson. Viscoelastic behavior of discrete human collagen fibrils. *Journal of the Mechanical Behavior of Biomedical Materials*, 3(1):112–115, 2010.

[82] René B Svensson, Tue Hassenkam, Colin A Grant, and S Peter Magnusson. Tensile properties of human collagen fibrils and fascicles are insensitive to environmental salts. *Biophysical journal*, 99(12):4020–4027, 2010.

[83] René B Svensson, Philip Hansen, Tue Hassenkam, Bjarki T Haraldsson, Per Aagaard, Vuokko Kovanen, Michael Krogsgaard, Michael Kjaer, and S Peter Magnusson. Mechanical properties of human patellar tendon at the hierarchical levels of tendon and fibril. *Journal of Applied Physiology*, 112(3):419–426, 2012.

[84] Rene B Svensson, Hindrik Mulder, Vuokko Kovanen, and S Peter Magnusson. Fracture mechanics of collagen fibrils: influence of natural cross-links. *Biophysical journal*, 104(11):2476–2484, 2013.

[85] Yehe Liu, Roberto Ballarini, and Steven J Eppell. Tension tests on mammalian collagen fibrils. *Interface focus*, 6(1):20150080, 2016.

[86] SJ Eppell, BN Smith, H Kahn, and R Ballarini. Nano measurements with micro-devices: mechanical properties of hydrated collagen fibrils. *Journal of the Royal Society Interface*, 3(6):117–121, 2006.

[87] Zhilei L Shen, Mohammad Reza Dodge, Harold Kahn, Roberto Ballarini, and Steven J Eppell. Stress-strain experiments on individual collagen fibrils. *Biophysical Journal*, 95(8):3956–3963, 2008.

[88] Zhilei Liu Shen, Harold Kahn, Roberto Ballarini, and Steven J Eppell. Viscoelastic properties of isolated collagen fibrils. *Biophysical journal*, 100(12):3008–3015, 2011.

[89] Zhilei Liu Shen, Mohammad Reza Dodge, Harold Kahn, Roberto Ballarini, and Steven J Eppell. In vitro fracture testing of submicron diameter collagen fibril specimens. *Biophysical journal*, 99(6):1986–1995, 2010.

[90] PA Franken, Alan E Hill, CW Peters, and G Weinreich. Generation of optical harmonics. *Physical Review Letters*, 7(4):118, 1961.

[91] Robert C Miller. Optical second harmonic generation in piezoelectric crystals. *Applied Physics Letters*, 5(1):17–19, 1964.

[92] I Freund, MOSHE Deutsch, and AARON Sprecher. Connective tissue polarity. optical second-harmonic microscopy, crossed-beam summation, and small-angle scattering in rat-tail tendon. *Biophysical journal*, 50(4):693, 1986.

[93] Aikaterini Zoumi, Alvin Yeh, and Bruce J Tromberg. Imaging cells and extracellular matrix in vivo by using second-harmonic generation and two-photon excited fluorescence. *Proceedings of the National Academy of Sciences*, 99(17):11014–11019, 2002.

[94] Mathias Strupler, A-M Pena, Monica Hernest, P-L Tharaux, J-L Martin, Emmanuel Beaurepaire, and M-C Schanne-Klein. Second harmonic imaging and scoring of collagen in fibrotic tissues. *Optics express*, 15(7):4054–4065, 2007.

[95] Xiyi Chen, Oleg Nadiarynkh, Sergey Plotnikov, and Paul J Campagnola. Second harmonic generation microscopy for quantitative analysis of collagen fibrillar structure. *Nature protocols*, 7(4):654–669, 2012.

[96] Israel Rocha-Mendoza, Diego R Yankelevich, Mingshi Wang, Karen M Reiser, Curt W Frank, and André Knoesen. Sum frequency vibrational spectroscopy: the molecular origins of the optical second-order nonlinearity of collagen. *Biophysical journal*, 93(12):4433–4444, 2007.

[97] François Tiaho, Gaëlle Recher, and Denis Rouede. Estimation of helical angles of myosin and collagen by second harmonic generation imaging microscopy. *Optics express*, 15(19):12286–12295, 2007.

[98] Ariane Deniset-Besseau, Julien Duboisset, Emmanuel Benichou, François Hache, Pierre-François Brevet, and Marie-Claire Schanne-Klein. Measurement of the second-order hyperpolarizability of the collagen triple helix and determination of its physical origin. *The Journal of Physical Chemistry B*, 113(40):13437–13445, 2009.

[99] Adam E Tuer, Serguei Krouglov, Nicole Prent, Richard Cisek, Daaf Sandkuijl, Kazuhiro Yasufuku, Brian C Wilson, and Virginijus Barzda. Nonlinear optical properties of type i collagen fibers studied by polarization dependent second harmonic generation microscopy. *The Journal of Physical Chemistry B*, 115(44):12759–12769, 2011.

[100] Julien Duboisset, Ariane Deniset-Besseau, Emmanuel Benichou, Isabelle Russier-Antoine, Noelle Lascoux, Christian Jonin, Francois Hache, Marie-Claire Schanne-Klein, and Pierre-Francois Brevet. A bottom-up approach to build the hyperpolarizability of peptides and proteins from their amino acids. *The Journal of Physical Chemistry B*, 117(34):9877–9881, 2013.

[101] Beop-Min Kim, Jürgen Eichler, Karen M Reiser, Alexander M Rubenchik, and Luiz B Da Silva. Collagen structure and nonlinear susceptibility: effects of heat, glycation, and enzymatic cleavage on second harmonic signal intensity. *Lasers in surgery and medicine*, 27(4):329–335, 2000.

[102] T Theodossiou, GS Rapti, V Hovhannisyan, E Georgiou, K Politopoulos, and Dido Yova. Thermally induced irreversible conformational changes in collagen probed by optical second harmonic generation and laser-induced fluorescence. *Lasers in medical science*, 17(1):34–41, 2002.

[103] Theodossis A Theodossiou, Christopher Thrasivoulou, Chidi Ekwobi, and David L Becker. Second harmonic generation confocal microscopy of collagen type i from rat tendon cryosections. *Biophysical journal*, 91(12):4665–4677, 2006.

[104] Yen Sun, Wei-Liang Chen, Sung-Jan Lin, Shiou-Hwa Jee, Yang-Fang Chen, Ling-Chih Lin, Peter TC So, and Chen-Yuan Dong. Investigating mechanisms of collagen thermal denaturation by high resolution second-harmonic generation imaging. *Biophysical journal*, 91(7):2620–2625, 2006.

[105] Stéphane Bancelin, Carole Aimé, Ivan Gusachenko, Laura Kowalczuk, Gaël Latour, Thibaud Coradin, and Marie-Claire Schanne-Klein. Determination of collagen fibril size via absolute measurements of second-harmonic generation signals. *Nature communications*, 5, 2014.

[106] Marianne B Ariganello, Rosalind S Labow, and J Michael Lee. Response of macrophage-like u937 cells to decellularized tissue heart valve materials. *J Heart Valve Dis*, 18(2):187–197, 2009.

[107] John E Sader. Frequency response of cantilever beams immersed in viscous fluids with applications to the atomic force microscope. *Journal of applied physics*, 84(1):64–76, 1998.

[108] Harald Herrmann, Harald Bär, Laurent Kreplak, Sergei V Strelkov, and Ueli Aebi. Intermediate filaments: from cell architecture to nanomechanics. *Nature Reviews Molecular Cell Biology*, 8(7):562–573, 2007.

[109] Enrico Gnecco, Roland Bennewitz, Oliver Pfeiffer, Anisoara Socoliuc, and Ernst Meyer. *Friction and Wear on the Atomic Scale*, pages 631–660. Springer Berlin Heidelberg, Berlin, Heidelberg, 2004.

[110] Christopher P Green, Hadi Lioe, Jason P Cleveland, Roger Proksch, Paul Mulvaney, and John E Sader. Normal and torsional spring constants of atomic force microscope cantilevers. *Review of scientific instruments*, 75(6):1988–1996, 2004.

[111] P Hess. Laser diagnostics of mechanical and elastic properties of silicon and carbon films. *Applied surface science*, 106:429–437, 1996.

[112] Marie-Andrée Houle, Charles-André Couture, Stéphane Bancelin, Jarno Kolk, Etienne Auger, Cameron Brown, Konstantin Popov, Lora Ramunno, and François Légaré. Analysis of forward and backward second harmonic generation images to probe the nanoscale structure of collagen within bone and cartilage. *Journal of biophotonics*, 8(11-12):993–1001, 2015.

[113] Claude Elwood Shannon. Communication in the presence of noise. *Proceedings of the IRE*, 37(1):10–21, 1949.

[114] Samuel J Baldwin, Laurent Kreplak, and J Michael Lee. Characterization via atomic force microscopy of discrete plasticity in collagen fibrils from mechanically overloaded tendons: Nano-scale structural changes mimic rope failure. *Journal of the mechanical behavior of biomedical materials*, 60:356–366, 2016.

[115] Cameron P Brown, Marie-Andree Houle, Konstantin Popov, Mischa Nicklaus, Charles-Andre Couture, Matthieu Laliberté, Thomas Brabec, Andreas Ruediger, Andrew J Carr, Andrew J Price, et al. Imaging and modeling collagen architecture from the nano to micro scale. *Biomedical optics express*, 5(1):233–243, 2014.

[116] Yehe Liu, Nelly Andarawis-Puri, and Steven J Eppell. Method to extract minimally damaged collagen fibrils from tendon. *Journal of Biological Methods*, 3(4):e54, 2016.

[117] Yehe Liu. *A Novel Method to Extract Type-I Collagen Fibrils from Mammalian Tendons*. PhD thesis, Case Western Reserve University, 2015.

[118] E Mosler, W Folkhard, E Knörzer, H Nemetschek-Gansler, Th Nemetschek, and MHJ Koch. Stress-induced molecular rearrangement in tendon collagen. *Journal of molecular biology*, 182(4):589–596, 1985.

[119] W Folkhard, E Mosler, W Geercken, E Knörzer, H Nemetschek-Gansler, Th Nemetschek, and MHJ Koch. Quantitative analysis of the molecular sliding mechanisms in native tendon collagentime-resolved dynamic studies using synchrotron radiation. *International Journal of Biological Macromolecules*, 9(3):169–175, 1987.

[120] Ingo Schwaiger, Clara Sattler, Daniel R Hostetter, and Matthias Rief. The myosin coiled-coil is a truly elastic protein structure. *Nature materials*, 1(4):232–235, 2002.

[121] K Misof, WJ Landis, K Klaushofer, and P Fratzl. Collagen from the osteogenesis imperfecta mouse model (oim) shows reduced resistance against tensile stress. *Journal of Clinical Investigation*, 100(1):40, 1997.

[122] Baptiste Depalle, Zhao Qin, Sandra J Shefelbine, and Markus J Buehler. Influence of cross-link structure, density and mechanical properties in the mesoscale deformation mechanisms of collagen fibrils. *Journal of the mechanical behavior of biomedical materials*, 52:1–13, 2015.

[123] Joost AJ van der Rijt, Kees O van der Werf, Martin L Bennink, Pieter J Dijkstra, and Jan Feijen. Micromechanical testing of individual collagen fibrils. *Macromolecular bioscience*, 6(9):697–702, 2006.

[124] Paul Kronick, Beverly Maleeff, and Robert Carroll. The locations of collagens with different thermal stabilities in fibrils of bovine reticular dermis. *Connective tissue research*, 18(2):123–134, 1988.

[125] A Miller. Molecular packing in collagen fibrils. In *Biochemistry of collagen*, pages 85–136. Springer, 1976.

[126] J-C Jesior, A Miller, and C Berthet-Colominas. Crystalline three-dimensional packing is a general characteristic of type i collagen fibrils. *FEBS letters*, 113(2):238–240, 1980.

[127] DJ Hulmes, Tim J Wess, Darwin J Prockop, and Peter Fratzl. Radial packing, order, and disorder in collagen fibrils. *Biophysical Journal*, 68(5):1661, 1995.

[128] Rebecca M Williams, Warren R Zipfel, and Watt W Webb. Interpreting second-harmonic generation images of collagen i fibrils. *Biophysical journal*, 88(2):1377–1386, 2005.

[129] Isaac Freund and Moshe Deutsch. Second-harmonic microscopy of biological tissue. *Optics letters*, 11(2):94–96, 1986.

[130] J Mertz and L Moreaux. Second-harmonic generation by focused excitation of inhomogeneously distributed scatterers. *Optics communications*, 196(1):325–330, 2001.

[131] Samuel P Veres, Ellen P Brennan-Pierce, and J Michael Lee. Macrophage-like u937 cells recognize collagen fibrils with strain-induced discrete plasticity damage. *Journal of Biomedical Materials Research Part A*, 103(1):397–408, 2015.

[132] N. C. Chambers, T. W. Herod, and S. P. Veres. Tendon rupture at the nanoscale: Damage to collagen fibrils varies substantially with both rupture speed and tendon type. *ORS Annual Meeting Abstract Submission*, 2015.

[133] Yang Li and S Michael Yu. Targeting and mimicking collagens via triple helical peptide assembly. *Current opinion in chemical biology*, 17(6):968–975, 2013.

[134] Yang Li, Daniel Ho, Huan Meng, Tania R Chan, Bo An, Hanry Yu, Barbara Brodsky, Albert S Jun, and S Michael Yu. Direct detection of collagenous proteins by fluorescently labeled collagen mimetic peptides. *Bioconjugate chemistry*, 24(1):9–16, 2013.

Copyright permission

Copyright permission for Figure 1.2, adapted from Canty *et al.* [27]

This Agreement between Andrew S Quigley ("You") and Elsevier ("Elsevier") consists of your license details and the terms and conditions provided by Elsevier and Copyright Clearance Center.

License Number	3967140999081
License date	Oct 13, 2016
Licensed Content Publisher	Elsevier
Licensed Content Publication	Acta Biomaterialia
Licensed Content Title	Collagen fibrils in functionally distinct tendons have differing structural responses to tendon rupture and fatigue loading
Licensed Content Author	Tyler W. Herod,Neil C. Chambers,Samuel P. Veres
Licensed Content Date	15 September 2016
Licensed Content Volume Number	42
Licensed Content Issue Number	n/a
Licensed Content Pages	12
Start Page	296
End Page	307
Type of Use	reuse in a thesis/dissertation
Intended publisher of new work	other
Portion	figures/tables/illustrations
Number of figures/tables/illustrations	7
Format	both print and electronic
Are you the author of this Elsevier article?	No
Will you be translating?	No
Order reference number	
Original figure numbers	Figure 2, 3, 4, 5, 6, 8, supplemental figure 3
Title of your thesis/dissertation	Collagen fibrils from physiologically distinct tendons follow unique paths to failure
Expected completion date	Nov 2016
Estimated size (number of pages)	100
Elsevier VAT number	GB 494 6272 12
Requestor Location	Andrew S Quigley 2735 Fuller Terrace

100

License Number	3967141411005
License date	Oct 13, 2016
Licensed Content Publisher	Elsevier
Licensed Content Publication	Journal of the Mechanical Behavior of Biomedical Materials
Licensed Content Title	Micromechanical analysis of native and cross-linked collagen type I fibrils supports the existence of microfibrils
Licensed Content Author	L. Yang,K.O. van der Werf,P.J. Dijkstra,J. Feijen,M.L. Bennink
Licensed Content Date	February 2012
Licensed Content Volume Number	6
Licensed Content Issue Number	n/a
Licensed Content Pages	11
Start Page	148
End Page	158
Type of Use	reuse in a thesis/dissertation
Intended publisher of new work	other
Portion	figures/tables/illustrations
Number of figures/tables/illustrations	1
Format	both print and electronic
Are you the author of this Elsevier article?	No
Will you be translating?	No
Order reference number	
Original figure numbers	Figure 2
Title of your thesis/dissertation	Collagen fibrils from physiologically distinct tendons follow unique paths to failure
Expected completion date	Nov 2016
Estimated size (number of pages)	100
Elsevier VAT number	GB 494 6272 12
Requestor Location	Andrew S Quigley 2735 Fuller Terrace

101

This Agreement between Andrew S Quigley ("You") and Elsevier ("Elsevier") consists of
your license details and the terms and conditions provided by Elsevier and Copyright
Clearance Center.

License Number	3967150905454
License date	Oct 13, 2016
Licensed Content Publisher	Elsevier
Licensed Content Publication	Biophysical Journal
Licensed Content Title	Fracture Mechanics of Collagen Fibrils: Influence of Natural Cross-Links
Licensed Content Author	Rene B. Svensson,Hindrik Mulder,Vuokko Kovanen,S. Peter Magnusson
Licensed Content Date	4 June 2013
Licensed Content Volume Number	104
Licensed Content Issue Number	11
Licensed Content Pages	9
Start Page	2476
End Page	2484
Type of Use	reuse in a thesis/dissertation
Intended publisher of new work	other
Portion	figures/tables/illustrations
Number of figures/tables/illustrations	2
Format	both print and electronic
Are you the author of this Elsevier article?	No
Will you be translating?	No
Order reference number	
Original figure numbers	Figures 4 and 5
Title of your thesis/dissertation	Collagen fibrils from physiologically distinct tendons follow unique paths to failure
Expected completion date	Nov 2016
Estimated size (number of pages)	100
Elsevier VAT number	GB 494 6272 12
Requestor Location	Andrew S Quigley 2735 Fuller Terrace

104

This Agreement between Andrew S Quigley ("You") and Nature Publishing Group ("Nature Publishing Group") consists of your license details and the terms and conditions provided by Nature Publishing Group and Copyright Clearance Center.

License Number	3967151391546
License date	Oct 13, 2016
Licensed Content Publisher	Nature Publishing Group
Licensed Content Publication	Nature Reviews Molecular Cell Biology
Licensed Content Title	Intermediate filaments: from cell architecture to nanomechanics
Licensed Content Author	Harald Herrmann,Harald Bär,Laurent Kreplak,Sergei V. StrelkovandUeli Aebi
Licensed Content Date	Jul 1, 2007
Licensed Content Volume Number	8
Licensed Content Issue Number	7
Type of Use	reuse in a dissertation / thesis
Requestor type	academic/educational
Format	print and electronic
Portion	figures/tables/illustrations
Number of figures/tables/illustrations	1
High-res required	no
Figures	Box 2
Author of this NPG article	no
Your reference number	
Title of your thesis / dissertation	Collagen fibrils from physiologically distinct tendons follow unique paths to failure
Expected completion date	Nov 2016
Estimated size (number of pages)	100
Requestor Location	Andrew S Quigley 2735 Fuller Terrace
	Halifax, NS B3K 3V9 Canada Attn: Andrew S Quigley
Billing Type	Invoice
Billing Address	Andrew S Quigley 2735 Fuller Terrace